Investigation on intense magnetic flux shielding with a high temperature superconducting tube for a transverse polarized target at the $\bar{\text{P}}$ANDA experiment

Dissertation

zur Erlangung des Grades
"Doktor der Naturwissenschaften"

am Fachbereich Physik, Mathematik und Informatik
der Johannes Gutenberg-Universität Mainz

Bertold Fröhlich
geboren in Budapest

Mainz, den 18. Oktober 2017

Tag der mündlichen Prüfung: 23. Oktober 2018

Zusammenfassung

Observablen, die durch eine transversale Targetpolarisation erfasst werden können, werden in Hochenergieexperimenten untersucht. Das Teilchenphysikexperiment $\bar{\text{P}}$ANDA besteht aus einem Detektor am Teilchenbeschleuniger FAIR, der am GSI Helmholtzzentrum für Schwerionenforschung in Darmstadt gebaut wird. Dieser Detektor benötigt ein hohes Magnetfeld in longitudinaler Richtung bezüglich des Antiprotonenstrahls, um eine hohe Impulsauflösung elektrisch geladener Teilchen zu ermöglichen. Für die Machbarkeit eines transversal polarisierten Targets ist es erforderlich, das longitudinale Magnetfeld abzuschirmen.

Die Möglichkeit ein intensives Magnetfeld mit Hilfe eines Abschirmrohres aus einem BSCCO Hochtemperatursupraleiter abzuschirmen wurde bezüglich eines erreichbaren Abschirmfaktors, dessen Stabilität in der Zeit und der residualen magnetischen Flussdichte entlang der Rohrachse experimentell untersucht. Eine numerische Simulation des induzierten Stromes im Abschirmrohr und der residualen magnetischen Flussdichte entlang seiner Achse wurde entwickelt, und die experimentellen Ergebnisse mit den Vorhersagen dieser Simulation verglichen.

Am Helmholtz-Institut Mainz (HIM) wurde eigens für diese Untersuchung eine Experimentierapparatur bestehend aus einem Kryostaten für flüssiges Helium bei einer Temperatur von 4,2 K entwickelt und aufgebaut. Das Abschirmrohr wurde mit einer beweglichen Hall-Sonde, mit einem speziellen Null-Feld Magneten aufgesetzt, versehen. Das externe Magnetfeld wurde von einem hierfür angefertigten supraleitenden Solenoiden, der auf dem Abschirmrohr montiert werden kann, erzeugt.

Eine magnetische Flussdichte von 1 T wurde angelegt und abgeschirmt, mit einem Abschirmfaktor von mindestens $3,2 \cdot 10^5$, bei einem Konfidenzniveau von 95 %. Bei einer Messung über vier Tage konnte ein weiteres Eindringen nicht beobachtet werden. Die Messung der residualen magnetischen Flussdichte entlang der Rohrachse zeigte eine Abschirmung über 80 mm (bei 150 mm Abschirmrohrlänge) bis 1 T. BSCCO ist ein geeignetes Material, das hohe Magnetfeld im $\bar{\text{P}}$ANDA Spektrometer abzuschirmen.

Abstract

In high energy particle experiments one is interested in observables that require a transverse target polarization. The particle physics experiment $\bar{\text{P}}$ANDA consists of a detector at the particle accelerator FAIR currently under construction at GSI Helmholtz Centre for Heavy Ion Research, Darmstadt (GSI). The detector requires a high magnetic field in longitudinal direction with respect to the antiproton beam to provide high momentum resolution of the electrically charged particles. For the feasibility of a transverse polarized target in $\bar{\text{P}}$ANDA, it is essential to shield the longitudinal magnetic field.

The ability to shield an intense magnetic flux with a high temperature superconductor BSCCO in form of a shielding tube was investigated experimentally. A shielding factor was extracted. A measurement of the stability of the shielding in time and a measurement of the residual magnetic flux density along the axis of the tube was performed. A numerical simulation of the induced current in the shielding tube and the residual magnetic flux density along its axis was developed. The experimental results were compared to the predictions based on the numerical simulation.

For the measurements a dedicated apparatus consisting of a cryostat, filled with liquid helium, at a temperature of 4.2 K was developed and constructed at the Helmholtz-Institut Mainz (HIM). The shielding tube was equipped with a movable Hall probe, with a Zero-field Magnet on top. The external magnetic field was generated by a purpose-built superconducting solenoid, which can be mounted on top of the shielding tube.

An external magnetic flux density of 1 T was applied and shielded with a shielding factor of at least $3.2 \cdot 10^5$ with a 95 % confidence level. In a measurement over four days a penetration of it into the shielding tube could not be observed. The measurement of the residual magnetic flux density along the axis of the tube showed a shielding of the the central region of 80 mm (from total 150 mm shielding tube) up to 1 T. BSCCO is a good shielding material and can be used to shield the high magnetic field within the $\bar{\text{P}}$ANDA spectrometer.

Contents

Chapter 1

Introduction and overview

The standard model of particle physics is a theory that describes the elementary particles and interactions between those that we can observe today. The interactions are mediated by the so-called force particles. Today three fundamental interactions are well described by this model. The first one is the electromagnetic force, mediated by the photon that is e.g. responsible for the Coulomb force that makes two oppositely charged particles to attract each other, and two particles of the same charge to repel. It is also the interaction that underlies the electromagnetic field that we see as light in the visible regime. The second interaction is the week force, with attributed bosons W and Z. It governs some decay of particles, like the beta decay or fusion. This two forces could be unified in one theory, the electro-week force. It states that this two forces are two different aspects of the same force that unifies them above an energy of the order by 100 GeV. Nevertheless, for a long time it remained unclear, why the photon is massless, while the W and the Z have masses that exceeds 80 times that of the proton. Also the masses of the fermions cannot be explained without introducing a new field, called the Higgs field. The recently found Higgs particle that is a quantum of that field, solves this problem. The third interaction, the strong force is the binding force of the quarks in a hadron. The large proton mass compared to the masses of its constituents, the quarks, is still an open question. The structure of the hadrons, those particles built by quarks, is one of the main subjects of the study of the experiment antiProton ANnihilation in DArmstadt ($\bar{\text{P}}$ANDA), a detector at the particle accelerator Facility for Antiproton and Ion Research (FAIR). The gravitational force is not included as a quantized theory in the standard model of particle physics. It is the dominating interaction on large scales where the universe is electromagnetically neutral. Because of the relatively week interaction compared to the other three it is usually negligible at small scales.

Understanding the hadron structure is one of the main issues of studying the strong interaction described by Quantum Chromo-Dynamics (QCD). Especially the non-perturbative QCD is of great interest, since it is not well understood and can only be accessed experimentally to have an exact and model independent description. The proton is the only stable hadron and its structure has been largely studied. The internal structure of the proton can be expressed in terms of structure functions that provide a probe of non-perturbative QCD. They can be extracted from various processes involving a proton. Electron-proton elastic scattering or antiproton-proton annihilation gives access to the electromagnetic form factors. Electromagnetic form factors are quantities, which describe the distribution of the electric charge and magnetization within the proton. The Drell-Yan process and its cross-channel deep inelastic scattering allows for measuring parton distribution functions which describe how the momentum of a nucleon is divided among its constituents, quarks and gluons. The description of the structure functions is not yet complete and requires more experimental effort. This work is related to electromagnetic processes that can be observed in the $\bar{\text{P}}$ANDA experiment.

A fixed target particle experiment as $\bar{\text{P}}$ANDA is based on an accelerator for the particle beam and a detector with the target inside. The experimental setup will be introduced and a brief discussion on the physics program as it is foreseen will follow. In particular a transversely polarized target in $\bar{\text{P}}$ANDA is foreseen to access polarization observables, to have a more complete description of the structure functions like time-like form factors. A short overview on the observables are given and also the main principles of a polarized experiment provided.

In order to operate a transverse polarized target in $\bar{\text{P}}$ANDA, a transverse magnetic field is needed at the target region. The longitudinal 2 T magnetic field of the solenoid in the $\bar{\text{P}}$ANDA spectrometer has to be compensated. A very promising approach to this issue, is the shielding of a high magnetic field with a high-temperature superconducting shielding tube. First the physical properties of the shielding tube are introduced, followed by a detailed description of how the residual field of a shielding tube is calculated, and the results of a simulation. After an introduction to the experimental setup and the experimental procedure, the results of the measurements are presented, and compared to the simulation.

Chapter 2

The $\bar{\text{P}}$ANDA experiment at FAIR

The $\bar{\text{P}}$ANDA spectrometer [1] will be installed at the High Energy Storage Ring (HESR), a storage ring of the future FAIR accelerator facility at GSI Darmstadt [2]. The already existing accelerator facility at GSI will be used as an injector into the newly built complex of storage rings. The protons or ions are accelerated in several steps to provide the experiments with a high intensity and a high quality beam. $\bar{\text{P}}$ANDA will detect products of an annihilation reaction induced by a high intensity antiproton beam with momentum from 1.5 to 15 GeV/c. The average interaction rate is expected to reach $2 \cdot 10^7$ s^{-1}. The HESR stores a secondary beam of antiprotons, created by colliding protons on a target. The stored antiprotons can collide and annihilate with a fixed target in the $\bar{\text{P}}$ANDA spectrometer. The use of matter and antimatter as target and projectile makes it a unique probe of the standard model, since they can annihilate and produce pure energy.

2.1 Physics program of $\bar{\text{P}}$ANDA

The use of antiproton-proton annihilation allows for the access to all non-exotic quantum numbers that makes precise measurements of mass and width of known states possible. In contrast to proton-proton colliders, where the high discovery potential is in foreground, or electron-positron colliders that are limited to one quantum number (1^{--}). The $\bar{\text{P}}$ANDA experiment will offer a broad physics program thanks to the large detector acceptance, high resolution, tracking capabilities and excellent neutral and charged particle identification. Charmonium ($c\bar{c}$) spectroscopy, investigation of gluonic excitations, in-medium properties of mesons, gamma ray spectroscopy of hy-

pernuclei, and study of hadron structure are included and described here briefly.

2.1.1 Hadron spectroscopy and exotic hadrons

$\bar{\text{P}}$ANDA will search for gluonic excitations and do charmonium, D-meson and baryon spectroscopy.

Gluonic excitation are states where gluons can act as principle components . This can be a glue ball, where only gluons contribute to the overall quantum number, and hybrids, where also quarks and anti-quarks are involved. Because of a direct access to a full set of quantum numbers that are possible by proton-antiproton annihilation, $\bar{\text{P}}$ANDA is a favorable environment for gluonic excitations.

Charmonium states are mesons composed of a valence charm anti-charm pair. The decay modes and widths of states that are already known but grossly incomplete can be accessed with $\bar{\text{P}}$ANDA with high accuracy. Also missing states and the nature of newly discovered states will be investigated.

D-mesons are composed by one charm quark as the heavy constituent of this heavy-light system and a quark or an antiquark. Some of the measured states do not fit well into quark model predictions. This has risen theoretical and experimental interest in D-mesons. A determination of the decay widths of these states with $\bar{\text{P}}$ANDA, with a resolution down to values of 100 keV, will allow distinction between the different theoretical pictures for heavy-light systems.

The understanding of the baryon spectrum is the main goal of non-perturbative QCD. Whereas agreement of experimental data with quark model predictions is very poor. $\bar{\text{P}}$ANDA is well-equipped for a thorough baryon spectroscopy.

2.1.2 Hadrons in nuclear matter

The mass of an atom or an atomic nucleus is close to the sum of the masses of its constituents and the binding energy effect is rather small. In a nucleon this is no longer the case. The mass of a proton is 938 MeV/c^2 and the mass of its constituents, the up quark, 2.3 MeV/c^2, and down quark, 4.8 MeV/c^2 [3]. How is it possible to build protons and neutrons from these nearly massless blocks? In the strong interaction, as gluons also obtain a color, gluon-gluon interactions are also possible in a hadron and beside the valence quarks also a quark sea can exist. Can one understand hadron masses as a consequence of the motion and interaction of quarks? Chiral symmetry is a fundamental symmetry of QCD for massless quarks. In this theory, in

the interaction of quarks by gluon exchange, the orientation of the spin of the quarks with respect to their momentum, their chirality, is conserved. The chiral symmetry is broken, when the quarks change their chirality in the presence of a quark anti-quark pair. At high temperatures and high densities, the chiral symmetry can be partially restored. An experimental verification would be a measurement of a mass shift of a hadron in nuclear medium. Also a broadening of the resonance and other structures in it are expected. The experimental search until now was concentrated only on light quarks. An antiproton beam with a momentum up to 15 GeV/c will also include the charm sector.

2.1.3 Hypernuclei

By replacing an up or a down quark with a strange quark in a nucleon, a hyperon is formed. The study of nuclei containing strange baryons provides information on the nuclear structure and also on strange baryons in nuclear medium. With a beam of antiprotons in $\bar{\text{P}}$ANDA $\Lambda\Lambda$-hypernuclei can be formed to study the strong nuclear interaction [4]. With an internal target, production of Ξ-hyperons is expected, which can be used to form a bound state of a Ξ-hypernuclei in an absorber. The Ξ-hypernuclei can be converted into $\Lambda\Lambda$-hypernuclei and allow the investigation of double strange systems by performing gamma-spectroscopy on them. The two step formation of $\Lambda\Lambda$-hypernuclei requires a primary and a secondary interaction point. A modification of the inner part of the $\bar{\text{P}}$ANDA spectrometer is needed, where some detector components are removed or adapted to the hypernuclei-setup [5].

2.1.4 Nucleon structure

One main goal in hadron physics is the direct investigation of the nucleon structure via electromagnetic processes. Elastic electron nucleon scattering was used to determine the electric and magnetic form factors G_M and G_E in the space-like regime, where the form factors are real functions of the momentum transfer squared. The time-like regime can only be accessed via annihilation, where the form factors are complex. In this region experiments so far were carried out with low luminosity and individual values for G_M and G_E have remained undetermined. Therefore $\bar{\text{P}}$ANDA, as a high luminosity detector, is a brilliant tool for the determination of the time-like form factors. Because of their complex nature, for a complete determination also the relative phase between G_M and G_E is needed. For this purpose a transverse polarization of the target is highly desirable.

Another important issue in the field of electromagnetic processes are the generalized parton distribution functions (GPDs) [6]. They can be measured in processes like deep virtual compton scattering ($ep \to ep\gamma$) or wide angle compton scattering ($\gamma p \to \gamma p$). Their counterpart, called generalized distribution amplitudes (GDA), can be measured in the crossed channel process $p\bar{p} \to \gamma\gamma$. They give information about the longitudinal momentum and transverse position of the constituent quarks and gluons, in this way the 3-dimensional structure of the nucleon can be accessed.

2.1.5 Detector requirements from the physics case

The physics at $\bar{\text{P}}$ANDA described here requires a momentum range of the antiproton beam from the HESR of 1.5 and 15 GeV/c to have access to the targeted hadronic states (fig. 2.1). Concerning the electromagnetic processes another difficulty comes into play. The governing process in proton-antiproton annihilation is the pion production. The hadronic cross sections are 6 orders of magnitude higher than that of electromagnetic processes. For a successful suppression of background events a very good particle identification is required. For a high rate capability for $2 \cdot 10^7 \text{s}^{-1}$ interactions, a high data rate and consequently a high degree of radiation resistance is needed.

2.2 The $\bar{\text{P}}$ANDA spectrometer

$\bar{\text{P}}$ANDA (fig. 2.2) is a fixed target experiment with good particle identification, high energy and angular resolutions for charged particles and photons, good vertex reconstruction and excellent calorimetry. There are two main parts of the detector: A target spectrometer, consisting of a solenoid around the interaction region, and a forward spectrometer, based on a dipole magnet to reconstruct the momentum of particles emitted at forward angles. By this combination, an almost full coverage of the solid angle will be possible. Some components of the spectrometer will be mentioned here very briefly. A detailed technical description is given in ref. [9].

2.2.1 The HESR at FAIR

At the accelerator complex FAIR (fig. 2.3), protons from the LINAC will be accelerated up to 30 GeV/c and will collide with a copper or nickel target to produce antiprotons. After collecting those and pre-cooling, they will be stored in the HESR. At HESR, an antiproton beam in the momentum range between 1.5 and 15 GeV/c will be available. There are two operational

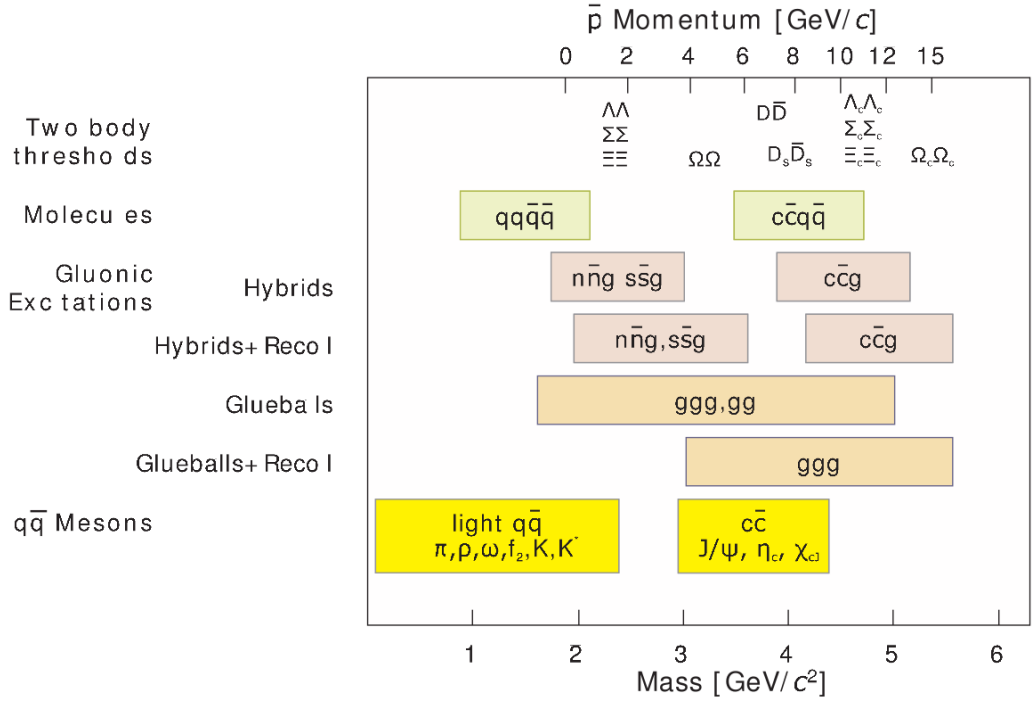

Fig. 2.1: Mass range of hadrons that $\bar{P}$ANDA is going to investigate. The upper scale indicates the required beam momentum range to have access to the mass region of the shown hadronic states. The HESR will provide a beam in the range of 1.5 and 15 GeV/c [8].

modes of the HESR that use either stochastic cooling or electron cooling [7]. Cooling of the beam means reducing the phase space occupied by the beam (emittance) and allowing a better momentum resolution. Stochastic cooling is a method where a feedback loop determines the signal of the deviation of particles in a bunch at one point of the storage ring. At a later point, by taking a shorter way across the ring, a correction to the bunch is given in a way that the particles in the bunch get closer to the desired trajectory. By successive application, the transverse momentum of the beam is reduced. Electron cooling exploits the momentum transfer of a low-emittance electron beam parallel to the antiproton beam. The electron beam is not circulating, it is generated just for one turn. By collisions of the electrons with the antiprotons, the antiproton beam emittance is reduced. In the high momentum resolution mode, electron-cooling is applied, allowing a very high momentum resolution $\delta p/p \sim 10^{-5}$ and a luminosity of $\mathcal{L} = 10^{31}\mathrm{cm}^{-2}\mathrm{s}^{-1}$. In the high luminosity mode, stochastic cooling will be used, and the momentum resolution is reduced to $\delta p/p \sim 10^{-4}$ while the luminosity reaches $\mathcal{L} = 2 \times 10^{32}\mathrm{cm}^{-2}\mathrm{s}^{-1}$.

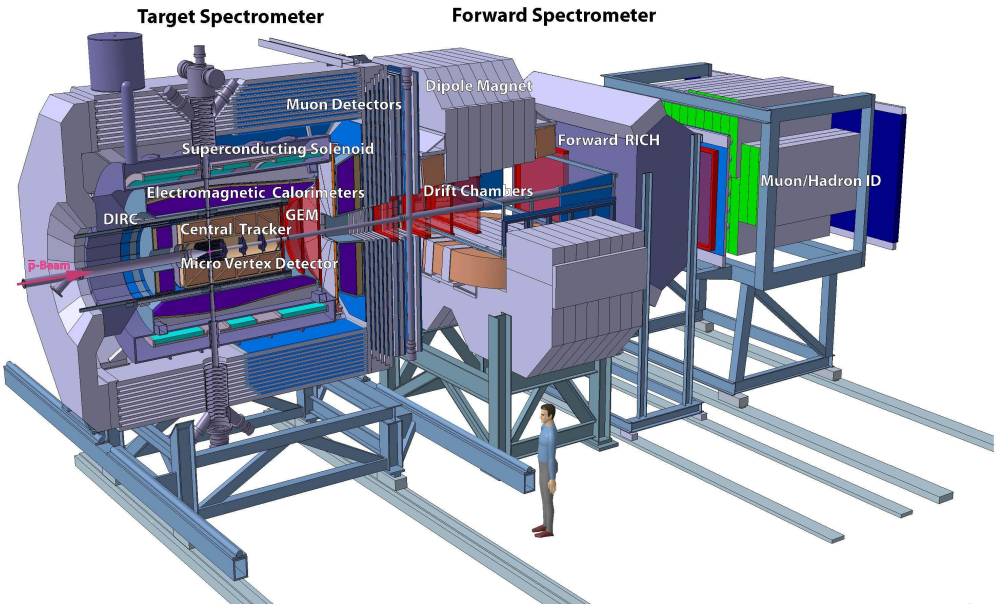

Fig. 2.2: $\bar{P}$ANDA Detector at HESR (FAIR). Shown are the target spectrometer, the forward spectrometer and the detector components described in the text [9]

2.2.2 Magnet systems

For the momentum resolution and identification of charged particles in the target spectrometer a superconducting solenoid with an inner diameter of 1.9 m and a length of 2.7 m is foreseen. It will provide a 2 T longitudinal magnetic field parallel to the beam axis, that will interact via the Lorentz force on charged particles and create curved tracks. From the tracking of the particles, their mass and velocity can be reconstructed. The lower the momentum of the particle, the higher its curvature in the magnetic field. In the ideal case the magnetic field should be uniform over the tracking volume. The homogeneity of the $\bar{P}$ANDA solenoid is planned to be better than 2 % over the volume of the tracker. The magnet in the forward spectrometer is a large-aperture dipole magnet which will provide a bending power of 2 Tm [10].

2.2.3 Target system

The target material required in $\bar{P}$ANDA for antiproton-proton experiments is a high density hydrogen target. It should provide a primary vertex point and at the same time fit in a small space by not worsening the vacuum in the beam pipe. Currently there are three types of targets foreseen depending

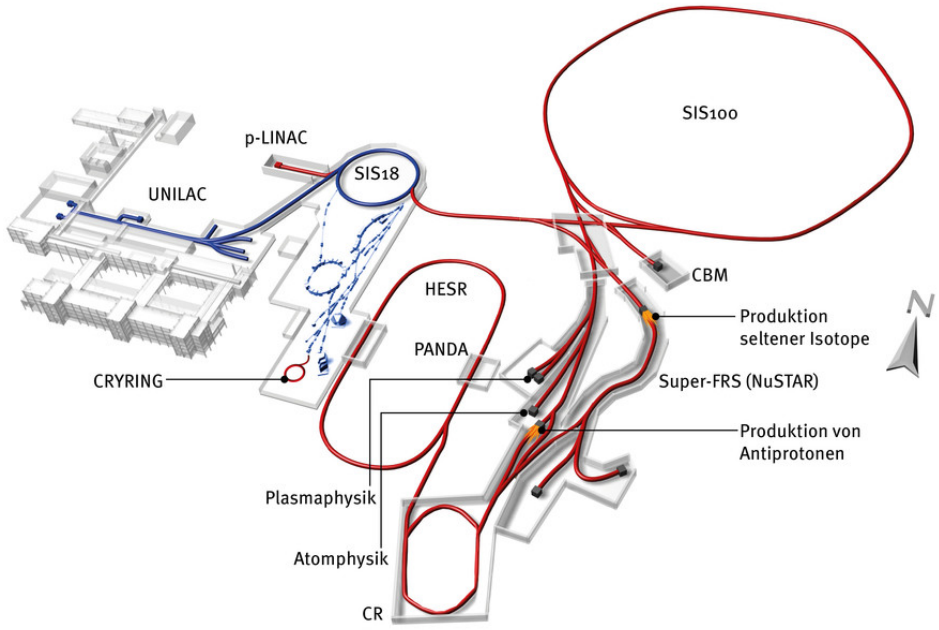

Fig. 2.3: The FAIR accelerator complex. The part already existing at the GSI site (blue) will be extended (red). The $\bar{P}$ANDA experiment at the HESR and also other experiments are shown [9].

on the requirements of the experiment. A cluster, a pellet, a fiber or a wire target [11,12]. The target pipe is perpendicular to the beam pipe. The cluster target is produced by pressing hydrogen gas through a nozzle that makes the gas to cool down and reach a supersonic speed. The gas condensates to nano-particles, the so-called clusters, with a thickness of $8 \cdot 10^{14}$ atoms/cm^2. A pellet target consists of micro-spheres of frozen hydrogen. This target type has a low divergence leading to an uncertainty of ± 1 mm of the interaction position with the beam. The average thickness of this target type is 10^{16} atoms/cm^2. The speed of 60 m/s of a pellet and a flow rate of 10000 pellets/s leads to a distance between two successive pellets on the order of a millimeter. A fiber or wire target would exploit the low beam emittance of the HESR best and will be needed for the physics with D mesons.

2.2.4 Detector components

The tracking system is the closest detector component to the interaction point. The micro vertex detector (MVD) is the innermost part of the tracking system. It allows the precise reconstruction of displaced vertices of short

lived particles with charm or strangeness content. Due to the magnetic field over the volume of the tracking system the particle momentum can be reconstructed by looking at the curvature of the tracks of charged particles. The information about the energy loss of a particle facilitate the particle identification.

In addition to the observables mentioned above a DIRC (detection of internally reflected cherenkov radiation) detector and a ToF (time of flight) detector will provide additional information. Cherenkov radiation is emitted by particles traveling through a medium with a faster velocity than the velocity of light in that medium. The angle is related to the velocity of the particle. The ToF measures the arrival time of the particle at two points at a distance, and by this the velocity and makes it possible to distinguish between particles of the same momentum but different mass.

Between the solenoid and the tracker, the electromagnetic calorimeter (EMC) measures the energy deposit of particles in its sensitive volume in an energy range of 10 MeV to 15 GeV. Electrons and photons will deposit their full energy by an electromagnetic shower, hadrons will lose just a fraction of their energy by a hadronic shower and muons penetrate the calorimeter almost without energy loss and have to be detected in the muon detector outside of the solenoid. Another issue for the EMC is, it has to be designed in a way that it can resist the hard radiation due to the high luminosity. For the particle identification the information of several independent detector components are correlated.

Particles emitted in the forward direction close to the beam pipe will be detected in the forward spectrometer equipped with a dipole magnet and the components described above placed in this part of the detector.

Chapter 3

Transversely polarized target measurements in $\bar{\text{P}}$ANDA

The electromagnetic form factors in the space-like regime that can be accessed by scattering electrons on protons, are real. In the time-like region, when a proton and an antiproton annihilates into an electron-positron pair, the form factors are complex. An unpolarized measurement in the time like region gives access to their moduli squared. For a full determination one needs additional information about the relative phase from a polarized measurement. A transversely polarized target in $\bar{\text{P}}$ANDA would allow the first-time extraction of their relative phase, opening a new window for investigating the nucleon structure.

3.1 Description of the nucleon structure

A complete description of the nucleon structure can be given in terms of structure functions, describing electromagnetic processes in the space-like and the time-like region. A scattering process for the former, and an annihilation for the latter is required involving a lepton pair or a photon and a nucleon or an additional meson. They are connected by crossing symmetry and the observables are counterparts in different kinematic regions.

- Generalized distribution amplitudes can be extracted from the annihilation channel of the wide angle Compton scattering [13]. And the measurement of transition distribution amplitudes from the process proton-antiproton annihilation and electron-positron pair production with an additional neutral pion [14].

- In the Drell-Yan production a quark of the proton and an antiquark

of the antiproton annihilate, creating a virtual photon, which then decays into an antilepton-lepton pair. From this process transverse momentum dependent (TMD) parton distribution functions (PDFs) can be extracted. At leading twist 8 TMD PDFs are needed to fully describe the nucleon structure [15, 16].

- With an unpolarized measurement in $\bar{\text{P}}$ANDA the Boer-Mulders functions can be measured which describes the distribution of polarized partons in unpolarized hadrons.

- If the target could be polarized transversely, also the Transversity and Sivers functions are accessible. These describe the distribution of polarized and respectively unpolarized partons in polarized hadrons. Comparing the Transversity and the Boer-Mulders functions from the Drell-Yan production to the Transversity and the Boer-Mulders functions from the crossed process semi inclusive deep inelastic scattering is a test of their universality.

3.2 Electromagnetic form factors

After the identification of an electron as an elementary particle in an experiment with cathode rays in 1897 by J.J. Thomson, he proposed that the negatively charged electrons (he called them "corpuscles") where distributed inside an atom in a sea of positive charge like plums in a bowl of pudding [17]. This was believed until the first scattering experiment to investigate the nucleon structure was carried out. In a scattering experiment of alpha particles generated by the radioactive decay of radium showed a behavior that contradicted this picture. In his analysis of the gold foil experiment published in 1911 by E. Rutherford in [18], he described the differential cross section for an alpha particle scattered from a static point charge. In a case where the incident particle is an electron, the differential cross section is:

$$\left(\frac{\mathrm{d}\sigma}{\mathrm{d}\Omega}\right)_{\mathrm{Ruth}} = \frac{Z^2\alpha^2}{16E_k^2\sin^4(\theta/2)}, \tag{3.1}$$

where $\mathrm{d}\Omega = 2\pi\mathrm{d}\cos\theta$ is the solid angle of the scattered electron at polar angle θ in the laboratory frame, $\alpha = \frac{e^2}{4\pi}$ is the electromagnetic coupling constant (e is the elementary charge), E_k is the kinetic energy of the incident electron, Z is the atomic number of the target. From this result he concluded that the atoms in the foil consist of a positively charged nucleus that is concentrated in the center with a relatively high mass. Otherwise

the alpha particles would have passed the foil with a few minor deflections. The Rutherford cross section (eq. 3.1) is accurate in the case of a scattering of non-relativistic, point-like, spin zero particles, without recoil of the target nucleus. The scattering is non-relativistic, if the kinetic energy of the involved particles is much smaller than their rest mass.

The differential cross section of the Mott scattering [19], by taking into account the spin of the electron and treating it as relativistic, is

$$\left(\frac{\mathrm{d}\sigma}{\mathrm{d}\Omega}\right)_{\mathrm{Mott}} = \frac{Z^2\alpha^2\cos^2\left(\frac{\theta}{2}\right)}{4\epsilon_1^2\sin^4\left(\theta/2\right)} \tag{3.2}$$

ϵ_1 is the total energy of the incident electron in the laboratory frame. The term $\cos^2\left(\frac{\theta}{2}\right)$ comes from the spin of the electron. If the target is not point-like but has a finite extension, the charge distribution of the target introduces a correction term called form factor [20, 21]. The scattering amplitude due to a distributed charge is the scattering amplitude due to a point multiplied with the form factor $F(\mathbf{q}) = \int \rho(\mathbf{x}) e^{\mathbf{q}\cdot\mathbf{x}} \mathrm{d}\mathbf{x}$. The differential cross section, in the case of a non-relativistic recoil of the proton, becomes

$$\frac{\mathrm{d}\sigma}{\mathrm{d}\Omega} = \left(\frac{\mathrm{d}\sigma}{\mathrm{d}\Omega}\right)_{\mathrm{Mott}} \left| \int \rho(\mathbf{x}) e^{\mathbf{q}\cdot\mathbf{x}} \mathrm{d}\mathbf{x} \right|^2 \tag{3.3}$$

where $\rho(\mathbf{x})$ is the charge distribution at distance $\mathbf{x}$ from the center of the proton, and $\mathbf{q}$ is the momentum transfer from the scattered electron. The form factor $F(\mathbf{q})$ is the Fourier transform of the charge distribution (in case of a non-relativistic proton). The spin of the target is not taken into account in eq. 3.3.

Form factors can be defined for any non-point-like particle. In the following we will focus on the proton form factor. The number of form factors for a spin-1/2 particle is two. Considering that the electromagnetic coupling has to fulfill Lorentz-invariance, charge- and parity conservation. There is also a contribution to the cross section coming from the magnetic moment of the proton. Hofstadter [21] described the cross section based on formalism by Foldy [22] and Rosenbluth [23] as

$$\frac{\mathrm{d}\sigma}{\mathrm{d}\Omega} = \left(\frac{\mathrm{d}\sigma}{\mathrm{d}\Omega}\right)_{\mathrm{Mott}} \frac{\epsilon_1}{\epsilon_2} \left[F_1^2 + \tau F_2^2 + 2\tau \tan^2(\theta/2)(F_1 + F_2)^2\right] \tag{3.4}$$

where ϵ_1 and ϵ_2 is the energy of the incident and scattered electron in the laboratory system, respectively. F_1 and F_2 are the Dirac and Pauli form

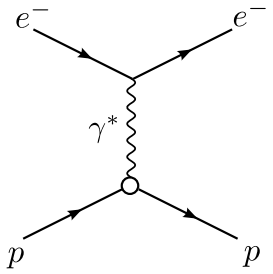

Fig. 3.1: Feynman diagram of the scattering process of an electron and a proton

factors as functions of the momentum transfer squared q^2, $\tau = \frac{q^2}{4m^2}$ and m is the mass of the nucleon.

It is convenient to use the Sachs form factors G_M and G_E which are linear combinations of the Pauli and Dirac form factors [24]

$$G_E = F_1 - \tau F_2, \quad G_M = F_1 + F_2. \tag{3.5}$$

They are related to the charge and magnetization distribution. Particularly, if $q^2 = 0$, $G_E = 1$ and $G_M = \mu_p$, where $\mu_p = 1.4106067873 \cdot 10^{-26}$ J/T is the proton magnetic moment [25]. At large q^2, G_M and G_E are phenomenological probes for the internal structure of the proton. At high q^2, where the interaction between the quarks gets weaker, perturbative QCD (pQCD) can be applied. At low q^2 QCD cannot be solved exactly and the transition region to pQCD is unclear too. By measuring G_M and G_E over a large q^2 range the transition region between perturbative QCD and non-perturbative QCD can be accessed experimentally.

3.2.1 Space-like form factors

The form factors in the space-like region when $q^2 < 0$ can be extracted by two different measurement methods both based on the elastic scattering process shown in fig. 3.1. One is called the Rosenbluth separation method [23], the other one the polarization transfer method [26], that allows the determination of the ratio of the form factors. The Rosenbluth separation method consists in measurement of the unpolarized differential cross section of the electron proton scattering (a detailed description can be found in ref. [28]):

$$\frac{\mathrm{d}\sigma}{\mathrm{d}\Omega} = \left(\frac{\mathrm{d}\sigma}{\mathrm{d}\Omega}\right)_{\text{Mott}} \frac{\varepsilon_1}{\varepsilon_2} \frac{1}{\mathcal{E}(1+\tau)} (\tau G_M^2 + \mathcal{E} G_E^2) \tag{3.6}$$

$$\mathcal{E}^{-1} = 1 + 2(1+\tau)\tan^2(\theta/2) \tag{3.7}$$

A reduced cross section can be defined:

$$\sigma_{red}(\theta, q^2) = \tau G_M^2 + \mathcal{E} G_E^2. \tag{3.8}$$

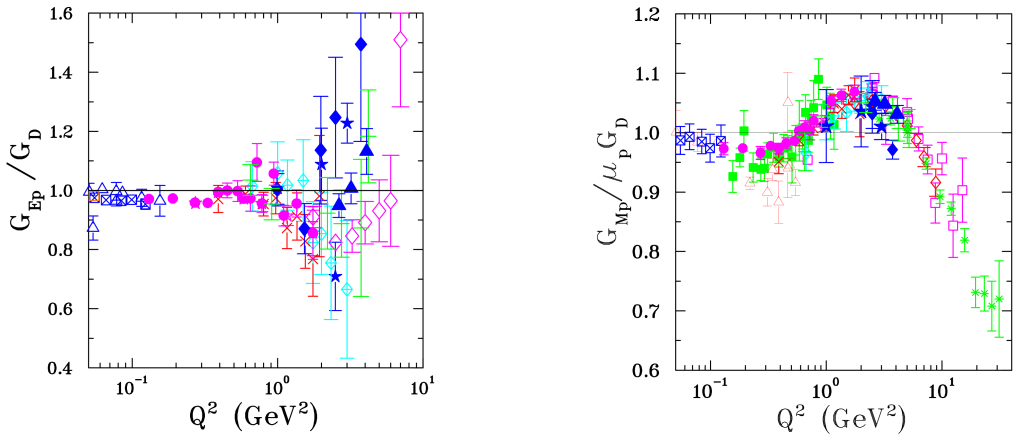

Fig. 3.2: Form factors G_M and G_E as a function of $Q^2 = q^2$ in terms of the dipol function $G_D = (1 + q^2/0.71 GeV^2)^{-2}$, extracted with the Rosenbluth method [28].

One can extract G_E^2 as the slope and τG_M^2 as the y-intercept of a linear fit of the function $\sigma_{red}(\theta, q^2)$ depending on $\mathcal{E}$. The data obtained with the Rosenbluth separation method are shown in fig. 3.2. There are two main disadvantages of this method: At large q^2 the cross section is dominated by G_M. Also exchange of more than one virtual photon in the scattering process is neglected. The development of polarized electron beams and proton polarimetry allowed for measurements of polarization observables. Starting in 1998 three measurements were carried out at Thomas Jefferson National Accelerator Facility of a measurement of the ratio of the form factors. They followed the suggestion of Akhiezer and Rekalo [26, 27], measuring the polarization of the recoil proton after scattering would be more sensitive to G_E rather than of an unpolarized cross section as in the Rosenbluth separation method. Moreover, the contributions from radiative corrections in this method are minimised, since polarization observables are ratios of cross sections. From the simultaneous measurement of the transverse P_t and longitudinal P_l component of the polarization of the recoil proton one can extract the ratio of the form factors:

$$R = \frac{G_E}{G_M} = -\frac{P_t}{P_l}\frac{\varepsilon_1 + \varepsilon_2}{2m}\tan(\theta/2). \tag{3.9}$$

Figure 3.3 shows the discrepancy of the results obtained with the two different methods. Until now this discrepancy is not yet fully understood.

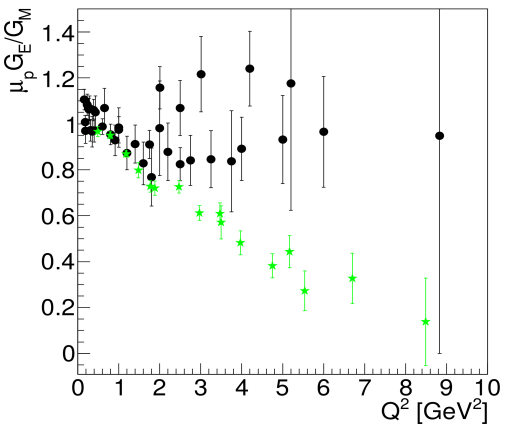

Fig. 3.3: Comparison between the two different methods to obtain proton form factors by electron-proton scattering. The black points are the result of the Rosenbluth separation method. The green stars are results from measurements via the proton recoil polarization method [33].

3.2.2 Time-like form factors

The proton form factors for $q^2 > 0$ (time-like region) can not be accessed in the electron-proton scattering process, where $q^2 < 0$ (space-like). They can be measured in the process where a proton and an antiproton annihilate and an electron-positron pair is produced (e.g. at LEAR [29]) or vice versa. The latter case, based on e^+e^--annihilation, has been investigated e.g. at BaBar [30] and BESIII [31]. These data suffered from low precision and are also partly inconsistent with each other within their total uncertainties. $\bar{\text{P}}$ANDA as a detector with near to 4π angular coverage and a high luminosity will be able to measure with higher accuracy and cover also higher values of q^2. The measurements of the ratio of the time-like form factors are shown in fig. 3.4 a) as black symbols [34–37]. The colored symbols are obtained by individual extraction of G_M and G_E via the $\bar{\text{P}}$ANDA simulation package [38] with the hypothesis of the ratio $R = \frac{|G_E|}{|G_M|} = 1$ [39]. In fig. 3.4 b) [40] the same simulation was done for the similar process involving a muon pair in the final state. More details are given in ref. [38]. For the unpolarized process:

$$p + \bar{p} \rightarrow e^- + e^+, \tag{3.10}$$

see the Feynman-diagram in fig. 3.5, the differential cross section in the center-of-mass system is

$$\left(\frac{d\sigma}{d\Omega}\right)_0 = \mathcal{N}[(1 + \cos^2\Theta)|G_M|^2 + \frac{1}{\tau}\sin^2\Theta|G_E|^2] \tag{3.11}$$

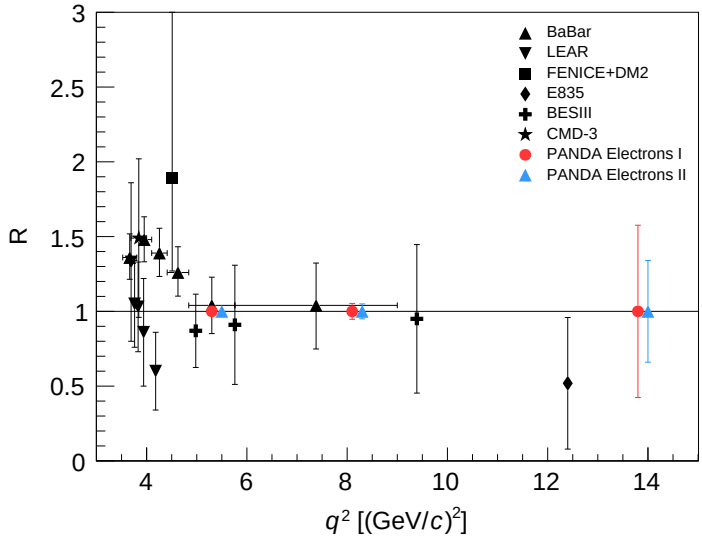

(a)

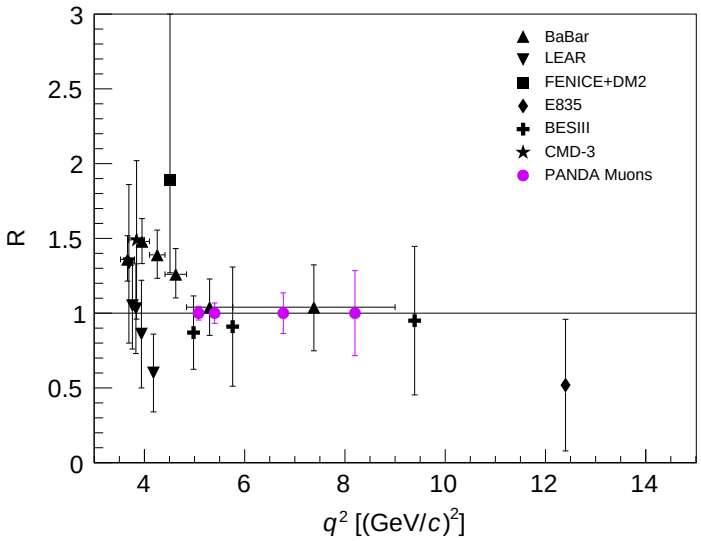

(b)

Fig. 3.4: a) World data of time like form factor ratio in proton-antiproton annihilation and electron-positron pair production [34–37] compared to simulations as it can be measured with $\bar{P}$ANDA (PANDA $p\bar{p} \to e^+e^-$) [38]. b) Simulation of time like form factors involving a muon pair in the final state (PANDA $p\bar{p} \to \mu^+\mu^-$) [40]. The simulations assume an integrated luminosity of $2fb^{-1}$.

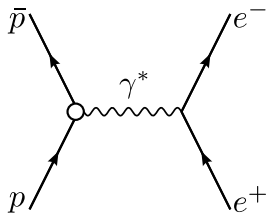

Fig. 3.5: Proton-antiproton annihilation and electron positron pair production process.

$$\mathcal{N} = \frac{\alpha^2}{4\sqrt{q^2(q^2-4m^2)}} \tag{3.12}$$

$$\alpha = e^2/(4\pi) \simeq 1/137 \tag{3.13}$$

with the Sachs form factors G_M and G_E, $q^2 = 4E^2$, $\tau = \frac{q^2}{4m^2}$ with the antiproton energy E in the center of mass frame and an approximation of zero electron mass. m is the mass of the proton. Θ is the angle between the antiproton and the electron in the center-of-mass frame. This formula was first shown in ref. [41]. The cross section depends only on the moduli squared of the complex Sachs form factors G_M and G_E. To have access to the relative phase between G_M and G_E, a measurement of the transverse single spin polarization observable is needed. By polarizing the proton transversely in the same process the polarized differential cross section is:

$$\left(\frac{d\sigma}{d\Omega}\right)_0 A_{1,y} = \frac{\mathcal{N}}{\sqrt{\tau}} \sin 2\Theta \, \mathrm{Im}(G_M G_E^*), \tag{3.14}$$

and $A_{1,y}$ is the single spin asymmetry by polarizing transverse to the production plane. This was derived in ref. [42]. By fixing the energy and the scattering angle, $\mathrm{Im}(G_M G_E^*)$ can be extracted from a polarized measurement:

$$|G_M||G_E| \left(\cos\left(\Phi_M - \Phi_E\right) + \mathrm{i} \sin\left(\Phi_\mathrm{M} - \Phi_\mathrm{E}\right)\right) \tag{3.15}$$

$$\mathrm{Im}(G_M G_E^*) = |G_M||G_E| \sin\left(\Phi_M - \Phi_E\right) \tag{3.16}$$

where Φ_M and Φ_E is the phase of the magnetic, electric form factor, respectively. If $|G_M|$ and $|G_E|$ are known from an unpolarized measurement, the relative phase can be determined. This is true for a polarized measurement where the target is 100% polarized. How to take a less polarized target into account, is described in the next section.

3.3 Polarization principles

The design and development of a transverse polarized target for $\bar{\mathrm{P}}$ANDA needs to be investigated in details. Nevertheless, the development of a shield-

ing against the 2 T longitudinal magnetic flux density of the solenoid of the $\bar{\text{P}}$ANDA spectrometer at the target region is the first step towards a transverse target polarization in $\bar{\text{P}}$ANDA, and therefore the main focus of this thesis. In this section basic considerations of target polarization are given.

3.3.1 Optimizing the performance of a polarization experiment

The first approaches of producing beams of polarized hydrogen atoms were reported at the International Symposium on Polarization Phenomena of Nucleons (Basel, 1960) [43]. A summary of polarized target experiments is given in tab. 3.1. A detailed description of polarization principles and techniques can be found in [44]. The main quantities that have to be considered in a polarization experiment are summarized here.

In a fixed target experiment the counting rate is:

$$N = \mathcal{L}\frac{d\sigma}{d\Omega}\Delta\Omega, \tag{3.17}$$

where $\frac{d\sigma}{d\Omega}$ is the differential cross section of interest and $\Delta\Omega$ the detector solid angle. The luminosity

$$\mathcal{L} = In_t \tag{3.18}$$

is defined as the product of the beam current I (number of beam particles per second) and the target thickness n_t (number of target particles per volume times the target length). $\mathcal{L}$ determines the accuracy and how fast an experiment can be carried out. In a storage ring, like HESR at FAIR, to guarantee a sufficient long lifetime of the beam, the target is usually very thin (typically $< 10^{15}$ atoms/cm^2). If the experiment requires a polarized target, one of the main issues is the maximization of the degree of polarization of the target P_t.

In an ensemble of nuclei with nuclear spin 1/2 the degree of nuclear target polarization is defined as

$$P_t = \frac{n_{+\frac{1}{2}} - n_{-\frac{1}{2}}}{n_{+\frac{1}{2}} + n_{-\frac{1}{2}}}, \tag{3.19}$$

where $n_{+/-\frac{1}{2}}$ is the number of nuclei with spin $+/-\frac{1}{2}$. The experimentally measured quantity is the counting rate asymmetry

$$\epsilon = \frac{N_\uparrow - N_\downarrow}{N_\uparrow + N_\downarrow}, \tag{3.20}$$

where $N_{\uparrow\downarrow} = \frac{1}{2}(N_\uparrow + N_\downarrow)(1 \pm P_t A)$ is the counting rate for an experiment with a target, polarized transversely to the production plane. The plus sign is for the positive, the minus for the negative polarization. The asymmetry A can than be extracted from

$$A = \frac{1}{P_t}\epsilon \tag{3.21}$$

meaning that $A = \epsilon$ if the target is 100% polarized. Thus measuring P_t is necessary for the determination of A. If the target contains a fraction f_{pol} of polarizable and $f_{unpol} = (1 - f_{pol})$ of unpolarized nuclei, the dilution factor f due to scattering from unpolarized material has to be taken into account:

$$f = \frac{f_{pol}\sigma_{pol}}{f_{unpol}\sigma_{unpol} + f_{pol}\sigma_{pol}}, \tag{3.22}$$

where σ_{unpol} is the cross section for an unpolarized measurement. For the comparison of target materials a simpler expression, without the dependence on the cross section, can be applied. In this case

$$f = \frac{\text{number of polarizable nuclei}}{\text{total number of nuclei in the target material}}. \tag{3.23}$$

This quantity is 1 in the case of H and D gas targets, 0.33 for ^{3}He targets, and ranges between 0.13 and 0.5 for solid H and D target materials. The uncertainty in the asymmetry A is

$$(\Delta A)^2 = \left(\frac{1}{f}\frac{1}{P_t}\Delta\epsilon\right)^2 + \left(A\frac{\Delta P_t}{P_t}\right)^2 + \frac{\Delta f}{f}(A)^2, \tag{3.24}$$

and $\Delta\epsilon = (N_\uparrow + N_\downarrow)^{-\frac{1}{2}}$. The main contribution is the first term.

If T is the running time of the experiment ΔA can be written as

$$\Delta A \approx \frac{1}{f}\frac{1}{P_t}\frac{1}{\sqrt{T n_t I}} \tag{3.25}$$

which gives a running time of

$$T \approx \frac{1}{f^2 P_t^2 n_t I \Delta A^2}. \tag{3.26}$$

The running time, required to fulfill a predefined accuracy ΔA in the asymmetry measurement, becomes short, if a quantity called "figure of merit"

$$FOM_{ext} = n_t P_t^2 f^2 \tag{3.27}$$

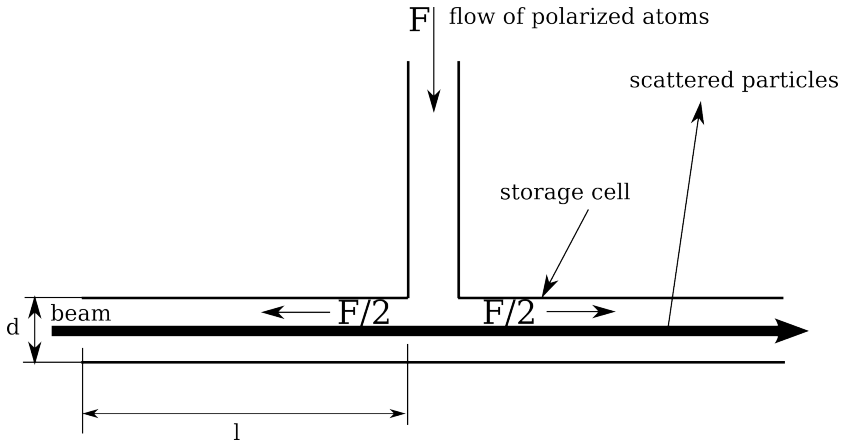

Fig. 3.6: Generalized storage cell target. F is the flow of atoms that interact with the beam.

is large. Therefore the performance of an external target experiment can be expressed by this quantity. For a storage cell target (fig. 3.6) the thickness is

$$n_t = \rho l, \tag{3.28}$$

where l is the length of the storage cell along the beam line. The density ρ of the gas in the cell is

$$\rho = \frac{F}{C}, \tag{3.29}$$

with the flow F (number of atoms injected per second) and the conductance C (volume per second). Since the conductance is proportional to the velocity of the atoms, it is also proportional to $\sqrt{T}$ where T is the temperature of the wall of the cell. Thus the "figure of merit" for a gas storage cell target is

$$FOM_{cell} = F\sqrt{T}^{-1} P_t^2 f^2, \tag{3.30}$$

which implies that the cell should be cooled in order to obtain a better figure of merit. the cooling of the cell. Some examples of gas target setups can be found here ref. [45].

3.3.2 Polarization techniques

The method called dynamic nuclear polarization, discovered by Erb, Motchane, and Ubersfeld (ref. [46]) and Abragam and Proctor (ref. [47]), led to the development of a variety of target systems used in polarization experiments. The first experiment with a polarized target was done by Abragam et al. at

Saclay in 1962 [48] followed by Chamberlain et al. at Berkeley [49]. The principle of nuclear polarization is the same for all target systems and consists of two main steps, described in detail in ref. [50]. The first step is to achieve an atomic polarization in a strong magnetic field. Since the magnetic moment of the nucleus is much lower than that of the electron, the nuclear polarization is poor. In a second step, by triggering the hyperfine interaction of the atomic spin with the nuclear spin, the polarization of the electrons can be transferred to a polarization of the nuclei.

The main categories of nuclear species for polarized targets are the following: hydrogen (H) or deuteron (D), both are used as solid state targets in experiments in an external beam, i. e. the beam is extracted from the accelerator and the collision with the target happens externally. Or as internal gas targets in a storage ring. Helium (^{3}He) gas targets can be used in external or internal experiments (tab. 3.1).

H and D solid state targets are doped with radicals to create paramagnetic centers. At very low temperature a strong magnetic field achieves a high atomic polarization in the radicals. Irradiation of microwaves changes the electron spin and the nuclear spin simultaneously. By a much faster relaxation of the electrons, they can act on another nucleus again, and this process leads to a polarization of the nuclei.

For a H or D gas target the atomic polarization is produced by selecting spin states by a magnetic field with a gradient. The irradiation of radio frequency exploits then the atomic polarization to polarize the nuclei that can be filtered by a sextupole magnet and injected into a storage cell. The storage cell ensures the multiple crossing of the target particles through the beam and thus a higher interaction rate. Nevertheless the recombination and depolarization due to wall collisions have to be suppressed.

For a ^{3}He target a circularly polarized laser beam is used to bring rubidium atoms into an excited state. Collisions between the rubidium and ^{3}He transfers then the atomic to a nuclear polarization.

The degree of polarization is measured by nuclear magnetic resonance in the case of solid state targets and ^{3}He. The polarization of H and D gas is measured with a Breit-Rabi polarimeter.

Since $\bar{\text{P}}$ANDA needs an internal target, a very thin target is required. The main issue is to maximize the transverse target polarization. This requires a vanishing longitudinal magnetic field after shielding, or a longitudinal residual field, as small as possible. The discussion of a particular target type is much too early at this stage of the study, since the specifications of the shielding system determines the conditions for further components.

Laboratory	Gas H, D	^{3}He	Solid H, D	Physics goal	Ref.
DESY (Hamburg)	•	•	-	NSS	[51, 52]
BINP (Novosibirsk)	•	-	-	NSS	[53]
TSR (Heidelberg)	•	-	-	TD	[54]
NIKHEF (Amsterdam)	•	•	-	NSS FF	[55]
IUCF (Indiana)	•	•	-	NSS	[56]
MIT-Bates (Massachusetts)	•	•	-	NSS FF	[57–59]
JLAB (Virginia)	-	•	-	NSS FF	[60]
LAMPF (Los Alamos)	-	•	-	TD	[61, 62]
MAMI (Mainz)	-	•	•	NR, GDH, FF	[63, 64]
TJNAF (Newport News)	-	•	•	NSS, NR, GDH, FF	[65]
TRIUMPF (Vancouver)	-	•	-	TD	[66, 67]
SLAC (Stanford)	-	•	•	NSS	[68]
CERN (Genava)	-	-	•	NSS	[69]
ELSA (Bonn)	-	-	•	NR, GDH	[70, 71]
GRAAL (Grenoble)	-	-	•	GDH	[72]
LEGS (Brookhaven)	-	-	•	GDH	[73]
SPRING8 (Osaka)	-	-	•	GDH	[74]

Tab. 3.1: Summary of polarized target experiments and their scientific purpose. NSS: Nucleon spin structure, NR: Nucleon resonances, FF: Form factors, GDH sum rule derived by Gerasimov [75] and Drell and Hearn [76], TD: Target development.

Chapter 4

Realization of a shielding of a magnetic field

A transverse polarized target in the $\bar{\text{P}}$ANDA spectrometer requires a shielding against the 2 T longitudinal field, generated by a solenoid, in a volume that is big enough for a polarized target, whereas the rest of the detector volume remains largely unaffected. The residual field at an applied external field of 2 T should be as low as possible, to maintain a strong degree of transverse polarization. Another important issue is to minimize the material budget introduced by the shielding tube. To be able to detect particles by the surrounding detectors, the energy loss, given by the thickness of the shielding tube in units of radiation length, should be minimized. This means to lower the material budget, introduced by the shielding tube.

A passive high-temperature superconducting shielding tube is the most promising solution to meet this two requirements. The choice of Bismuth-2 Strontium-2 Calcium-1 Copper-2 Oxid (BSCCO) has the following reason. Fagnard et al. [88] used BSCCO-2212 compound, a melt cast high-temperature superconductor, formed to a hollow cylinder. They shielded 1 T with a shielding factor of 1000 at the temperature T = 10 K. Lowering the temperature to T = 4.2 K will increase the current density even more leading to a higher shielding factor at the same external field.

Beside a qualitative introduction to the principles of a shielding tube, some important physical properties of a BSCCO-2212 shielding tube are given here.

4.1 The superconducting state

A comprehensive description of superconductivity is given in ref. [77]. The most important properties of a superconductor, in particular in form of a hollow cylinder, are given here. The very low electrical resistance and the high current density is the reason for choosing a superconductor for magnetic flux shielding. The vanishing electrical resistance in superconductors below a transition temperature was discovered in 1913 by Heike Kamerlingh-Onnes and called superconductivity [78]. He measured the resistance of mercury at liquid helium temperature 4.2 K and found it to be less than $10^{-6}\Omega$.

Although this is not the property used for the shielding effect, the other remarkable property of superconductors should be mentioned here, too. Expulsion of the magnetic field from the material, as soon as the material is below a transition temperature, was discovered in 1933 by Meissner and Ochsenfeld [79]. The so called Meissner-effect, is independent of the magnetic field inside the material, before the probe has become superconducting.

In 1935, Lev Shubnikov [80] discovered that in some alloys superconductivity has two different phases shown schematically in fig. 4.1.

Because of the Shubnikov-phase the current density and second critical magnetic field in type II superconductors can reach very high values. Some of them, called high-temperature superconductors, have a transition temperature well above the boiling point of liquid nitrogen and a high second critical magnetic field. For example, the transition temperature for BSCCO-2212 is 94 K and the second critical magnetic field of more than 60 T [81]. The values for the critical current density increase with decreasing temperature. Therefore, the maximum current density in high-temperature superconductors are reached at very low temperatures. They can be considered for shielding a high magnetic field.

4.2 Generation of a shielding field

The main issue is to create a shielding magnetic field, opposing to the external field in the whole volume, in which a polarized target should be installed. In the ideal case, the flux density has the same value but with opposite sign in this region, so that the superposition vanishes. The field of a shielding solenoid, surrounding the target region, would result in a poor shielding effect. A large inhomogeneity would be introduced, since the field at the ends of the solenoid would drop to approximately half of the value of that in the center. At the same time, the homogeneity of the external field is better then 2%, therefore, the residual field will follow the inhomogeneity of the shielding

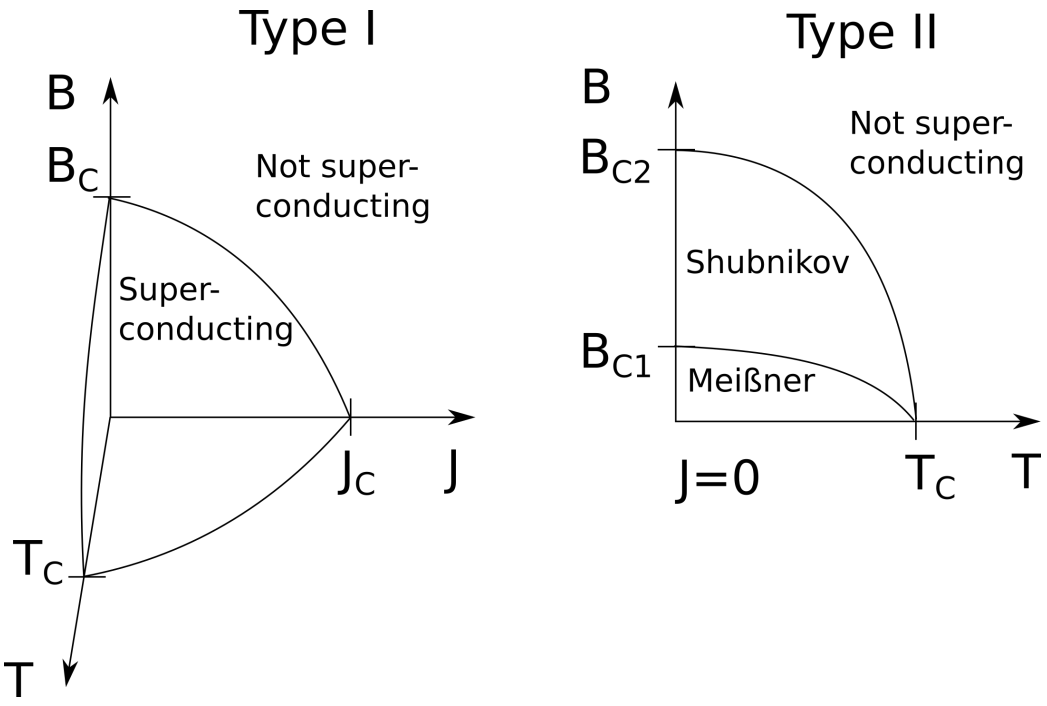

Fig. 4.1: Schematic picture of the phase diagram of the two different types of superconductors. The phase diagram for type one is shown on the left side. The superconducting state is limited by a surface that is spanned by the three variables the temperature T, the magnetic field B and the current density J that is applied to a superconductor. The three critical values T_C, B_C and J_C determine the phase boundary. The phase below the surface, where the magnetic field is expelled from the material, is called the Meissner-phase. The second type is shown on the right. The area between the two critical values, the first B_{C1} and second B_{C2} critical magnetic field, is called the Shubnikov-phase, where magnetic field can enter the material but superconductivity is still observed. B_{C2} can be much higher as B_C or B_{C1}. Typical values of B_C in type I superconductors are well below 1 T. Whereas B_{C2} in type II can be at the order of 10 T to 100 T.

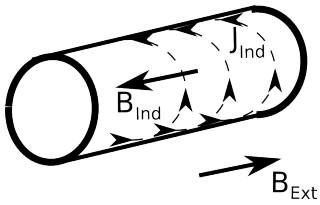

Fig. 4.2: Principle sketch of a shielding tube for shielding a magnetic field inside a perfectly conducting tube. The variation of the magnetic flux inside a perfect conductor (0 resistance) is zero, independent of the variation of the external flux. The induced shielding current J_{ind} by an external field B_{ext} creates a field B_{ind} of the same value but opposite direction inside the shielding tube.

solenoid, and it would make it very hard to maintain a polarization.

One needs a solution, where the opposing magnetic field is not exclusively at one point equal to the negative value of the external field, but follows the external field also in a larger volume. A shielding tube can be viewed as many superconducting rings in a row. If a superconducting ring is placed in an the external field, where a magnetic field is varied in time (ramping the field from zero to a maximum value), the current induced by the external field generates itself a magnetic flux in the plane of the ring that cancels the external flux. Thinking of a tube instead of a ring, the residual field will be of the desired quality. The electrodynamics of this process will be described in this chapter and also in sec. 5.

The current needed for a homogeneous opposing field in a shielding tube is created in the following way. A variation of the magnetic flux inside a conducting ring leads to an induced current $I_0 = I(t = 0)$ as a function of time that decays exponentially, depending on the electrical resistance R and the inductance L of the ring. A shielding tube is a concatenation of single rings.

$$I(t) = I_0 \mathrm{e}^{-\frac{R}{L}t} \tag{4.1}$$

If R is close to zero, as in a superconductor, a near to steady current will be observed after application of an external field. This current will create an opposing field and the flux from inside is expelled as described in fig.4.2. A quantitative description will be given in sec.5.1.3. The current is distributed in a way that the residual field is homogeneous. This is a consequence from Faraday's law of induction and that the current is not constrained to flow homogeneously with respect to the axis of the tube. Also no additional current supply is needed to drive the shield. The electromotive force created by the external field is enough to operate the shielding tube. Since a high-temperature superconductor is not exactly an ideal conductor, penetration

of flux at a certain value of the external magnetic flux and degradation of the shielding with time can be observed.

4.3 Characteristics of a shielding tube

Current density. Shielding of a magnetic field means to reduce the external field to an acceptable residual value. The maximum shielding current determines the maximum magnetic field that can be shielded. The maximum current density specifies the wall thickness that is needed to obtain the desired shielding current. By application of an external field that exceeds the shielded field, a residual field appears in the tube that cannot be removed by lowering the external field below the shielded field. To understand this behavior, a phenomenological theory of a high-temperature superconductor exposed to a magnetic field was introduced by C. P. Bean [82]. He suggested that as a result of a time varying magnetic field, a current density J_C is induced, that is either zero or has a constant value. The shielding current is then obtained by multiplying the current density with the wall thickness, that is carrying the current. In the other parts of the material the current is zero. With this model one can calculate the flux density distribution inside a superconductor. It can also explain the hysteresis-like behavior of the induced current and residual field after application and removal of an external field. This is shown in fig. 4.3 and fig. 4.4. The weakness of this model is the assumption of an infinitely extended material, plus that the current density is independent of the value of the external field. The hysteresis-like behavior will become important, when the residual field is measured. Especially, if the external field is increased and decreased again, one has to take into account, that some field might remain as described above. Also the earth magnetic field and other local fields are maintained in the shielding tube, after it is cooled below a transition temperature.

The average induced current density J_{ind} in a shielding tube and its thickness determines the maximum magnetic field that can be shielded. The average current density is defined as to create a magnetic flux density that compensates the external flux density at the center in an equivalent solenoid with the thickness of the shielding tube. This is an approximation in the case of a solenoid (shielding tube) with a large length over diameter ratio. The average induced current density J_{ind} in the shielding tube at the applied external magnetic field B_{ext} is shown in tab.4.1. The current density is a function of the temperature and was determined for BSCCO-2212 in ref. [88] with a shielding factor of 1000. It is shown in fig.4.5. At a fixed temperature one can estimate the thickness d of the material necessary to shield the

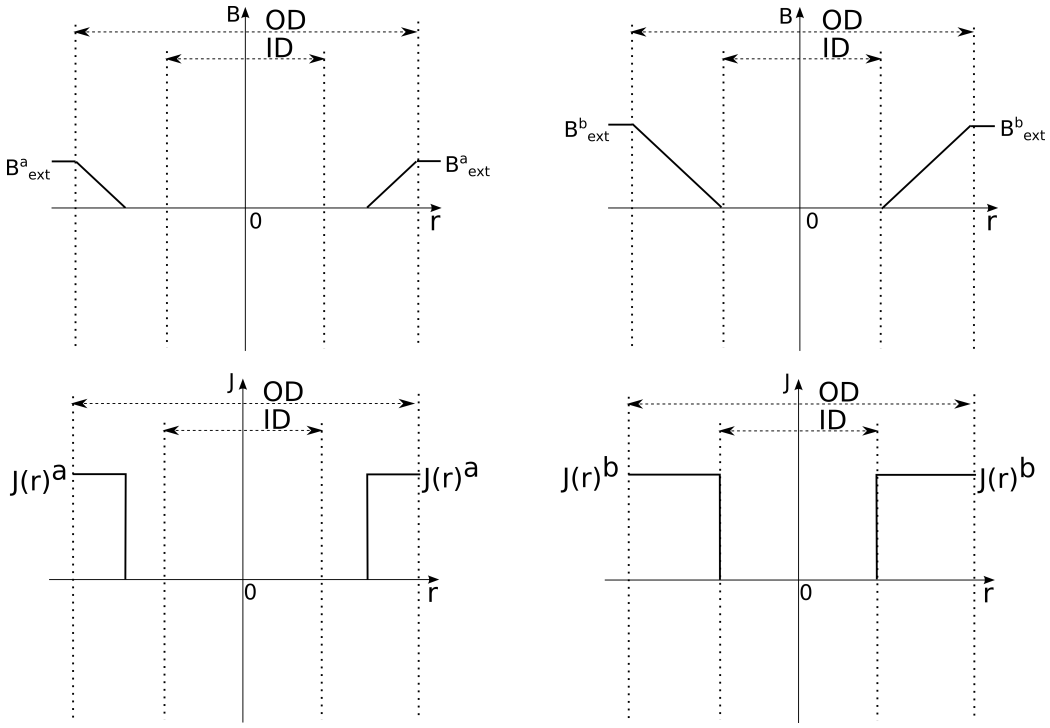

Fig. 4.3: Model of a high-temperature superconducting shielding tube of infinite length, as suggested by C. P. Bean [82]. Originally he considered an infinite long slab of thickness D, that can be applied to the case of an infinitely long shielding tube with a wall thickness of $\frac{OD-ID}{2} = d = D/2$, within the simplifications of his model. The horizontal axis of the plots is the spacial direction r perpendicular to the wall of a superconducting shielding tube. The vertical axis of the upper plots show the magnetic field B and the lower plots the corresponding current density $J(r)$. This sketch and fig. 4.4 show four states of the shielding tube in time as the external field is increased and decreased. The first state is shown in the left plots, where the external field B^a_{ext} is applied parallel to the axis of the shielding tube (vertical direction in the plot). The field decreases linearly as it penetrates the material until it vanishes. The second state is shown in the right plots, where the external field reaches a value B^b_{ext}, so that it vanishes exactly at $r = ID/2$ The external field is shielded up to this value. The corresponding shielding current density J is either a constant or zero. As the external field rises, the shielding current is created by the induced current density times the wall thickness occupied by the current.

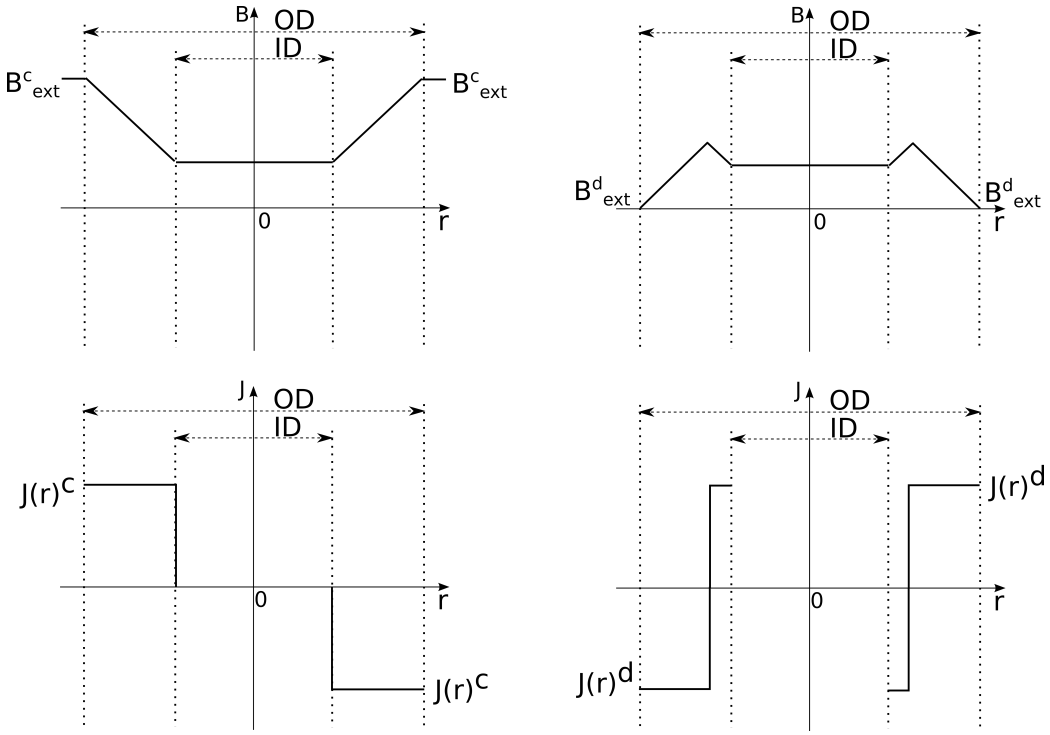

Fig. 4.4: Third and fourth states of a superconducting shielding tube during increasing and decreasing the external magnetic field. The first and second states are shown in fig. 4.3. The third state is shown in the left plots, where the external field rises above B^b_{ext}. The difference enters the inner part of a shielding tube unaffected. The last state is shown in the two plots on the right. This is the consecutive decrease of the external field to $B^d_{ext} = 0$. A trapped flux B^d_{res} remains in the superconductor. The shielding current J^d in the shielding tube after removing the external field is not zero. The residual field can be lowered or removed by applying an opposite external field. This is the hysteresis-like behavior of the shielding tube.

Average current density			
$J_{ind} = \frac{B_{\text{ext}}}{\mu_0 d} \cdot 10^{-8}$	**Symbol**	**Unit**	**Definition**
	J_{ind}	A/cm^2	induced average current density
	d	m	thickness of the shielding tube
	μ_0	Vs/Am	vacuum permeability
	B_{ext}	G	external magnetic flux density

Tab. 4.1: Formula for the calculation of the average current density.

magnetic field B_{ext}. If B_{ext} exceeds this value, the difference will enter the shielding tube. If one is interested in the induced current vs. the position on

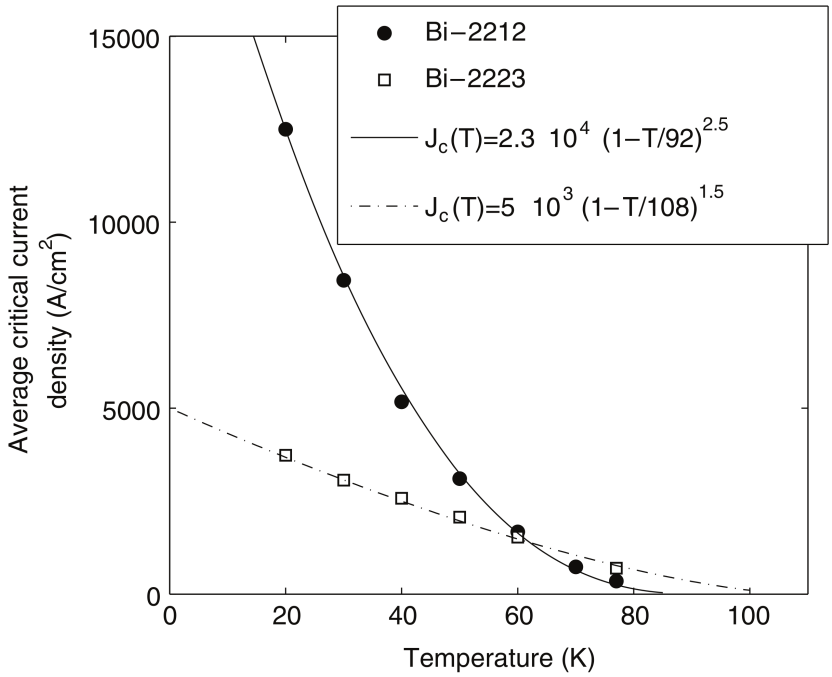

Fig. 4.5: Temperature dependence of the current density of BSCCO-2212 and BSCCO-2223 at a shielding factor of 1000 [88]. Our choice of BSCCO-2212 is due to the higher current density in this material at low temperatures. The fitting functions of the current density versus the temperature are also shown.

the axis without averaging over the length, the Bean model is insufficient. One needs to apply a calculation as in sec. 5.1.3.

Mechanical stress on the shielding tube. The Lorentz force on the current in the shielding tube is defined as

$$\vec{F}_L = I \oint d\vec{l} \times \vec{B} \tag{4.2}$$

in presence of a magnetic flux density B and a current I along the infinitesimal line element dl. We consider the z component of the magnetic field parallel to the shielding tube axis. This magnetic field results in a pressure from outside to inside the shielding tube, as we will see in the following calculation. The x and y components of the magnetic field are low compared to the dominating z component. They create a force along the axis and cannot apply a pressure on the shielding tube. Since the current is everywhere

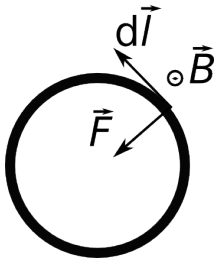

Fig. 4.6: Cross section of the shielding tube. Lorentz force F_L on the current in presence of a magnetic flux density B and a current I along the infinitesimal line element $d\vec{l}$.

Lorentz force			
	Symbol	**Unit**	**Definition**
$F_L = J_{ind} dL_{st} l B^z_{\text{ext}}$	J_{ind}	A/cm^2	induced average current density
	B^z_{ext}	T	z component of the external magnetic flux density
	d	m	thickness of the shielding tube
	l	m	circumference of the shielding tube $l = 2\pi r_{st}$
	L_{st}	m	length of the shielding tube

Tab. 4.2: Formula for calculation of the Lorentz force.

perpendicular to the magnetic flux density along the integration region, we get

$$F_L = I l B^z_{\text{ext}} = J_{ind} dL_{st} l B^z_{\text{ext}} \tag{4.3}$$

The symbols are defined in tab. 4.2. The Pressure is

$$P = \frac{F_L}{a_{\text{surface}}} \tag{4.4}$$

where $a_{\text{side}} = L_{st} l$ is the surface area of the side of the shielding tube. The pressure on the shielding tube due to the magnetic field determines the maximum field that can be applied without destruction of the shielding tube. An additional holding tube can stabilize the shielding tube mechanically. For example, at an external field of 1.4 T the induced average current density in a shielding tube of 3.5 mm thickness is $J_{ind} = \frac{B^z_{\text{ext}}}{\mu_0 d}$ is 3.2 kA/cm^2. The pressure due to the Lorentz force (fig. 4.6) is thus $F_L = 1.6$ MPa.

4.3.0.0.1 Material budget. The material budget of the BSCCO-2212 shielding tube can be estimated in the following way. Traversing the thickness d of the shielding tube, consisting of the BSCCO-2212 material and the

holding tube, a particle with the initial energy E_0 will have an average energy

$$E(d) = E_0 e^{-\frac{d}{X_0}} \tag{4.5}$$

due to radiation loss. This energy loss has to be reduced to a minimum. The radiation length X_0 of a material divided by the density is defined as the mean length to reduce the energy of an electron by the factor 1/e (e is Euler's number) when the electron is propagating through the material [83]

$$X_0 = \frac{716.4A}{Z(Z+1)\ln\frac{287}{\sqrt{Z}}} \frac{\mathrm{g}}{\mathrm{cm}^2} \tag{4.6}$$

with the atomic mass A and atomic number Z. In this case the shielding tube consists of the composite material $Bi_2Sr_2CaCu_2O_8$ (BSCCO-2212), and therefore we have to add the reciprocal of the single radiation lengths X_i of every atom weighted by w_i, the atomic mass of the element relative to the total mass of the BISCO-2212 molecule. We obtain X_0 from the following formula

$$\frac{1}{X_0} = \sum \frac{w_i}{X_i} \tag{4.7}$$

The density of BSCCO-2212 is $6\frac{\mathrm{g}}{\mathrm{cm}^3}$ and the radiation length divided by the density is 1.5 cm. The same calculation for the holding tube (Mn20%, Ni20%, Cu 60%) with a density of $8.25\frac{\mathrm{g}}{\mathrm{cm}^3}$ leads to a radiation length of 1.6 cm. The BSSCO tube is (3.5 ± 0.2) mm and the holding tube (2 ± 0.1) mm thick. This leads to a relative energy loss I_{rel} of $I_{rel} = 1 - e^{-\frac{0.35}{1.5} - \frac{0.2}{1.6}} = 0.3$. The electrons lose 30% of their initial energy by traversing the shielding tube.

Operating the shielding tube in this way, concerning the thickness of the tube itself and the holding tube, results in a very high energy loss. Choosing this shielding tube material, the energy loss can only be reduced by the following options: Lowering the operating temperature could increase the shielding current density, that means less material is needed to achieve the same shielding current. Try to minimize the amount of material for the holding tube by ensuring the mechanical stability of the shielding tube at the same time.

4.4 Grain boundaries in sintered high-temperature superconductors

BSCCO-2212 is categorized as a cuprate superconductor. Its structure is shown in fig. 4.7 [77]. It consists of two CuO_2 layers close to each other, and

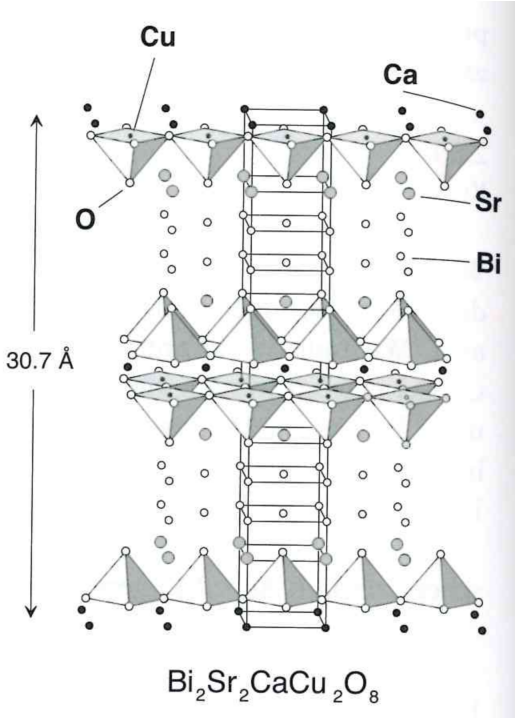

Fig. 4.7: Molecular structure in a BSCCO-2212 superconductor crystal [77]. The atoms bismuth (Bi), strontium (Sr), calcium (Ca), copper (Cu) and oxygen (O) and their position in the crystal structure are shown. One elementary cell occupies a volume of a few nanometers. The conducting copper layers alternate with isolating bismuth and strontium.

between them is a layer of calcium. This sandwich structure alternates with two layers of bismuth and two layers of strontium. The superconductivity builds up in the close layers of CuO_2 by forming cooper-pairs. The oxygen content in BSCCO-2212 is a critical issue since one oxygen excess takes one electron from CuO_2 leaving a hole behind as a charge carrier. In a BSCCO-2212 crystal molecule are $8+x$ oxygen atoms. At an optimal value of $x = 0.16$ (0.16 holes per cu-atom) the transition temperature T_C is 90 K. For smaller x values T_C is very low and decreases also for larger values, until it vanishes at $x = 0.27$. After this point BSCCO-2212 is a normal conductor at all temperatures.

For manufacturing a shielding tube, the starting material of a superconducting compound is mixed and melted between 1000 °C and 1200 °C, followed by an annealing procedure between 750 °C and 850 °C [84]. An important issue is the existence of grain boundaries in sintered material. These are formed by misalignment of neighboring superconductor crystals

and the current density is limited by the inter-granular current. An example is the investigation for bicrystals of the high-temperature superconductor Yttrium-1 Barium-2 Copper-3 Oxid (YBCO) in ref. [85]. The melt cast processed BSCCO-2212 contains a partially textured region which can carry a high current density [84].

Chapter 5

Numerical simulation of a shielding tube

In addition to the experimental investigation of the shielding of an external field with a superconducting shielding tube, it is of great importance to provide support in form of a numerical calculation. On the one hand it can be used for including a field map into particle tracking simulations. On the other hand, it offers a cheap and fast tool to optimize and design a final geometry of the shielding tube.

The induced current in a shielding tube which creates the shielding magnetic counter-field, depends on the position along the axis of the tube and is inhomogeneous. It is high at the edges and low towards the center. A simple Biot-Savart calculation with the assumption of a homogeneous current in the whole tube is not sufficient to calculate the residual magnetic field.

Therefore, the induced current is calculated by using the exact forms of the Maxwell equations in integral form and the Biot-Savart law. This is an alternative method to the finite element method (FEM) calculation (appendix A) that solves the differential form of the Maxwell equations on a mesh, by discretization of the volume. The FEM calculation is optimized for simulation of complicated geometries. Since all shapes involved in the calculation are cylindrically symmetric, a simplified model can be used. An additional advantage of the calculation described here is the modular setup which allows for calculation of single steps separately. If e.g., one is interested in the optimization of the length of the shielding tube, the external magnetic flux can be calculated only once. To make the calculations more effective, the induced current is flowing on the surface of the shielding tube.

5.1 Introduction to the calculation method

5.1.1 Equations in a quasistatic electromagnetic field

The simulation is based on the calculation of the induced current by a varying magnetic field. The self and mutual inductances in a system of ideally conducting current loops can be used to describe the current density distribution in a superconducting tube. The principles are described in ref. [86]. For creating a static magnetic field in a solenoid a rise of the field is required from zero to the maximum value. Since the change in the magnetic field during this procedure is slow, the wavelength of the electromagnetic field is very long. The lengths of the involved structures are much shorter than this wavelength, so the Maxwell equations can be reduced to the quasistatic case where the displacement current $\frac{\partial \epsilon_0 \vec{E}}{\partial t}$ is negligible. Since there are no static electric sources $\boldsymbol{\nabla} \cdot \epsilon_0 \vec{E} = 0$, too. The governing equations in this case are therefore

$$\boldsymbol{\nabla} \times \vec{E} = -\frac{\partial \vec{B}}{\partial t} \tag{5.1}$$

$$\boldsymbol{\nabla} \times \vec{B} = \mu_0 \vec{j} \tag{5.2}$$

$$\boldsymbol{\nabla} \cdot \epsilon_0 \vec{E} = 0 \tag{5.3}$$

$$\boldsymbol{\nabla} \cdot \vec{B} = 0 \tag{5.4}$$

by using the operators for the curl $\boldsymbol{\nabla}\times$ and the divergence $\boldsymbol{\nabla}\cdot$, the electric field $\vec{E}$, the magnetic flux density $\vec{B}$, the current density $\vec{j}$, the vacuum permittivity ϵ_0 and the vacuum permeability μ_0.

5.1.2 Geometry of the external magnet and shielding tube

The geometrical parameters of the external magnet and the shielding tube are shown in tab. 5.1. This calculation method can be applied to any size of the shielding tube or external magnet. Since we want to compare the results from the simulation and the measurement described in chapter 6, we use the same geometry here as in the experiment. The symbols that we use for the fields are defined in tab. 5.2. In fig. 5.1 the arrangement of the external magnet and the shielding tube is visualized. In fig. 5.2 the discretization of the shielding tube into rings is shown.

External magnet	Length	L_{em}	138 mm
	Radius	r_{em}	31.5 mm
	Number of windings per layer	N_{em}	460
	Number of layers	n_0	22
	Distance between windings	d_w	0.3 mm
Shielding tube	Length	L_{st}	150 mm
	Radius	r_{st}	25 mm
	Number of divisions	N_{st}	3750
	Distance between neighboring rings	d_R	0.04 mm
	Thickness of the shielding tube	d	3.5 mm

Tab. 5.1: Geometrical parameters of the external magnet and the shielding tube in the calculation.

	Magn. flux density $\vec{B}$	**Magn. flux** $\int_a \vec{B} \cdot d\vec{a}$	**Current**
External	$\vec{B}^{ext}$	F^{ext}	I^{ext}
Induced	$\vec{B}^{ind}$	F^{ind}	I^{ind}
Residual	$\vec{B}^{res}$	F^{res}	-

Tab. 5.2: Symbols used in the calculation documentation for the external magnetic flux density and flux that is created by the external current and the induced quantities. The residual quantities are a superposition of the external and induced ones.

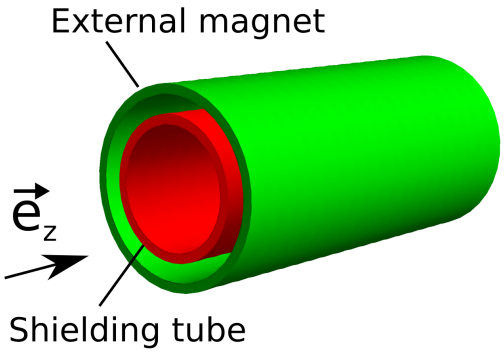

Fig. 5.1: Geometrical arrangement underlying the calculations. The shielding tube is inside the external magnet as shown in the picture.

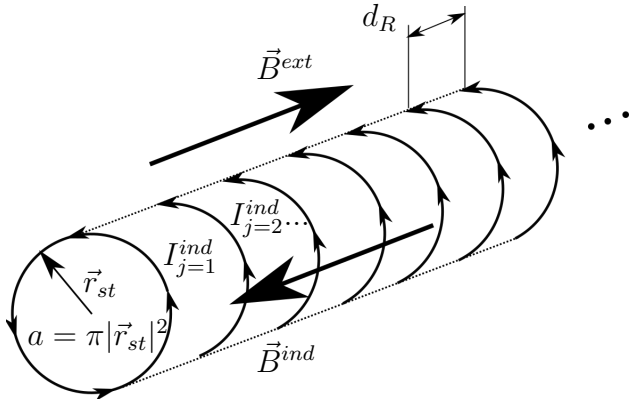

Fig. 5.2: Sketch of the method of dividing the tube in N_{st} equidistant rings at distance d_R. Each of them carrying a current I^{ind}_j, $j = 1...N_{st}$ induced by $\vec{B}^{ext}$ creating an induced magnetic field $\vec{B}^{ind}$. We calculate I^{ind}_j and $\vec{B}^{ind}$ as shown in the text. The induced current density J_{ind} in the tube is then a function of the ring position.

5.1.3 Compensation of the magnetic flux

The property of a superconducting hollow cylinder of shielding a magnetic flux can be explained by application of Faraday's law to an ideally-conducting circular ring. It can be shown that the external magnetic flux is compensated.

We assume that the superconductor is an ideal conductor and from this the following behavior concerning the induced flux can be derived. A constant magnetic flux inside the shielding tube can be shown by an argumentation with Faraday's law.

$$-\frac{d}{dt}\int_a \vec{B}\cdot d\vec{a} = \oint_{\partial a} \vec{E}\cdot d\vec{l} \tag{5.5}$$

In the case of an ideally conducting ring or tube as shown in fig. 5.3

$$\oint_{\partial a} \vec{E}\cdot d\vec{l} = 0 \tag{5.6}$$

Since the tangential component of the electric field $\vec{E}$ is everywhere zero on an ideal conductor, the scalar product $\vec{E}\cdot \mathrm{d}\vec{l}$ vanishes. It follows that also the right-hand side, which is the change of the magnetic flux through a surface, must be zero

$$-\frac{d}{dt}\int_a \vec{B}\cdot d\vec{a} = 0 \tag{5.7}$$

which leads to the central statement that the magnetic flux is constant

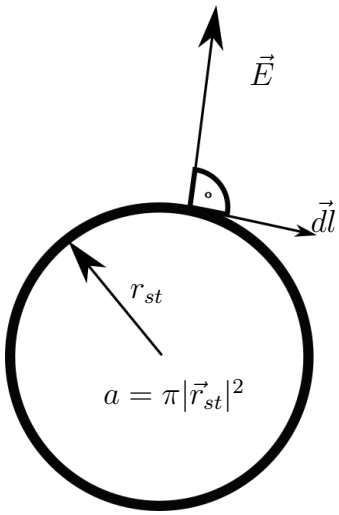

Fig. 5.3: Sketch of an ideally conducting current loop. The electric field $\vec{E}$ is perpendicular to the surface of the loop at every point on the loop. It can be shown, by the use of Faraday's law, that the change of the magnetic flux inside the loop is zero, independent of the change of the external magnetic flux.

through a surface bounded by an ideal conductor. Because

$$\int_a \vec{B} \cdot d\vec{a} = F^{res} = F^{ext} + F^{ind} \tag{5.8}$$

it follows, if the external magnetic flux in the shielding tube is zero at the beginning of the process and is changed afterwards, the flux in the inner part of the shielding tube remains zero. It is constant, if there was already a magnetic flux present before it got superconducting. [1] By assuming $F_{res} = 0$ it follows that

$$F^{ind} = -F^{ext} \tag{5.9}$$

The external magnetic flux is compensated by the induced flux inside the shielding tube. This will be the magnetic flux that we use for our calculation of the induced current.

5.1.4 Calculation steps and simplifications

The calculation steps are shown in fig. 5.4. From the parameters of the external magnet, the external magnetic flux inside the shielding tube can be calculated. This is equal to the induced flux. The relationship between the

[1] In the literature one can find that the first situation is referred to as "zero field cooled (zfc)" and the latter one "field cooled (fc)".

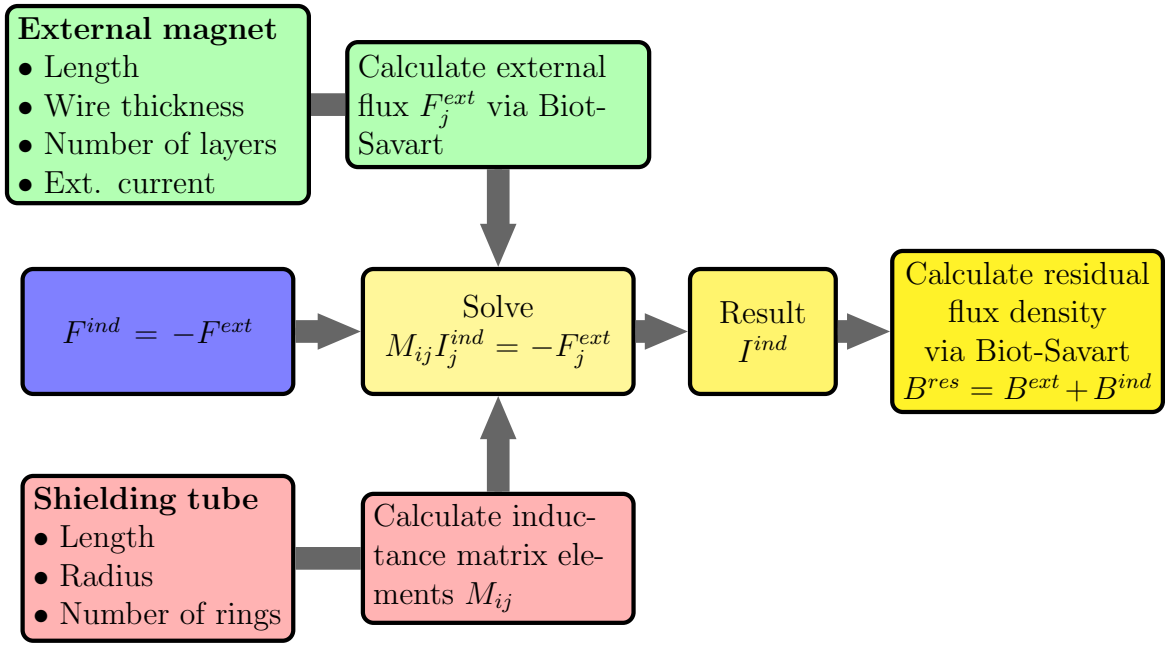

Fig. 5.4: Calculation steps. Symbols are described in the text.

induced flux in a ring and the induced current in that ring is given by the inductance. By solving a matrix equation an induced current to each ring can be assigned. The induced magnetic flux density can then be calculated from the induced current by using Biot-Savart. By superposition one can calculate the residual magnetic flux density.

The following simplifications are used: First, the induced current is not limited. Second, we also neglect the finite wall thickness of the shielding tube. The induced current is confined to the surface of the cylinder.

5.2 Calculation of the magnetic flux density

The first step in the calculation is the calculation of the external magnetic flux density. In a later step, this formulation will also be used to calculate the induced magnetic flux density. Let us consider a winding of the external magnet in the x-y plane (fig. 5.5) that creates a magnetic flux density in the x-z plane. This has a simple geometry of a circular closed loop in approximation to a helix of a very small height of one wire diameter compared to the total length of the external magnet. The z component of the magnetic flux density at position $P(x, z)$ $\overline{OP} = r(\vec{x}, z)$ can be calculated via the Biot-Savart law

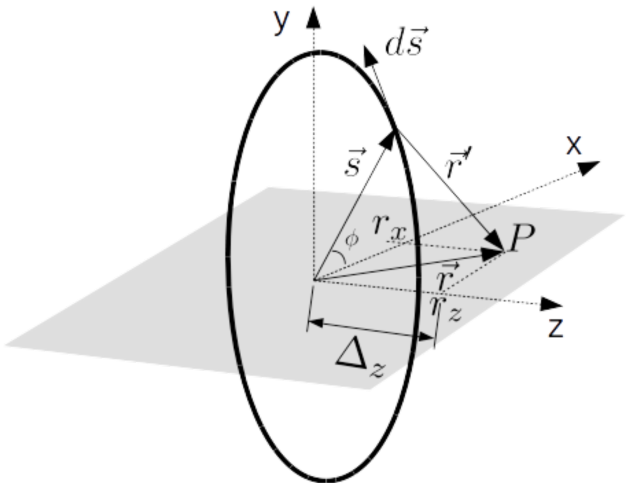

Fig. 5.5: One winding of the external magnet in the x-y plane. The symbols are used for the calculation of the external magnetic flux density. The magnetic flux density generated by the induced current in sec. 5.5 is calculated in the same way.

[86]

$$B_z(\vec{r}) = \frac{\mu_0}{4\pi} I \oint \frac{(d\vec{s} \times \vec{r}')_z}{|\vec{r}'|^3}. \tag{5.10}$$

The parametrization of the winding is

$$\vec{s}(\phi) = (R\cos\phi, R\sin\phi, z_0), \tag{5.11}$$

where $\phi \in [0; 2\pi]$ and R is the radius of the winding. The tangent $d\vec{s}(\phi)$ that describes the current density

$$d\vec{s} = R(-\sin\phi, \cos\phi, 0)d\phi. \tag{5.12}$$

The vector $\vec{r}'(\phi)$ that connects $\vec{s}(\phi)$ with the observation point $P(x, z)$ is

$$\vec{r}' = \vec{r} - \vec{s} = (r_x - R\cos\phi, -R\sin\phi, r_z - z_0). \tag{5.13}$$

And the z component of the cross product

$$(d\vec{s} \times \vec{r}')_z = (R^2 - Rr_x\cos\phi)d\phi. \tag{5.14}$$

The square of the length of of $\vec{r}'(\phi)$ is

$$|\vec{r}'|^2 = r_x^2 - 2r_xR\cos\phi + R^2 + (r_z - z_0)^2. \tag{5.15}$$

Therefore we can write the z component of the magnetic flux density of a winding as

$$B_z^w(r_x, \Delta_z) = \frac{I^{ext}\mu_0}{4\pi} \int_0^{2\pi} \frac{(R^2 - Rr_x\cos\phi)}{(r_x^2 - 2r_xR\cos\phi + R^2 + \Delta_z^2)^{\frac{3}{2}}} d\phi, \tag{5.16}$$

with the relative distance $\Delta_z = r_z - z_0$.

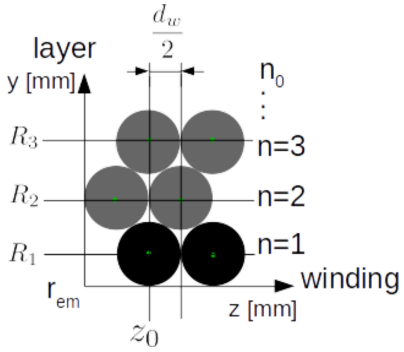

Fig. 5.6: Example of the layout with 2 windings and 3 layers. With this structure an ideally winded solenoid is calculated.

The external magnet has 460 windings and 22 layers ($n_0 = 22$). This is taken into account by a summation over the layers. Fig. 5.6 shows an example with 2 windings and 3 layers for visualizing the layout cross section of the windings and layers. two variables are defined (that describe the horizontal and vertical position of a single winding on the axis of the magnet and in radial direction) that are functions of the layer number n

$$z_n = ((n-1) \bmod 2)\frac{d_w}{2} \tag{5.17}$$

$$R_n = r_{em} + \frac{d_w}{2} + (n-1)\sqrt{3}\frac{d_w}{2} \tag{5.18}$$

with $z_0 = z_1$.

The formula for the z component of the magnetic flux density of one winding is defined then as

$$B_z^{wn}(r_x, \Delta_z) = \frac{I^{ext}\mu_0}{4\pi} \sum_{n=1}^{n=n_0} \int_0^{2\pi} \frac{({R_n}^2 - R_n r_x \cos\phi)}{(r_x^2 - 2r_x R_n \cos\phi + {R_n}^2 + (\Delta_z - z_n)^2)^{\frac{3}{2}}} d\phi. \tag{5.19}$$

5.3 External magnetic flux

The external magnetic flux is calculated in three steps:

1. External magnetic flux of a winding in a shielding tube ring
2. External magnetic flux of the external magnet in a shielding tube ring
3. External magnetic flux of the external magnet in the shielding tube

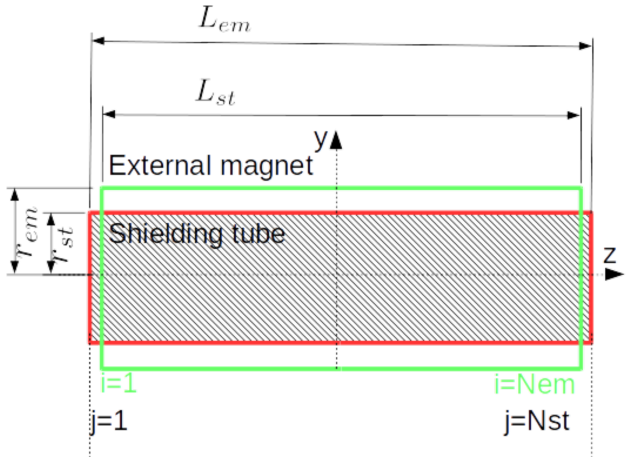

Fig. 5.7: Sketch of the geometry of the external magnet and shielding tube. The shaded area shows where the flux of the external magnet is calculated.

The external magnet is outside, but shorter than the shielding tube. In fig. 5.7 the shaded area inside the whole shielding tube indicates where the flux of the external magnet is calculated.

A formula for the external magnetic flux of one winding can be written down by integrating over $a = \pi|\vec{r}_{st}|^2$. A sketch of the underlying geometry is shown in fig. 5.8.

$$F^{wn}(\Delta_z) = \int B_z^{wn}(\rho, \Delta_z) da \tag{5.20}$$

The surface element of the shielding tube (x-y plane) is

$$da = \rho d\rho d\phi' \tag{5.21}$$

with

$$\phi' \in [0; 2\pi], \rho \in [0; r_{st}], \rho^2 = x^2 + y^2. \tag{5.22}$$

The magnetic flux density is symmetric in the azimuth ϕ'

$$B_z^{wn}(\rho, \Delta_z) = B_z^{wn}(r_x, \Delta_z). \tag{5.23}$$

Integration of B_z^{wn} over ρ and ϕ'

$$F^{wn}(\Delta_z) = \int_{\rho=0}^{\rho=r_{st}} \int_{\phi'=0}^{\phi'=2\pi} B_z^{wn}(\rho, \Delta_z) \rho d\rho d\phi'. \tag{5.24}$$

Integration over ϕ' is 2π, hence

$$F^{wn}(\Delta_z) = 2\pi \int_{\rho=0}^{\rho=r_{st}} B_z^{wn}(\rho, \Delta_z) \rho d\rho. \tag{5.25}$$

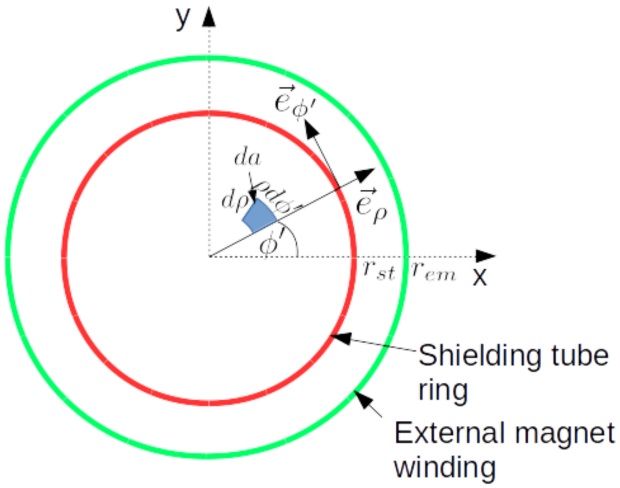

Fig. 5.8: Sketch with symbols for calculation of the magnetic flux inside the shielding tube.

By summation over all windings of the external magnet, each of them creating a magnetic flux in a ring of the shielding tube, the total flux in one ring is calculated. Considering the distance between the i^{th} winding and the j^{th} ring (fig. 5.9)

$$\Delta_z = \Delta_{ij} = |z_i^{em} - z_j^{st}|, \tag{5.26}$$

where z_i^{em}, $i = 1...N_{em}$ is the z position of a winding and z_j^{st}, $j = 1...N_{st}$ is the z position of a ring. Now the flux in every shielding tube ring can be calculated as a function of the relative distance of the windings and the rings Δ_{ij} (fig. 5.10). The external flux in the shielding tube ring j is

$$F_j^{ext} = \sum_{i=1}^{N_{em}} F^{wn}(\Delta_{ij}). \tag{5.27}$$

The external magnetic flux of the external magnet in the shielding tube is calculated in the following way. By calculating eq. 5.27 for all j and write it as a function of z_j^{st} we obtain the flux in the shielding tube as shown in fig. 5.11. I^{ext} is chosen such that the external magnetic flux density is 1 T at the center ($z = 0$, $\rho = 0$), as in the experiment, to be able to compare the results. The current is determined by a fit of the calculated field map to the measured one (sec. 6.3.2).

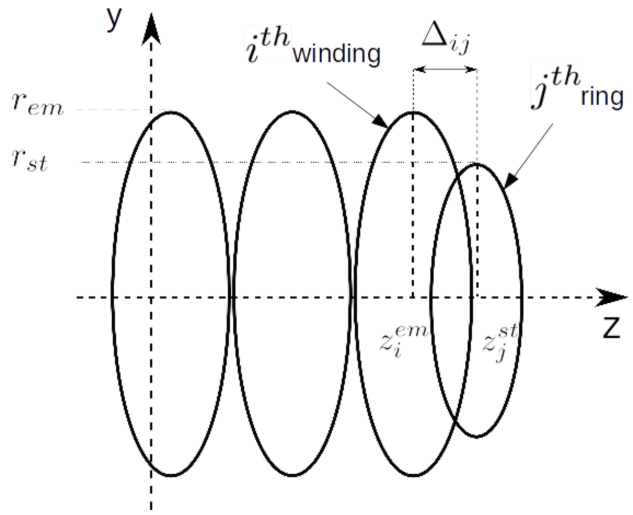

Fig. 5.9: The big circles are the windings of the external magnet. Each of them creates a magnetic flux in the shielding tube ring, showed here as a small circle.

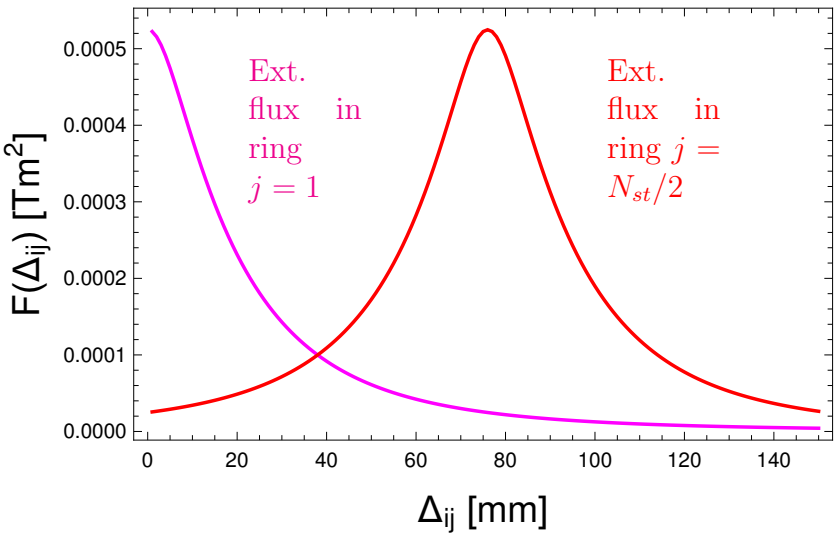

Fig. 5.10: External magnetic flux in the shielding tube ring $j = 1$ and $j = N_{st}/2$ as a function of the relative distance of the windings to the rings Δ_{ij}.

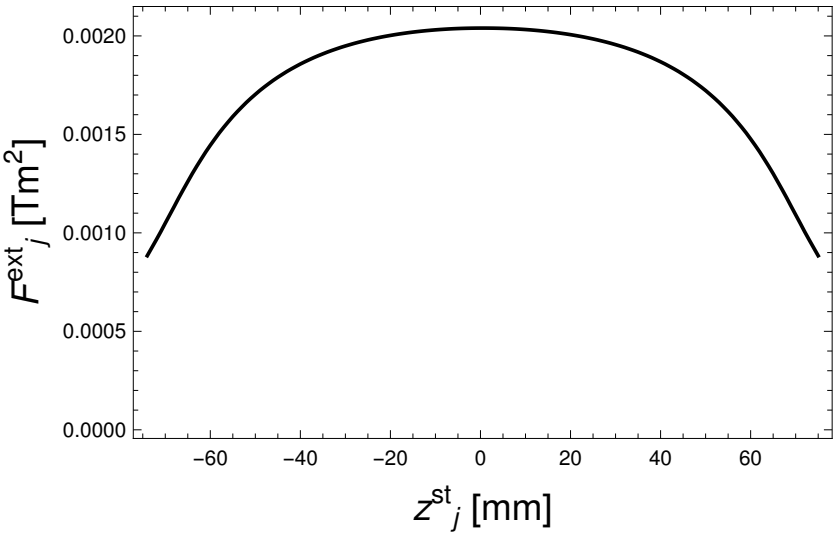

Fig. 5.11: External magnetic flux of the external magnet in the shielding tube.

5.4 Inductance of the rings

The current in the rings can be calculated by solving a linear equation, containing the flux and the inductance. This quantity depends only on the radii and distances of the rings as shown here. The derivation for a system of thin wires can be found in ref. [86]. This is extended here by considering also the width of the rings in z-direction. The flux in ring j, F_j^{ind}, arising from ring k, can be written by use of the vector potential $\vec{A_k}$ arising from the ring k

$$\vec{A_k}(x,y,z) = \frac{\mu_0}{4\pi}\int_k \frac{\vec{j_k}(\vec{r_k}(x,y,z))}{|\vec{r_k}(x,y,z) - \vec{r_j}(x,y,z)|}dxdydz, \tag{5.28}$$

where $\vec{r_k}(x,y,z)$ is a vector pointing on the k^{th} ring, that generates a vector potential in the j^{th} ring. $\vec{j_k}$ is the current density in the k^{th} ring, and $dxdydz$ the volume element. The integration goes over the volume of the k^{th} ring with radius r_{st} and width d_R. The expression can be simplified by introducing the following parametrization of a ring (fig. 5.12):

$$\begin{aligned} x(r,\phi,z) &= r\cos\phi \\ y(r,\phi,z) &= r\sin\phi \\ z(r,\phi,z) &= z \end{aligned} \tag{5.29}$$

And $dxdydz$ is $rdrd\phi dz$. By using the integration intervals

$$r = r_{st}, \phi \in [0; 2\pi], z \in [-\frac{d_R}{2}; \frac{d_R}{2}], \tag{5.30}$$

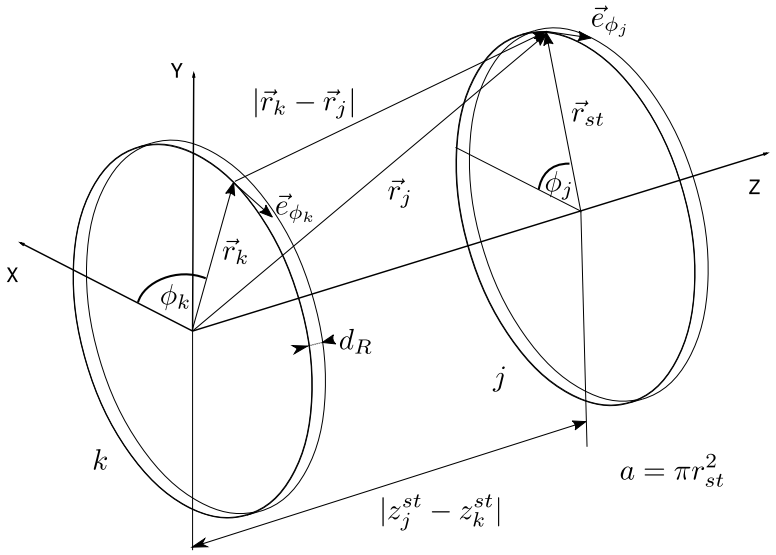

Fig. 5.12: Sketch of two rings with symbols used to calculate the inductance matrix elements.

the integration over r can be left out. The current density is integrated over a surface and has the unit $[\frac{A}{m}]$. To take into account the thickness, d, of the shielding tube, the result of the induced current will be divided by d. A current density $\vec{j}_k$ in the k^{th} ring can be defined as:

$$\vec{j}_k(\phi_k) = j_k \vec{e}_\phi(\phi_k), \tag{5.31}$$

where $\vec{e}_\phi(\phi_k) = (-\sin\phi_k, \cos\phi_k, 0)$ and $j_k = \frac{I_k^{ind}}{d_R}$ are introduced. The vector potential $A_k(\phi_j, z_j)$ at the j^{th} ring generated by the k^{th} ring is then

$$\vec{A_k}(\phi_j, z_j) = \frac{\mu_0 I_k^{ind} r_{st}}{4\pi d_R} \int_{\phi_k=0}^{\phi_k=2\pi} \int_{z'_k=z_k-\frac{d_R}{2}}^{z'_k=z_k+\frac{d_R}{2}} \frac{\vec{e}_\phi(\phi_k)}{|\vec{r}_k - \vec{r}_j|} d\phi_k dz'_k. \tag{5.32}$$

The induced magnetic flux F_j' in the j^{th} ring at position z_j (middle position in the ring) generated by the current in the k^{th} ring is

$$\begin{aligned} F_j^{'}(z_j') &= \int \vec{B}_k \cdot da \\ &= \int (\vec{\nabla} \times \vec{A}_k) \cdot da = r_{st} \int_{\phi_j=0}^{\phi_j=2\pi} \vec{A}_k \cdot \vec{e}_\phi(\phi_j) d\phi_j \\ =& r_{st} \int_{\phi_j=0}^{\phi_j=2\pi} \underbrace{\frac{\mu_0 I_k^{ind} r_{st}}{4\pi d_R} \int_{\phi_k=0}^{\phi_k=2\pi} \int_{z_k'=z_k-\frac{d_R}{2}}^{z_k'=z_k+\frac{d_R}{2}} \frac{\vec{e}_\phi(\phi_k)}{|\vec{r}_k - \vec{r}_j|} d\phi_k dz_k'}_{\vec{A}_k} \cdot \vec{e}_\phi(\phi_j) d\phi_j, \end{aligned} \tag{5.33}$$

where $\vec{B}_k$ is the magnetic flux density created by the ring k. The scalar product in the integrand $\vec{e}_\phi(\phi_j)\vec{e}_\phi(\phi_k)$ is

$$\begin{aligned} \vec{e}_\phi(\phi_j)\vec{e}_\phi(\phi_k) &= (\sin\phi_k \sin\phi_j + \cos\phi_k \cos\phi_j) \\ &= \cos(\phi_k - \phi_j). \end{aligned} \tag{5.34}$$

The distance is

$$\begin{aligned} |\vec{r}_k - \vec{r}_j| &= \sqrt{(x_k - x_j)^2 + (y_k - y_j)^2 + (z_k - z_j)^2} \\ &= \sqrt{2r_{st}^2[1 - \cos(\phi_k - \phi_j)] + (z_k - z_j)^2}. \end{aligned} \tag{5.35}$$

To take into account the width of the j^{th} ring, the following consideration can be used. The flux in a ring F_j^{ind} can be expressed as an average over the flux at a given z, $F_j^{'}(z_j)$, in the interval of the width d_R of the j^{th} ring,

$$F_j^{ind} = \frac{1}{d_R} \int_{z_j'=z_j-\frac{d_R}{2}}^{z_j'=z_j+\frac{d_R}{2}} F_j^{'}(z_j') dz_j'. \tag{5.36}$$

From eq. 5.9 it can be seen that the external flux is equal but opposite in sign to the induced flux $F_j^{ind} = -F_j^{ext}$. In eq. 5.33 it is shown that the flux is proportional to the current I_k and the proportionality constant is the inductance matrix element M_{kj}

$$-F_j^{ext} = M_{kj} I_k^{ind}. \tag{5.37}$$

The summation over k, running from 1 to N_{st}, is due to the fact that all rings contribute to the flux in the j^{th} ring. The inductance matrix element

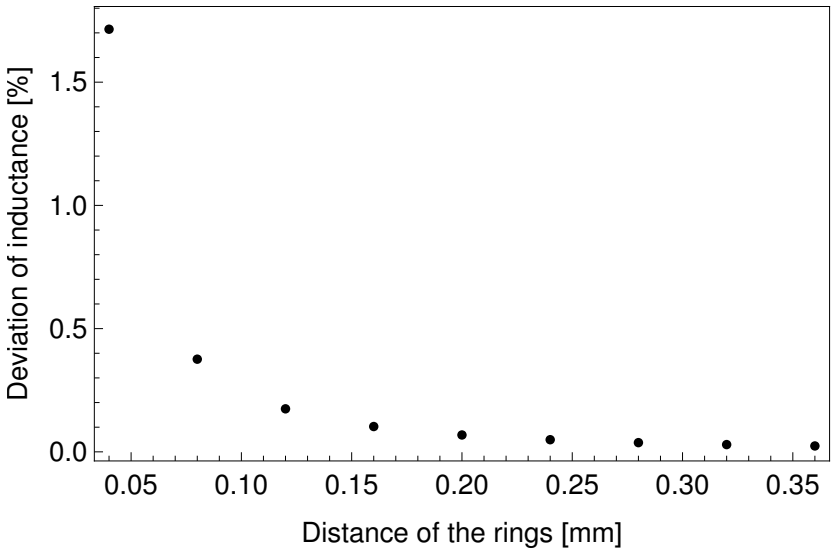

Fig. 5.13: Deviation of the inductances between the calculation with a point-like cross section and a finite extent in z-direction relative to the inductance in %. The discretization size (distance of neighboring rings) is 0.04 mm.

depends only on the geometry of the rings, in our case this are the radius r_{st} and the distance (width of a ring) d_R.

If the rings are relatively far from each other, one can neglect they finite thickness in z-direction. The current density is then $j_k = I_k^{ind}$ and the vector potential is independent of z,

$$\vec{A}_k = \frac{\mu_0 I_k^{ind} r_{st}}{4\pi} \oint_{\phi_k} \frac{\vec{e}_\phi(\phi_k)}{|\vec{r}_k - \vec{r}_j|} d\phi_k. \tag{5.38}$$

And the flux becomes

$$F_j^{ind} = \frac{\mu_0 I_k^{ind} r_{st}^2}{4\pi} \oint_{\phi_k} \oint_{\phi_j} \frac{\vec{e}_\phi(\phi_k) \cdot \vec{e}_\phi(\phi_j)}{|\vec{r_k} - \vec{r_j}|} d\phi_j d\phi_k. \tag{5.39}$$

The deviation of the inductances between the calculation with a point-like cross section and a finite extent of the rings in z-direction relative to the inductance is shown in the plot in fig. 5.13. From the ninth neighbor, the cross section is approximated as point-like. The result of the calculation, with a point-like cross section for all rings is significantly different from the measured value of the residual field of a shielding tube. This can be seen in appendix B.

For the diagonal elements of the inductance matrix, when $k = j$ and $|z_k^{st} - z_j^{st}| = 0$ eq. 5.33 cannot be integrated because of the term

$$1 - \cos(\phi_k - \phi_j) + (z_k - z_j)^2 = 0 \tag{5.40}$$

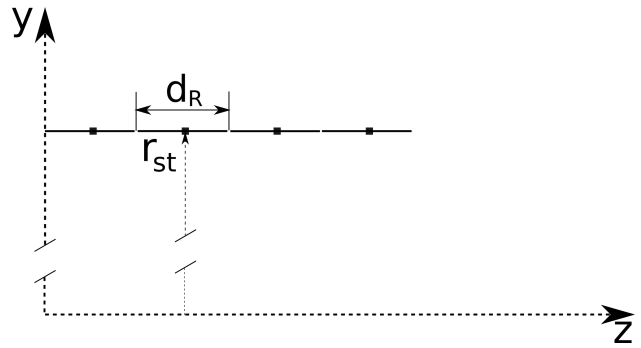

Fig. 5.14: Cross section of a ring with the thickness d_R (equal to the distance of neighboring rings). The self inductance of a ring can be approximated by a formula for the self inductance of a thin tape-like one dimensional cross section.

for $\phi_k = \phi_j$. To overcome this an approximation to the exact solution can be used. The cross section considered here is like a thin tape as shown in fig. 5.14. We assume that the current is distributed homogeneously on the cross-sectional area (thickness of the ring). The tabulated formula to calculate the self inductance is [87]:

$$M_{k=j} = \mu_0 r_{st} \left[\ln \frac{8r_{st}}{d_R} - \frac{1}{2} + \frac{d_R^2}{32 r_{st}^2} \left(\ln \frac{8r_{st}}{d_R} + \frac{1}{4} \right) \right] \tag{5.41}$$

5.5 Induced magnetic flux density

The solution of $M_{kj} I_j^{ind} = -F_j^{ext}$ is the induced current I_j^{ind}. The magnetic flux density can be calculated from it (under the assumption that the rings have a point-like cross section) via Biot-Savart (eq. 5.16)

$$I_j^{ind} \longrightarrow B_{j,r_x=0}^{ind} \longrightarrow B_{j,r_x=0}^{res} = B_{j,r_x=0}^{ext} + B_{j,r_x=0}^{ind}. \tag{5.42}$$

The radius is $R = r_{st}$, and the distance between rings $\Delta_z = \Delta_{kj} = |z_k^{st} - z_j^{st}|$. The z-component of the induced magnetic flux density created by the current $I_j^{ind} = I^{ind}(z = z(j))$ of the j^{th} ring is

$$\begin{aligned} B_z^{ring}(r_x = 0, \Delta_z) &= \frac{I_j^{ind} \mu_0}{4\pi} \int_0^{2\pi} \frac{R^2}{(R^2 + \Delta_z^2)^{\frac{3}{2}}} d\phi \\ &= \frac{I_j^{ind} \mu_0}{2} \frac{R^2}{(R^2 + \Delta_z^2)^{\frac{3}{2}}}. \end{aligned} \tag{5.43}$$

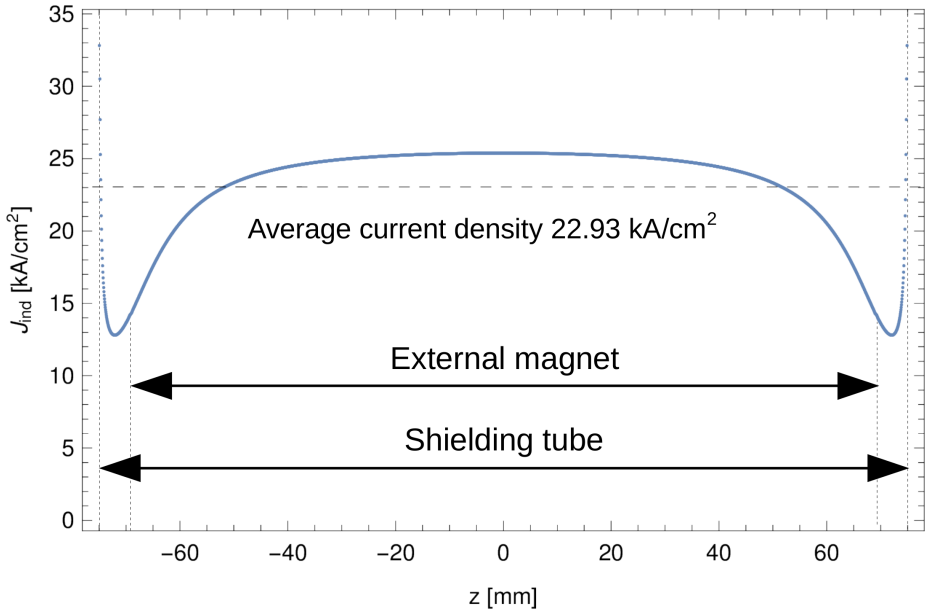

Fig. 5.15: Induced current density along the axis of the shielding tube. The average induced current density is also shown. It is consistent with the experimentally estimated value in sec. 6.3.3 $J_{ind}^{EXP} = (23000 \pm 2000)\frac{A}{cm^2}$. *The size of the shielding tube and the external magnet is also shown. The dashed line indicates the average current density.*

We obtain the induced magnetic flux density along the axis of the shielding tube by summation over all rings

$$B_{r_x=0}^{ind} = \sum_{i=1}^{N_{st}} B_z^{ring}(\Delta_{kj}). \tag{5.44}$$

5.6 Results of the calculation

The magnetic flux in the shielding tube of the external magnet, when the magnetic flux density in the center is 1 T, is calculated and used as an input to the the matrix equation 5.37. This equation can be solved for the induced current in the shielding tube. This is shown in fig. 5.15. The current density is determined from the current by taking the finite wall thickness of the shielding tube into account. The residual magnetic flux density is the

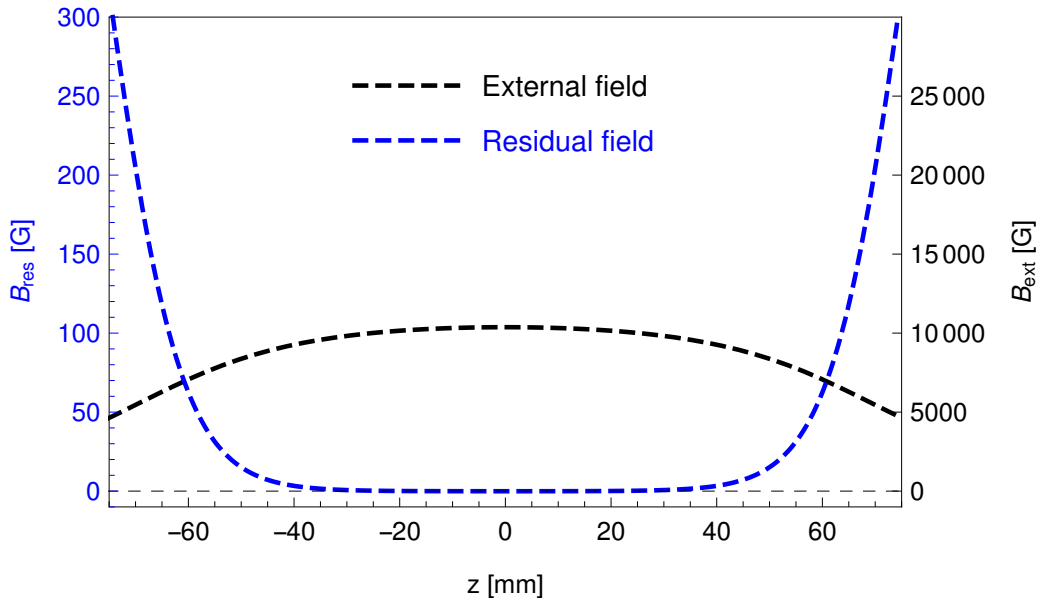

Fig. 5.16: Result of the simulation. The z-component of the residual field and the applied external field on the axis of the shielding tube.

superposition of the external and induced magnetic flux densities

$$B^{res} = B^{ext} + B^{ind}. \tag{5.45}$$

This is the final result of my simulation. In fig. 5.16 the residual field on the axis of the shielding tube and the applied external field are shown.

5.7 Residual flux density in the limit of zero ring width

The expectation is that the residual flux density goes to zero, when the discretization size d_R (equal to the width of a ring and also the distance of neighboring rings) is approaching the continuum limit with $d_R = 0$. We calculate the residual magnetic flux density at different discretization sizes d_R. The plot is shown in fig. 5.17. A fitting function to the ratio of the residual flux density and the external flux density B_{res}/B_{ext} vs. d_R is constructed. The difference of the data and the fitting function should be negligible compared to the expected measurement errors. The fitting function is then extrapolated to estimate the value at $d_R = 0$. The expectation of zero residual flux

density at $d_R = 0$ is fulfilled by the calculation to the accuracy at the order of 10^{-7}.

5.8 Varying the length of the shielding tube and the external magnet

In this section the behavior of the induced current at the edges of the shielding tube is investigated, by variation of the length of the tube and the external magnet. Also the numerical stability of the calculation is tested at the same time, since the discretization changes, by changing the length of the tube and thus the number of rings.

The resulting current and residual field under variation of the length of the shielding tube in the range $L_{st} = 150\text{to}450$ mm was investigated. The current density in the shielding tube is shown in fig. 5.18 and the residual field in fig. 5.19. The length of the external magnet is fixed to $L_{em} = 138$ mm. The discretization size in this simulation part is $d_R = 0.1$ mm. The reason for this coarse value is to spare computational resources for long tubes and consequently large amount of rings at small discretization size. As the shielding tube gets longer the current at the edges of the tube decreases until a saturation at 225 mm. This is expected since the length of the external magnet and therefore the external magnetic field does not increase, whereas at the same time, the shielding tube has more surface. The interval, where the residual field is minimal, increases as expected. Above a tube length of 225 mm, a saturation of the shielded length can be observed.

The current and the residual field at different lengths of the external magnet in the range of $L_{em} = 138\text{to}3000$ mm was investigated. The current density in the shielding tube is shown in fig. 5.20 and the residual field in fig. 5.21. The length of the shielding tube is fixed at $L_{st} = 150$ mm. The discretization size is $d_R = 0.04$ mm. As the length of the external magnet increases the inhomogeneity of the external field decreases, in a way that the field at the ends of the shielding tube increases. As a consequence the current density and the residual field also increases as expected.

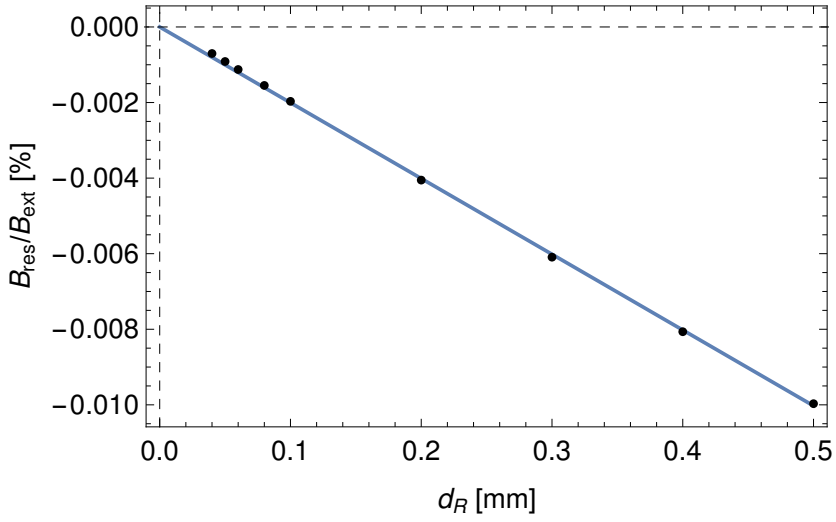

(a)

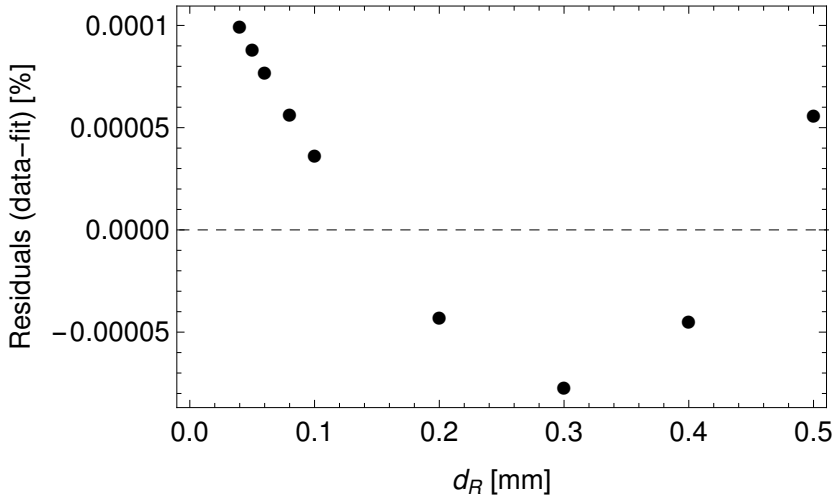

(b)

Fig. 5.17: a) Ratio of the residual flux density and the external flux density B_{res}/B_{ext} vs. d_R. The estimated values for the parameters of the linear regression function $f(x) = a_{fit} + b_{fit} \cdot x$ that reduce the residuals to less than $10^{-4}\%$ are $b_{fit} = -0.0201 \pm 1 \cdot 10^{-4}$ and $a_{fit} = 0 \pm 3 \cdot 10^{-5}$. Extrapolation of the fitting function, where $x = d_R$, to the continuum limit with $d_R = 0$. b) Residuals of the fits.

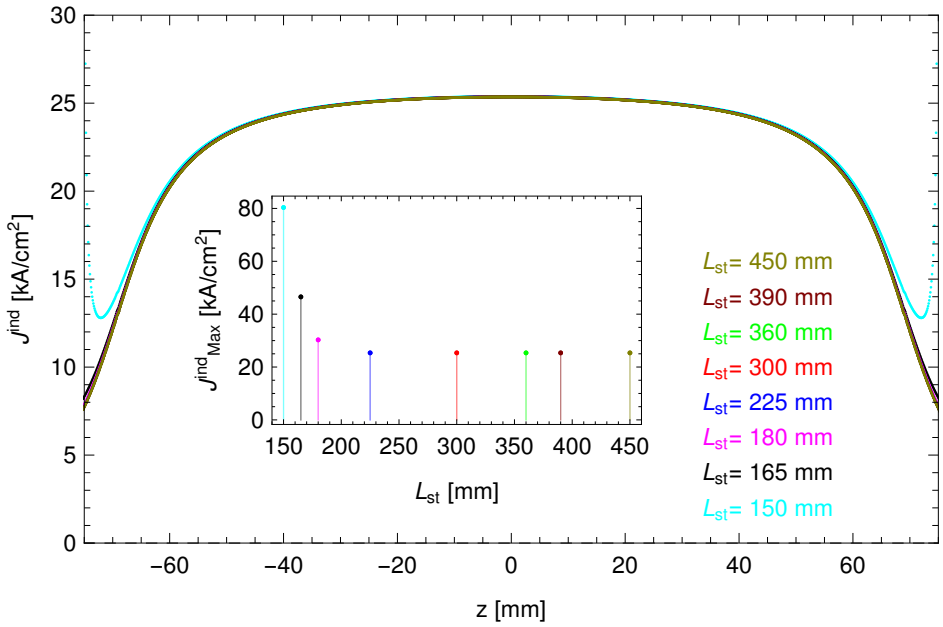

Fig. 5.18: Current density by variation of the length of the shielding tube. The inset plot shows the maximum current in the shielding tube.

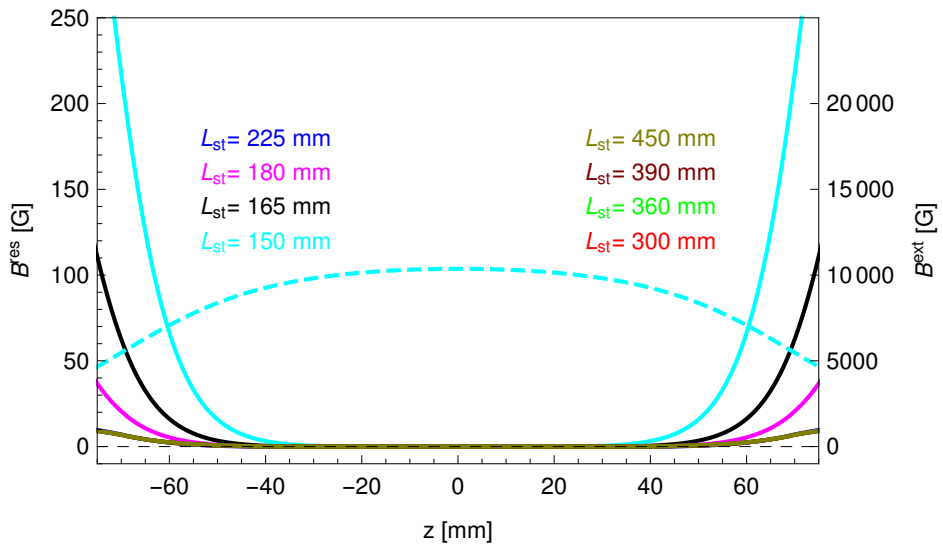

Fig. 5.19: Variation of the length of the shielding tube. Scale on the right for the external field (dashed line). The external field was the same for all simulations. The tube lengths and the corresponding colors are given in the legend of the plot. The residual field decreases on the axes of the shielding tube in the plotted region, when the shielding tube gets longer. From the tube length of 225 mm and higher, the residual field does not change much, so the corresponding curves overlap.

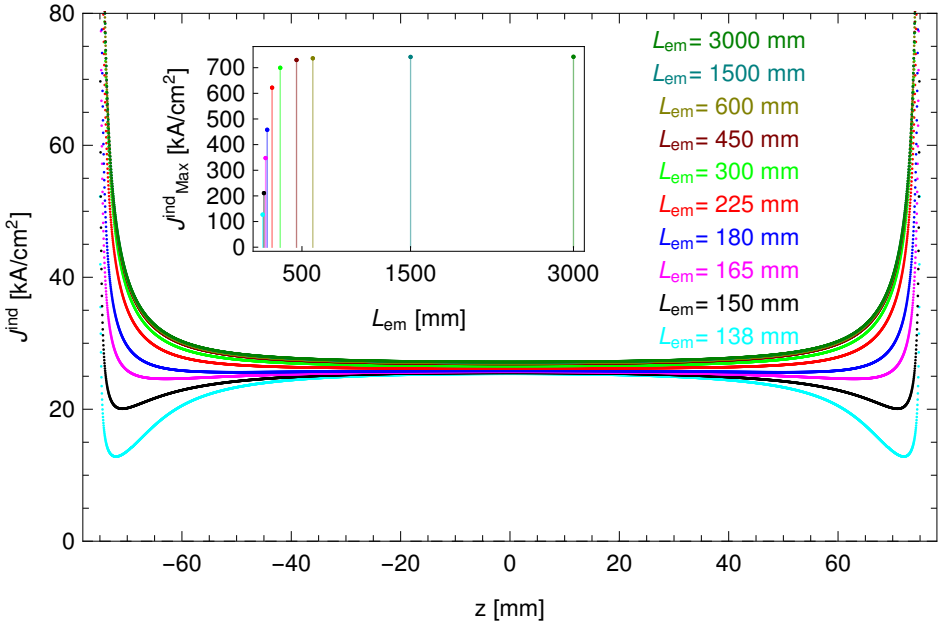

Fig. 5.20: Current density by variation of the length of the external magnet. The inset plot shows the maximum current in the shielding tube.

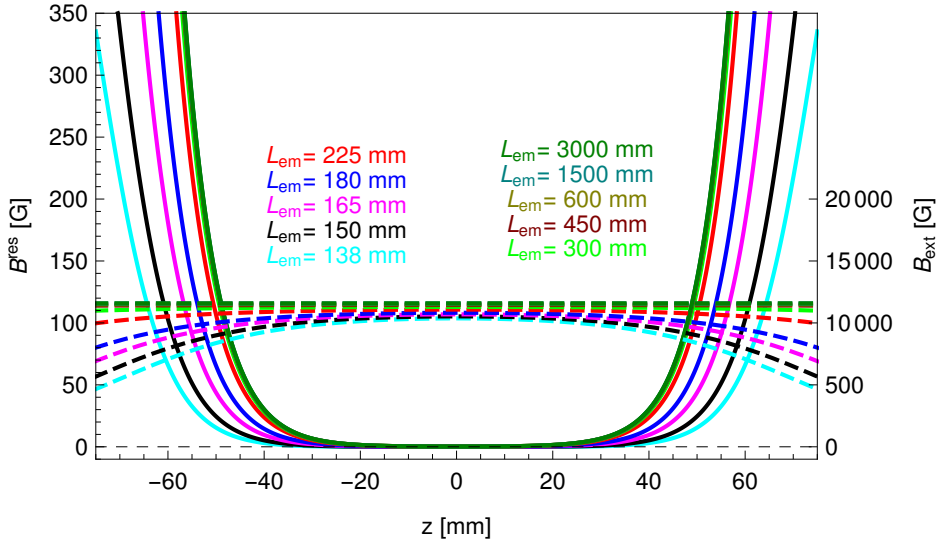

Fig. 5.21: Residual field by variation of the length of the external magnet. Scale on the right for the external field (dashed lines).

Chapter 6

Experimental test of the shielding tube

As described in the earlier chapters the main objective of this work is to shield the magnetic flux at the target region created by the $\bar{\text{P}}$ANDA solenoid. The shielding is constrained by the following requirements. It should:

- Reduce the magnetic flux density as much as possible
- Shield a volume large enough for installation of a polarized target (homogeneity in space)
- Allow for a long data taking time by stability of the residual field (stability in time)
- Minimize the radiation loss in the material by making it as thin as possible

In this chapter an experimental approach will be discussed that tries to answer the question whether the above requirements can be fulfilled by using a BSCCO shielding tube, a high-temperature superconductor. The basic principle is to apply a longitudinal magnetic field parallel to the wall of the shielding tube and measure the residual field. The measurement of the external field is essential to determine the shielding factor. The superconducting magnet and the shielding tube cannot be cooled and operated separately with the cryogenic equipment available. In the first part of this experiment the external magnet is measured alone without the shielding tube. In the second part, also the shielding tube is installed. Because of the Lorentz force on the tube, for safety reasons, the maximally applied magnetic field is 1.4 T. The longitudinal component of the residual field is measured with a Hall probe on the axis of the tube with a manually driven moving system. Also a stability

measurement is done by applying a constant external field over several days. The measurements are carried out in a liquid helium environment. The experimental setup, the measurement method, the analysis of the data and the results will be presented. At the end, the results will be summarized.

6.1 Experimental setup for testing the shielding tube

The experimental setup consists of the following elements (fig. 6.1): The liquid helium that is used, to cool down the tube system (shielding tube and external magnet) to 4.2 K is hold in a dewar. Underneath the dewar there is a scale (weighing machine). The level of liquid helium needed for full coverage of the tube system was calculated. By controlling the weight and knowing the density of helium 0.1786 g/L the volume is calculated and converted to the level of the liquid in the dewar. The shielding tube was covered entirely during the experiments. The insert in fig. 6.1 is a construction for holding the tube system, consisting of the external magnet, the shielding tube and the Hall probe together with the Zero-field magnet on top, in the liquid helium and guiding the wire leads from the tube system out of the dewar. All components are made of non-ferromagnetic materials, that would distort the magnetic field measurements. A picture of the tube system is shown in fig. 6.2 and the drawing is given in fig. 6.3. The shielding tube is surrounded by a superconducting magnet applying an external field to the shielding tube. With a Hall probe inside the shielding tube the residual magnetic field can be measured. Since the residual field is expected to be very close to zero, one has to ensure the functionality of the Hall probe also in the case, when it does not show a nonzero magnetic flux density. To be always able to to check the response of the Hall probe, an additional coil is mounted directly on the top of it.

6.1.1 The external magnet and copper tube

Since the shielding of 1 T to 2 T will be demonstrated, a special superconducting magnet (external magnet) is constructed that can apply at least 2 T to the shielding tube. The size of this magnet is relatively small (length 138 mm, inner diameter 63 mm), compared to solenoid of the $\bar{\text{P}}$ANDA spectrometer (length 2.7 m, inner diameter 1.9 m). This difference leads to a larger inhomogeneity of the external magnet in the experiment. The required Ampere-turns can be approximated with a calculation for a solenoid

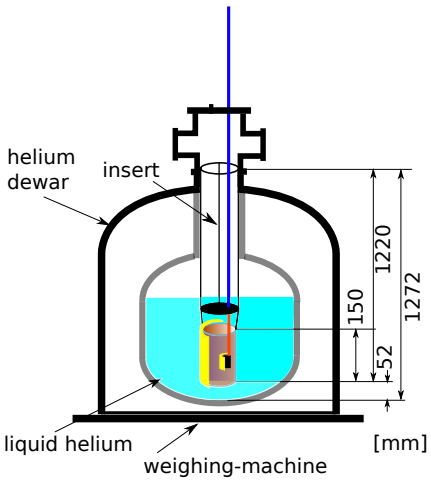

(a) Experimental setup. Dewar filled with liquid helium to keep the external magnet and the shielding tube at a temperature of 4.2 K. The insert is shown seperately in b). By measuring the weight of the dewar with the weighing machine before and after filling with helium, the volume of helium in the dewar is determined.

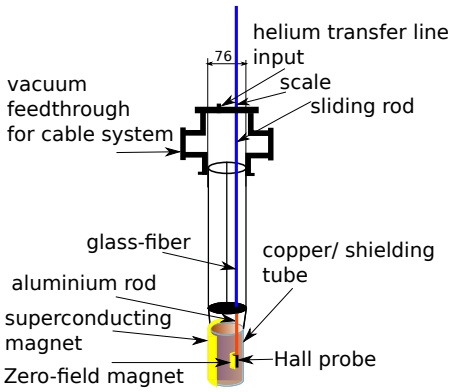

(b) The insert with the shielding tube. It is holding the external magnet (superconducting magnet) and the shielding tube. The Hall probe and the Zero-field magnet are mounted on the end of a sliding rod (glass fiber rod in the upper section of the insert is connected to an aluminum rod in the lower section). It allows for measurement of the magnetic field along the axis of the shielding tube by manual alignment. The rod is equipped with a scale in mm that can be read back to determine the position of the Hall probe. The head on the top of the dewar has bores which are used to lead the cable system out from inside. Also a helium transfer line, used to fill the dewar, can be attached.

Fig. 6.1

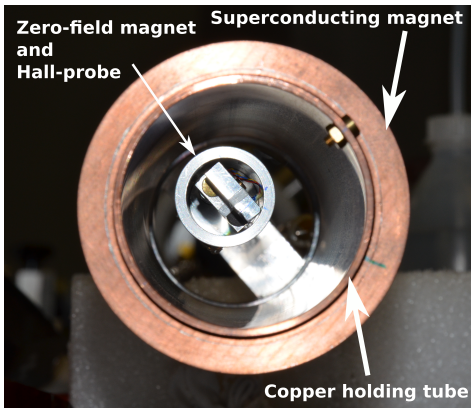

(a) External (superconducting) magnet with the copper holding tube.

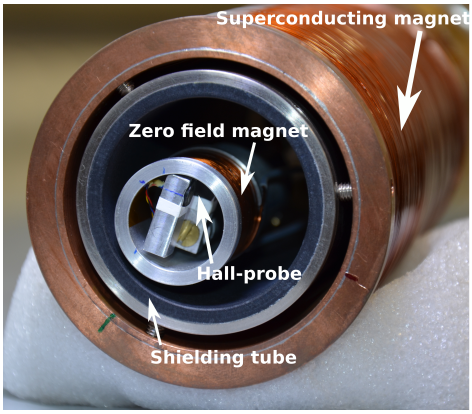

(b) External (superconducting) magnet with the shielding tube.

Fig. 6.2: Tube system in the first (a) and second (b) part of the experiment. In the first part the magnetic field created by the external magnet is measured. In the second part the shielding tube is inside the external magnet and the residual field is measured. The Hall probe is inside the shielding tube on a stick that is moved to its position on the axis of the tube.

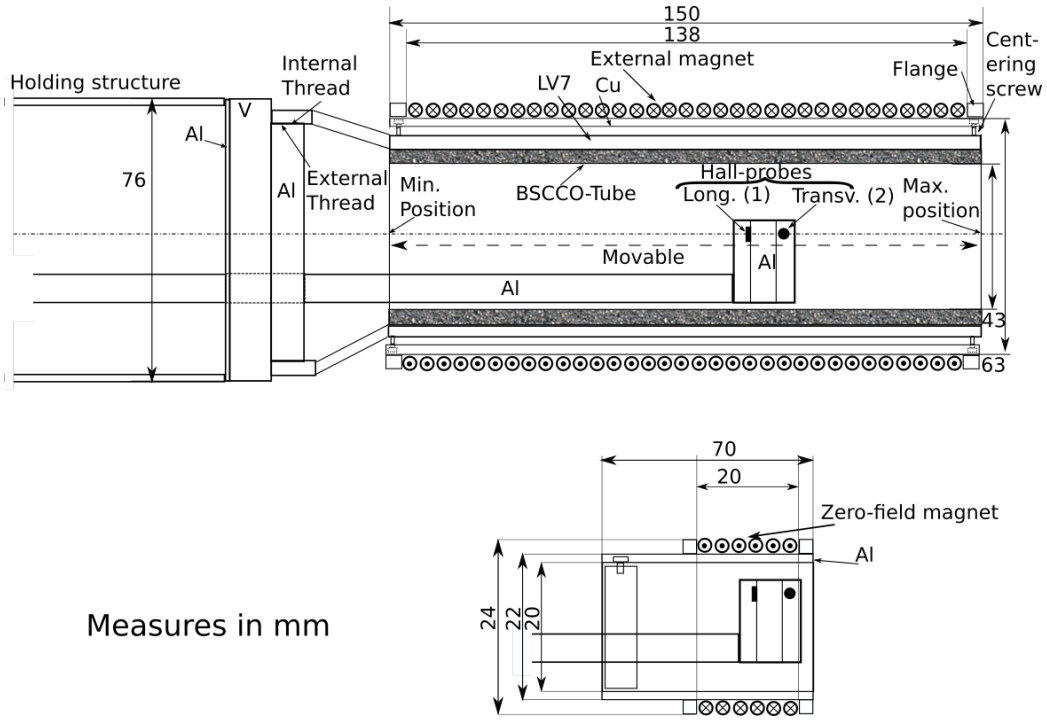

Fig. 6.3: Drawing of the holding structure installation and tube system with shielding tube and external magnet on top. The Zero-field magnet is shown separately.

Calculation parameter	
Wire diameter	0.291 mm
Winding per layer	474
Number of layers	22
Calculated field at center at 1 A	848.5 G

Tab. 6.1: Parameter list used for the calculation of the field map of the external magnet.

Superconducting magnet	
Inner diameter	63 mm
Outer diameter	ca. 68 mm
Length	138 mm
Winding per layer	474
Number of layers	22
Measured field at center at 1 A	(833.6 ± 1.6) G
Quench (measured)	(24150 ± 90) G

Tab. 6.2: External magnet specifications

with a large length over diameter ratio:

$$nI = \frac{Bl}{\mu_0} = \frac{2\ \mathrm{T} \cdot 0.15\ \mathrm{m}}{4\pi \cdot 10^{-7} \frac{\mathrm{Vs}}{\mathrm{Am}}} = 238732\mathrm{A}$$

with the magnetic flux density B, the length of the magnet l, the number of windings n and current I. The required current density can only be achieved by a superconductor. The resulting field map of a calculation with Biot-Savart (sec. 5.2) is shown in fig. 6.4. The calculation of the field map is based on the parameter list in tab. 6.1. They are chosen in a way that the required magnetic field of 2 T can be achieved. A picture how the external magnet is mounted onto the top of the shielding tube is shown in fig. 6.5. The specification of the magnet is given in tab. 6.2. For the wire a multi-filamentary Niobium-Titanium (NbTi) was selected. It has a transition temperature around 9 K. The copper holding structure that holds the solenoid, is fixed with three centering screws on the ends of the shielding tube. For the operation of the external magnet a bipolar high current supply with specifications shown in tab. 6.3 is used. The copper current leads inside the dewar should be designed to carry at least 40 A and with an insulation that is appropriate to work with liquid helium.

As a replacement for the shielding tube in the first part of the measurement, when the field of the external magnet will be measured, a copper tube

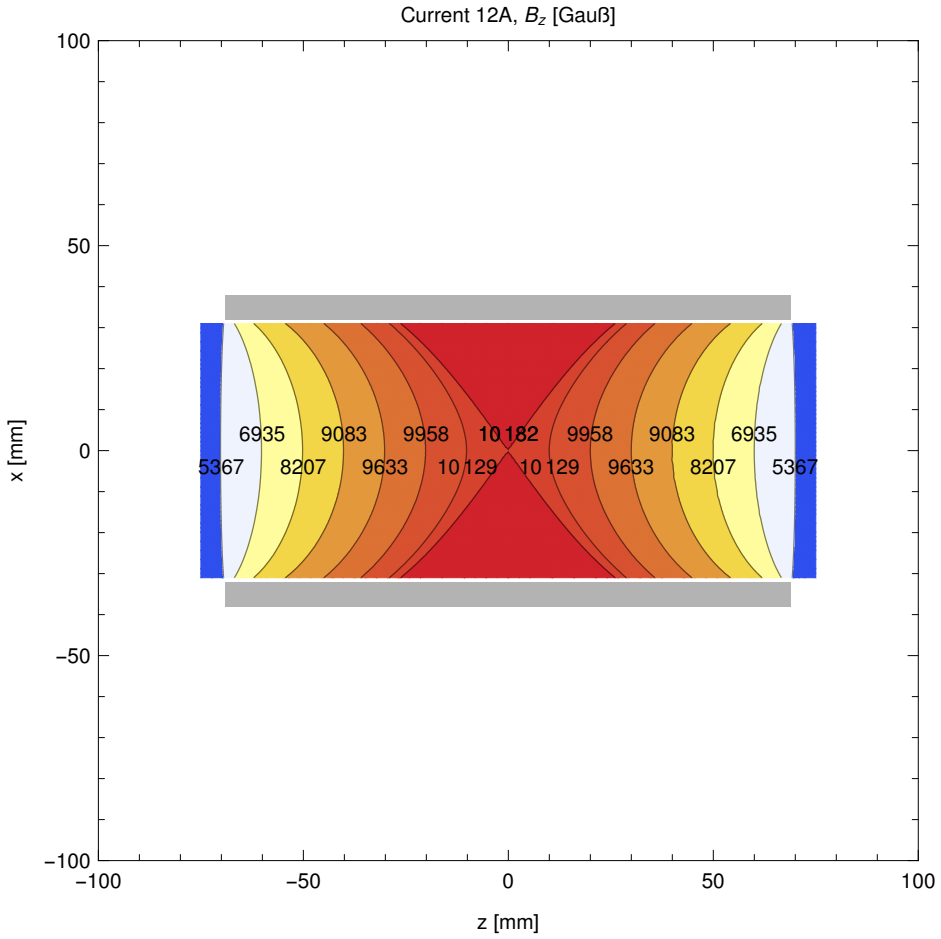

Fig. 6.4: Calculation of the magnetic field map $f_{map}(x, z)$ of the external magnet at a current of $I^{ext} = 12$ A. The contour lines of the longitudinal component z of the magnetic flux density and the values in G on the lines are shown. The colors refer to the strength of the magnetic field. The gray regions are the windings of the solenoid.

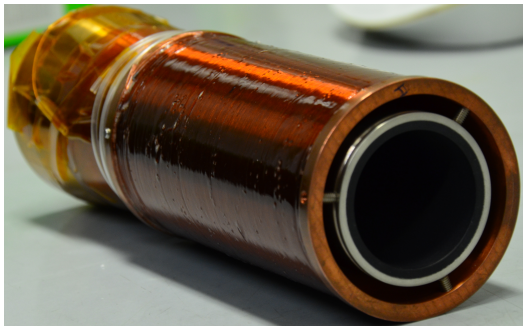

Fig. 6.5: The shielding tube and the external magnet mounted on the top.

	I	U
Range	±75 A	±10 V
Accuracy	0.1 %	0.5 %
Ripple and noise	max. 2 %	

Tab. 6.3: Specifications of the high current power supply (Kepco BOP 1000W) used for operation of the external superconducting magnet. For currents lower than 2.48 A the measured uncertainty is 2.5 mA

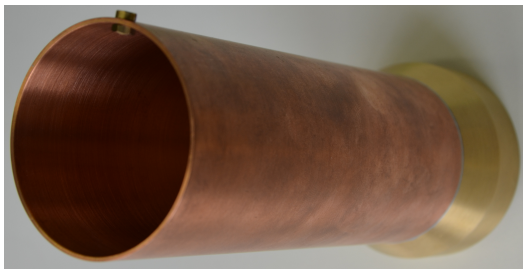

Fig. 6.6: Copper tube (Inner/ Outer diameter 60 mm/ 63 mm) used as a replacement for the shielding tube in the first part of the experiment

is used (fig. 6.6). inside the external magnet. Copper is not ferromagnetic (magnetic susceptibility $\chi_m = -9.6 \cdot 10^{-6}$) and does not have an effect on the magnetic field measurements. The variation of the magnetic field in time is very low compared to the inductance of the copper tube, also all measurements are done in a static magnetic field. Thus the inductance can be neglected.

6.1.2 The BSCCO shielding tube

The shielding tube used in the second part of this experiment (fig. 6.7) is a melt cast BSCCO hollow cylinder purchased from Nexans[1]. The technical drawing with all dimensions is given in fig. 6.8. Its shielding performance at the temperature of 10 K was reported in ref. [88] and is summarized in tab. 6.4. At this temperature the BSCCO shielding tube is able to shield a magnetic field of 1 T with a residual field of 1 mT (shielding factor 10^3). A better performance at 4.2 K is expected, since the critical current density in a high-temperature superconductor increases with decreasing temperature. The shielding tube has the dimensions outer diameter 50 mm, inner diameter 43 mm and length 150 mm. The uncertainty in the wall thickness is 0.2 mm. (sec. 6.3.3). It is hold by a steel tube. Its dimensions are described in tab. 6.5.

[1]Nexans SuperConductors GmbH Hürth

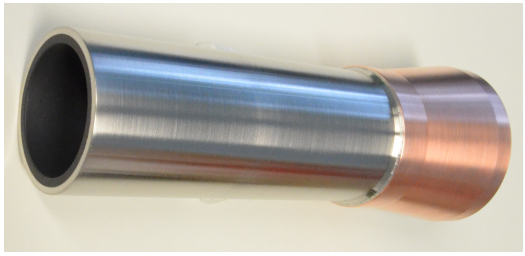

Fig. 6.7: BSCCO-2212 shielding tube. The length is 150 mm and the wall thickness 3.5 mm. It is hold by a CuNiMn (LV7) tube with a wall thickness of 2 mm from Nexans soldered to a copper thread with that the connection to the insert can be established.

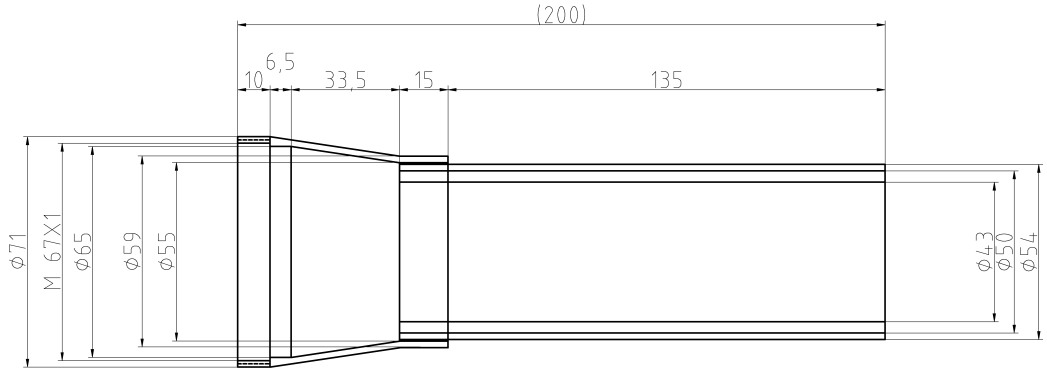

Fig. 6.8: Technical drawing of the BSCCO shielding tube with the holding structure and thread for installation on the insert.

BSCCO-2212 Characteristics	
Critical temperature	92 K
Current density at 10 K	16 kA/cm^2
Shielding factor at 10 K; 1 T	1000
Radiation length of BSCCO	1.5 cm
Density of BSCCO	6.3 g/cm^3

Tab. 6.4: Measurement results of a BSCCO shielding tube that can be found in ref. [88]

BSCCO-2212 Shielding tube	
Inner diameter	43 mm ±0.3
Outer diameter	50 mm ±0.3
Length	150 mm
Inner diameter of CuNiMn (LV7) tube	50 mm ±0.1
Outer diameter of CuNiMn (LV7) tube	54 mm ±0.1
Radiation length of CuNiMn	1.6 cm
Density of CuNiMn	8.25 g/cm^3

Tab. 6.5: Dimensions of the shielding tube

6.1.3 The YBCO tube

A tube with the same length, an inner diameter of 50 mm and an outer diameter 60 mm consisting of the high temperature superconductor Yttrium-1 Barium-2 Copper-3 Oxid (YBCO) was tested in a cryostat in Bonn[2] at the temperature of 1.5 K. This test was carried out twice. In the first experiment a good shielding effect was recorded, but the Hall probe was realized to be broken after the experiment. Therefore a shielding effect could not be shown for sure. For the second test with a new Hall probe a 4 mm bore was drilled in the wall of the tube. Since there was no shielding effect it was unclear, whether the broken Hall probe was the reason, that the two experiments were not consistent with each other, or the drilling of the bore caused the YBCO tube to be useless for shielding in the second test.

For this reason the experiment was repeated with the experimental setup described here with a new YBCO tube, that was manufactured in the same way, with the same length and a wall thickness of 3 mm. A shielding effect could not be observed.

6.1.4 The Hall probe and the Zero-field magnet

A Hall probe is a sensor made of a semiconductor that is operated by driving a control current I_c through the sensor. If a magnetic field B perpendicular to the current direction is present, the electrons will be bended by the Lorentz force perpendicular to the current and the magnetic field in a way that a static charge is built up, by separation of electrons and holes, and an electric field results that equals the Lorentz force. A voltage U_H appears on the sides

[2]Polarized Target Group at the Physikalisches Institut der Universität Bonn

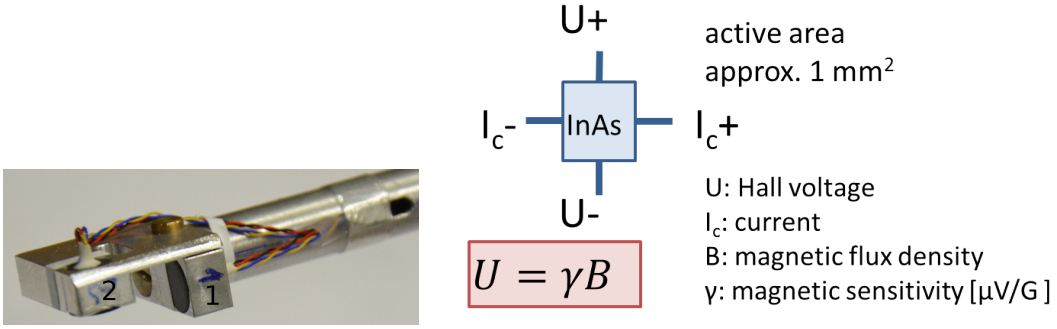

Fig. 6.9: Left: The two Hall probes used for the measurement in liquid helium. They are built into the Hall probe holder on the sliding rod. In all measurements the Hall probe 1. is used. The numbering of the Hall probes is as in the picture. Right: Principle sketch of the HGCA 3020 Indium Arsenide cryogenic Hall probe sensor chip with the configuration of the leads.

	T= 298 K	T =4 K
Magnetic sensitivity γ [mV/kG]	0.827	0.821 ($\pm$0.01%/K)
Zero field offset	3.1 μV ($\pm$ 0.4 μV/K)	

Tab. 6.6: Specifications of the Hall probe Lake Shore HGCA 3020.

of the sensor and is proportional to B as follows $U_H = \gamma B$. In fig. 6.9 the two Hall probes built into the Hall probe holder are shown. Both are fabricated by Lake Shore (HGCA 3020). We used the Hall probe number 1 sensitive to the longitudinal component of the field of the external magnet. It has the specification shown in tab. 6.6. The Hall probe was calibrated by Lake Shore and corrections to the linearity are given in appendix C. The given accuracy of better than 0.1 % up to 2 T magnetic field is guaranteed after applying the corrections and by using a nominal control current I_c = 100 mA with a stability better than 10^{-4}. The temperature range is 1.5 K to 375 K. For the control current and readout of the Hall voltage the devices specified in tab. 6.7 and tab. 6.8 are used. The Hall-probe holder is fixed on a sliding rod that can be moved along the axis of the shielding tube. On a scale on the top of the dewar the position of the Hall probe is read back.

The Zero-field magnet is shown in fig. 6.10. It is a small normal conducting solenoid on the top of the Hall-probe with specifications tabulated in tab. 6.9. As a current supply for the Zero-field magnet the device Instek PSP 603 with the specifications in tab. 6.10 is used. The maximum field

	Current supply Digistant 6425 T
Range	200 mA
Resolution	1 µA
Error	$(0.005\%rdg + 5 \cdot 10^{-10})$ A
Noise	$(0.0002\%rdg + 1 \cdot 10^{-11})$ A

Tab. 6.7: Specifications of the control device to operate the Hall probe. The abbreviation rdg stands for the read back value on the display of the instrument. rng stands for the chosen range.

	Voltmeter Prema 5017
Range	0.1 µV to 300 mV (0.1 G to 365.4 kG)
Resolution	10 nV (0.0122 G)
Error	$(0.0008\%rdg + 0.0002\%rng)$ (24 h)
Accuracy for low field	(0.821 ± 0.6) µV $((1 \pm 0.73)$ G)
Accuracy for high field	(8210 ± 6.6) µV $((10,000 \pm 8)$ G)

Tab. 6.8: Specifications of the read out device of the Hall probe. The abbreviation rdg stands for the read back value on the display of the instrument. rng stands for the chosen range.

Wire diameter	0.75 mm
Winding per layer	27
Number of layers	2
Field at center at 1 A	21.9 G
Inner diameter	22 mm
Length	20 mm

Tab. 6.9: Parameter list of the Zero-field magnet.

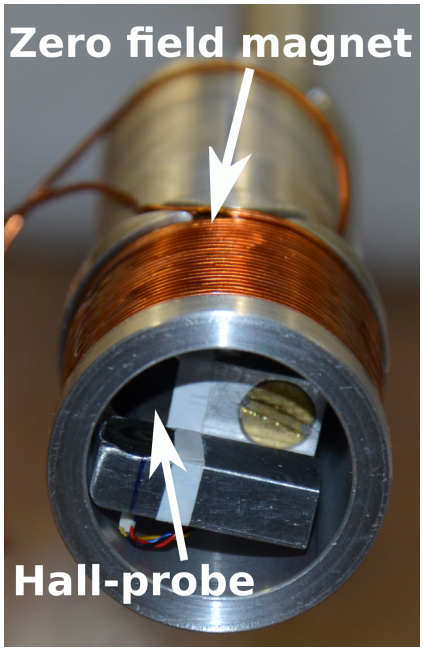

Fig. 6.10: The Zero-field magnet is a normal conducting coil on an aluminum holder directly on the top of the Hall probe to ensure the Hall probe functionality when the external field is shielded.

Range	3.5 A
Resolution	2 mA
Accuracy	(0.1 % rdg +5 digits)
Ripple	max. 10 mA

Tab. 6.10: Current supply for operation of the Zero-field magnet (Instek PSP 603). The abbreviation rdg stands for the read back value on the display of the instrument.

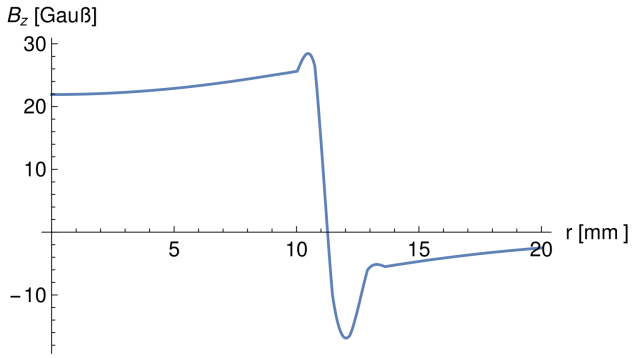

Fig. 6.11: Calculation with Biot-Savart of the magnetic field strength of the Zero-field magnet. The z-component of the magnetic flux density B_z vs. the radial distance from the center of the Zero-field magnet is shown. It decreases fast outside of the magnets surface (at ca. $r = 11$ mm).

of about $21 \cdot 10^{-3}$ T will not affect the shielding tube. Since only a variation of the flux induces a shielding current, the magnetic field lines that do not exit the inner part of the shielding tube and thus not varying the flux, will not induce any current. A part of the magnetic field lines do exit, but they are very weak, since the magnetic field strength outside of a solenoid decreases relatively fast (fig. 6.11). Therefore, the induced shielding current due to the Zero-field magnet can be neglected.

6.1.5 The data acquisition system

In order to control the power supplies for the magnets, read out the Hall voltage, the pressure and acquire and save the measured data, a data acquisition system is needed. Fig. 6.12 gives an overview of what was used for this measurement. The magnets, the Hall sensor and the pressure sensor are installed in the dewar. The magnets are connected to power supplies, the Hall sensor to a current supply and a voltage readout device. The are located directly next to the dewar. The pressure sensor is located at the inner part of the dewar at the top. It converts the pressure to a voltage. It is connected to a voltage read out device outside the dewar. All readout and control devices are connected via a RS-232 interface to a computer running the EPICS software, for controlling the input and output of the data. A read-out cycle once every 2 seconds is sufficient. The data from all devices are synchronized with a time delay, less then a second, and written together in the same output stream. The total number of readout parameters is 6. The Zero-field magnet current supply is controlled automatically with a special software. The driving of the current supply for the external magnet is

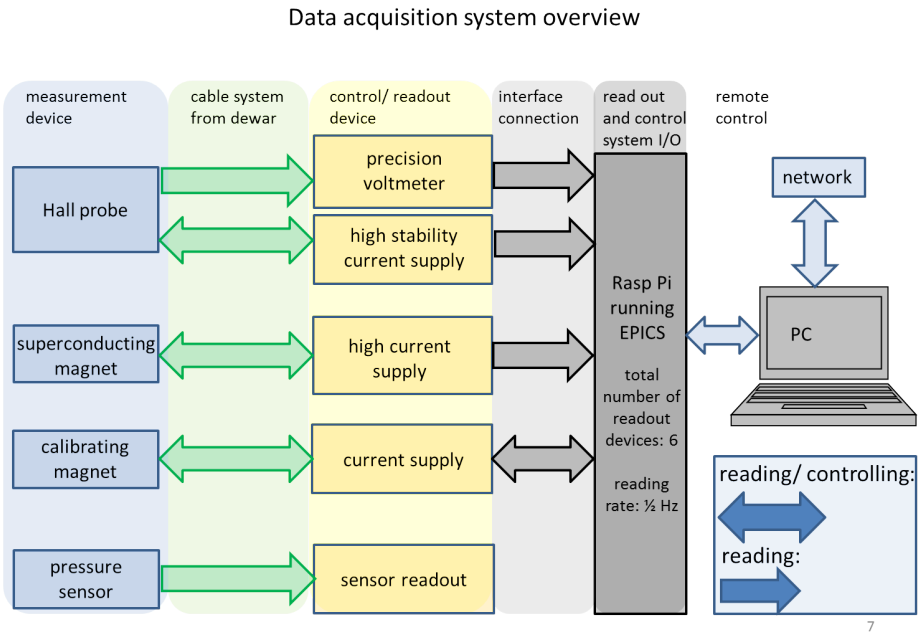

Fig. 6.12: Design of the data acquisition system. The sensors, the devices and they connection to a computer that is taking the data in digitized form and writing it to a single data stream, is shown.

done manually. The computer is connected to the network. All access of the data and controlling can be done remotely through a terminal. A log-book software is recording all data taking runs started by the operator.

6.2 Experimental procedure of the measurements

This experiment is divided into two main parts. In the first part the magnetic field at the center of the external magnet is measured by increasing the current in it. The shielding tube is not installed. Also the magnetic field along the axis of the external magnet at a constant current is measured. In the second part the BSCCO shielding tube is installed inside and the residual field is measured. It is measured at the center of the tube and also along the axis. Also a measurement of the residual field stability over 4 days at 1 T external field and 14 h at 1.4 T is performed. The limit 1.4 T is chosen because of the mechanical stability of the shielding tube due to the Lorentz force described in sec. 4.3. The main measurements are shown in tab. D.1 in appendix D and all measurements listed in tab. D.2, tab. D.3 and tab. D.4. The following types of measurements are carried out:

- Measurement of the the external magnet: The magnetic field generated by the external magnet as a response to the current generated by the current supply was measured, and the functional relation between the current of the external magnet and the magnetic flux density determined. As a comparison to the residual field on the axis of the shielding tube, the field map of the external magnet has to be measured.

- Residual field measurement in the shielding tube: The shielding tube is installed on the insert that is slid into the dewar and fixed in position. The dewar is filled with liquid helium. When the tube system is covered with the liquid, the measurement starts. The external field is increased in positive and negative direction and the residual field in the center of the shielding tube measured.

- Residual field measurement with the Zero-field magnet: We expect to detect an extremely low signal in the Hall probe when the magnetic field from the external magnet is shielded. A secondary magnet (Zero-field magnet described in sec. 6.1.4) between the Hall probe and the shielding tube, is used to test the Hall probe functionality also in case the signal is very low. Turning on the current in the Zero-field magnet

generates a magnetic field of known value and therefore a signal of the Hall-probe can be detected to ensure its functionality.

For acquiring the data, the current of the Zero-field magnet is increased and the values of the magnetic flux density taken as measured by the Hall probe at equidistant current values. We read back the current and the Hall voltage and get a relation between the current and the magnetic field. These data are plotted and linearly fitted to estimate the value at zero current (zero magnetic field) of the Zero-field magnet. In the following, this is called the "inc." (increase) value. The same procedure is done by reducing the current and thus the magnetic field to zero, this value is called "dec." (decrease). Two additional data points are obtained, one before the "inc.", and one before the "dec." measurement starts. The Zero-field magnet is still off but the Hall-probe is measuring. This data points are called "0 inc." or "0 dec." respectively.

- Field map of the shielding tube: Measuring the residual field along the axis of the tube at constant external field (1 T and 1.4 T).

- Stability of the shielding tube: Measuring the residual field in the center at a constant external magnetic field (1 T and 1.4 T) versus time.

Treatment of the nonzero residual field in the shielding tube. In the measurement of the residual field in the shielding tube, the offset is defined as the measured residual field, when no magnetic field is applied externally. The following components contributing to the offset are independent from the field of the external magnet: The temperature dependent offset of the Hall probe itself (1.9 G at room temperature), the temperature dependent fluctuations of the Hall-probe, the earth magnetic field (< 0.5 G), contributions from local fields and also from the voltmeter measuring the Hall-voltage.

Another contribution to the offset comes from the residual field in the shielding tube. The dewar was filled with liquid helium at a different location than the laboratory for the experiment. This is important to take into account, since the magnetic field inside the shielding tube, when the shielding tube was cooled below the superconducting temperature, remains inside as long as it is superconducting (see sec. 4.2). That means, even if the dewar is filled with liquid helium and transported to another place, the local magnetic field, where the shielding tube got superconducting, is "transported" together with the shielding tube.

And there is a component of the offset depending on the external field, that is applied to the shielding tube. In the following the hysteresis-like be-

havior of the shielding tube (see sec. 4.3) will be considered. Let us start the process with zero external field. We increase it to a threshold value, when it begins to enter the shielding tube. Further increase of the external field will result in a residual field. To reduce the residual field again to zero, it is not sufficient to decrease the external field to zero. The external field must exceed the zero point into the negative regime until negative external field enters the shielding tube. In this way the residual field is reduced to zero. This happens solely in case, the negative external field has the same absolute value as the maximum positive external field that was applied. Otherwise the difference appears as an additional offset to the next measurement. The residual field left is therefore treated as a component of the offset of the following measurement. Especially the offset in the first part of the measurement without shielding tube (5.7 G ±0.9 G) is not the same as the offset in the second part of the measurement with the shielding tube (-1.0 G ±0.9 G and -1.4 G ±0.9 G). Nevertheless, in this experiment the determination of the difference between the residual field when the external field is turned off and the residual field when the external magnet is increased is of interest. The offset is subtracted from all values of the residual field measurement. The difference in the residual field is then independent from all contributions to the offset as long as they are constant in time on the time scale of the duration of the measurement.

6.3 Analysis of the measurements

6.3.1 Estimation of the uncertainty in the magnetic field measurement

The uncertainty in the magnetic field measurement is generated by the uncertainty in the Hall probe output voltage, and the volt meter that is connected to the Hall probe sensor. The main source of uncertainty in the measurement of the magnetic field is found in the Hall voltage readout device. For the investigation of the Hall voltage fluctuation, the output of the voltmeter is recorded for 14 hours. This is shown in fig. 6.13. The first two hours the voltage rises due to warming up of the voltmeter. A statistical analysis is performed in intervals of two hours distributed in six parts over the whole time range. For each data set, a mean value μ and a standard deviation σ is determined from a Gaussian fit $P(x) = \frac{1}{\sigma\sqrt{2\pi}} e^{-(x-\mu)^2/2\sigma^2}$ to the data, where x is the Hall voltage. The results for σ are shown in fig. 6.15. The Gaussian fit to each data set is shown in fig. 6.14. The reduced χ^2, χ^2/ndf, where ndf is the number of degrees of freedom, is also shown. In the 4th interval, $\sigma = 0.14$

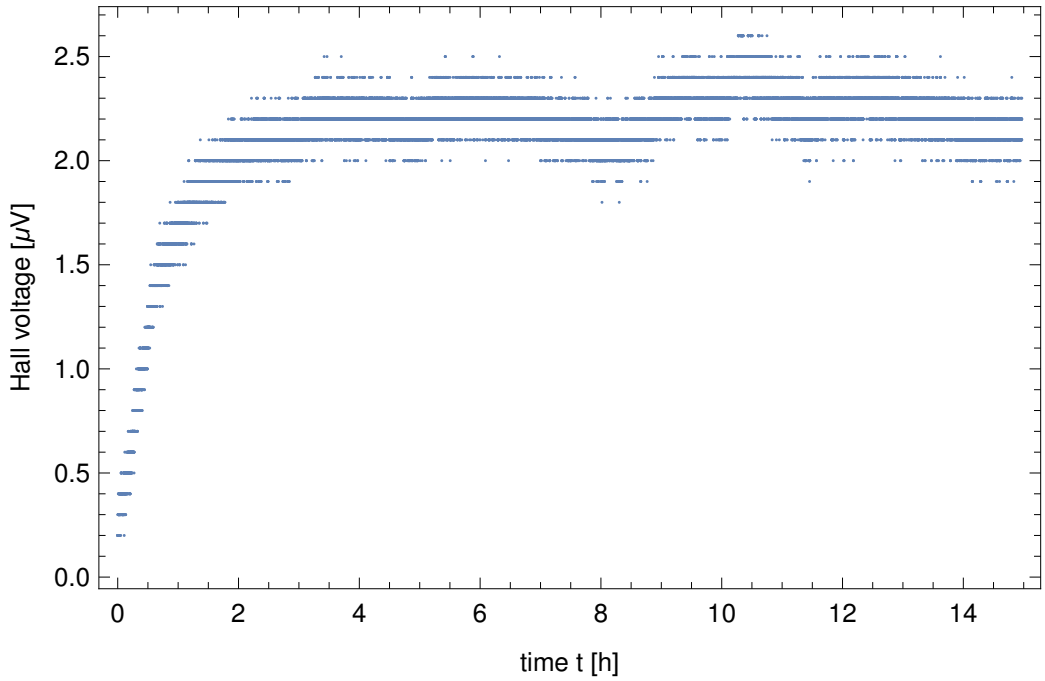

Fig. 6.13: Fluctuation and drift of the voltmeter measuring the Hall voltage at room temperature. In the first two hours the voltmeter needs to warm up. After this phase, the statistical uncertainty is determined by partitioning of the time axis into two hour sections and projection of the data points onto the vertical axis, and fitting a Gaussian distribution to the data (fig. 6.14).

µV is the largest. This corresponds to 0.17 G (converted value of the Hall voltage to a magnetic field using the conversion factor at helium temperature 0.821 mV/kG). This is the value that is applied as a the statistical error to all Hall voltage data taken during the experiment. This leads sometimes to an overestimate of the error. The drift given by the manufacturer for a 24 h measurement is maximal 0.6 µV corresponding 0.73 G. A conservative estimate for the uncertainty in the magnetic field measurement is therefore $\Delta B = \sqrt{0.73^2 + 0.17^2}$ G = 0.75 G.

6.3.2 Magnetic field of the external magnet

Because a stabilization of the current with the power supply, used as a current supply for the external magnet, was not successful, a mode was used, where the voltage is stabilized. This is not the usual mode to operate a magnet. It is described here, how the difficulty of taking a measurement at a stable current value was dealt with. A voltage is set, and the current approximates a stable

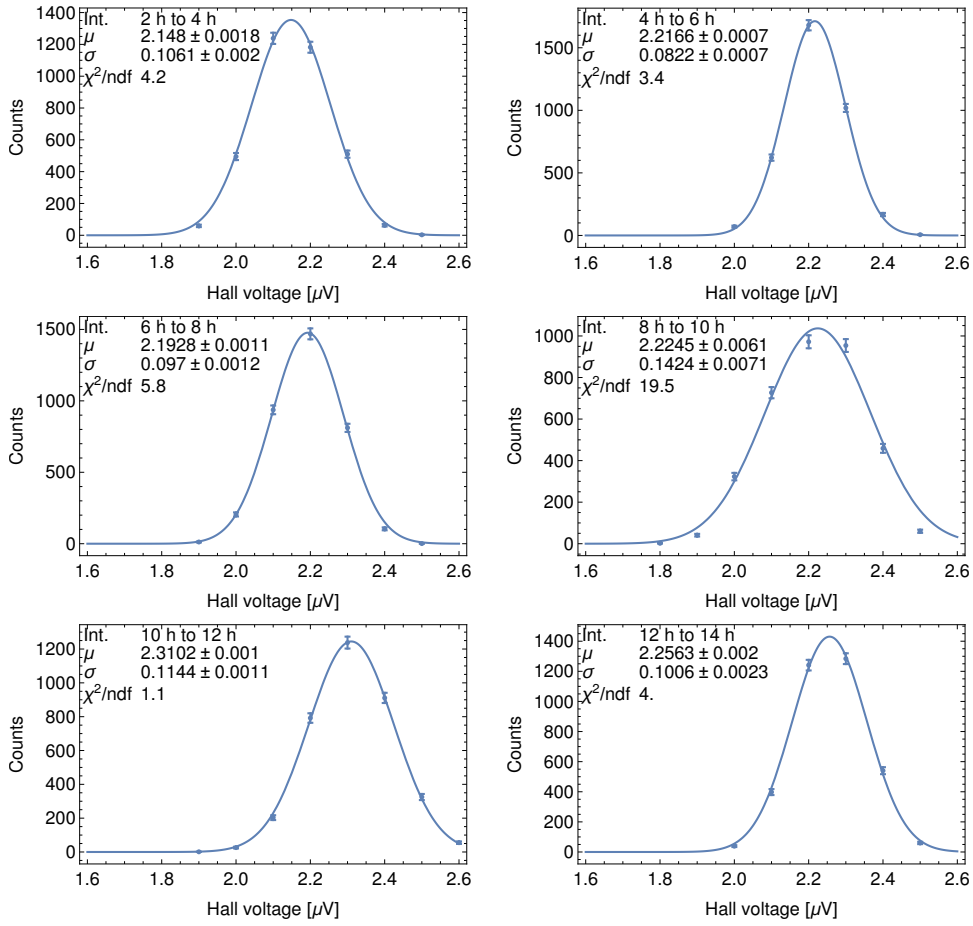

Fig. 6.14: Statistical analysis of the fluctuation of the Hall voltage readout device, to determine the uncertainty of the output. The 12 hours long measurement is divided into intervals of two hours and shown in a histogram with bins of 0.1 μV. The standard deviation σ is determined for all six histograms and in fig. 6.15 plotted against the measuring time.

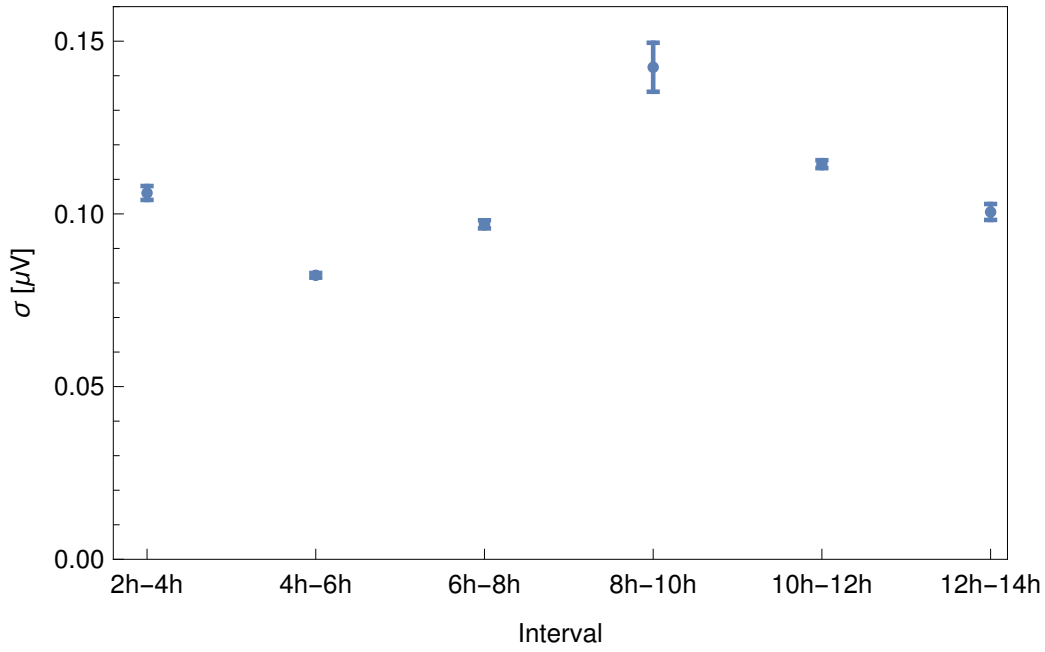

Fig. 6.15: Standard deviations σ from fig. 6.14 in two hour intervals of the fluctuation of the Hall voltage plotted against the measuring time.

value. The magnetic field strength is measured at stability of the current, i.e. the mean value of those data points where the current is constant for at least 20 s, and the reading of the built in voltmeter of the current supply settled down. The evolution of the current and the external magnetic field as a function of time is shown in fig. 6.16. A detailed view on the points at stability is shown in appendix E.

A linear fit function f_{ext} of the form

$$f_{ext}(x) = ax + c \tag{6.1}$$

is fitted to the data. The fit result and the residuals (difference between data points and fit function) are shown in fig. 6.17. By looking at the residuals one realizes that the linear fit does not describe the data well. This might be because of some magnetic material in the setup. A nonlinear fit of a parabolic model f_{ext} of the form

$$f_{ext}(x) = ax + bx^2 + c \tag{6.2}$$

is applied to the data with the parameters a,b and c and the variable x. The result of the fit is shown in the table in fig. 6.18c. The uncertainty of the data is determined mainly by the error of the power supply of the external

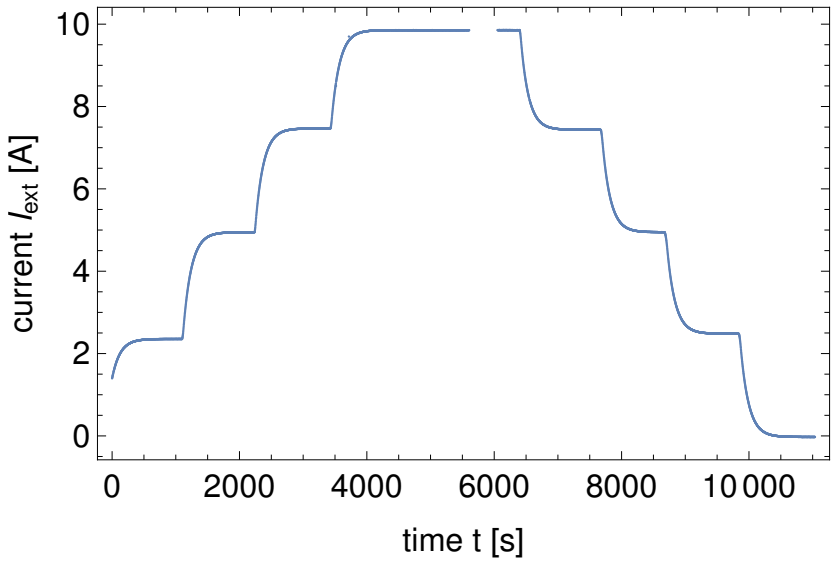

(a)

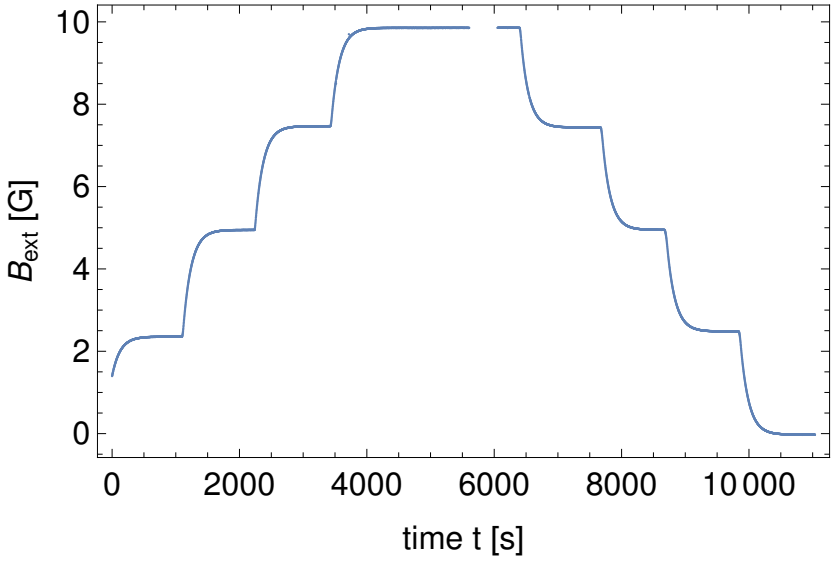

(b)

Fig. 6.16: a) Current of the external magnet vs. time. b) Magnetic flux density vs. time measured with the Hall-probe. The data points estimated to be stable are at the horizontal part of the steps. Here the current is stable and the Hall voltage shows the same value within the uncertainty.

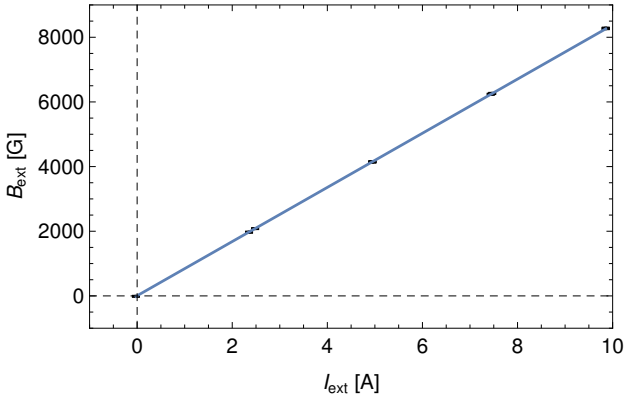

(a)

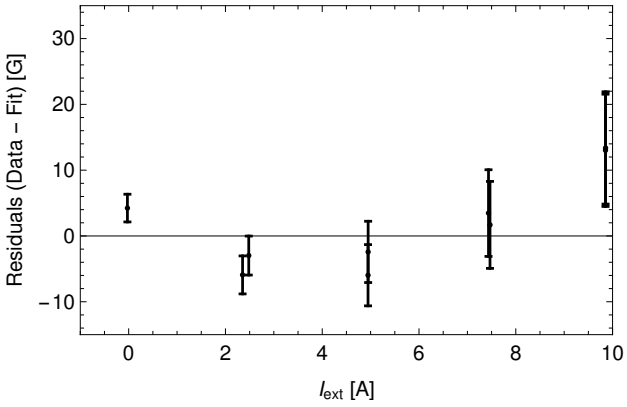

(b)

$f_{ext}(x) = ax + c$				
Slope(a)	σ_{slope}	Offset(c)	σ_{offset}	χ^2/ndf
837.6	0.5	5.5	1.8	2.3

(c)

Fig. 6.17: a) Magnetic flux density vs. the current of the external magnet and linear fit to the data. b) The residuals (difference between data points and fit function) of the fit show a nonlinear behavior. c) Table of fit results.

magnet. The error in the current is propagated to the error in the magnetic field. After a parabolic fit the residuals are smaller than the uncertainty of the data points. This is not the case for a linear fit. This subject is still open and one needs additional data points at higher magnetic fields. The plot of the data, the fit and the residuals are shown in fig. 6.18. The covariance matrix $M_{a,b,c,x}$ of the parameters a, b, c and x is

$$M_{a,b,c,x} = \begin{pmatrix} 1.37 & -0.16 & -1.15 & 0 \\ -0.16 & 0.02 & 0.10 & 0 \\ -1.15 & 0.10 & 2.71 & 0 \\ 0 & 0 & 0 & 10^{-6}x^2 \end{pmatrix} \tag{6.3}$$

and

$$\nabla f_{ext}(x) = \begin{pmatrix} \frac{\partial f(x)_{ext}}{\partial a} \\ \frac{\partial f(x)_{ext}}{\partial b} \\ \frac{\partial f(x)_{ext}}{\partial c} \\ \frac{\partial f(x)_{ext}}{\partial x} \end{pmatrix} = \begin{pmatrix} x \\ x^2 \\ 1 \\ a + 2bx \end{pmatrix} \tag{6.4}$$

The variance of the magnetic field measurement is

$$\begin{aligned} &\nabla f_{ext}(x) M_{a,b,c,x} \nabla f_{ext}(x)^T \\ &= 2.71 - 2.30x + (1.57 + 10^{-6}a^2)x^2 \\ &+ (-0.31 + 4 \cdot 10^{-6}ab)x^3 + (0.02 + 4 \cdot 10^{-6}b^2)x^4 \end{aligned} \tag{6.5}$$

The field map of the external magnet was measured. In the plot in fig. 6.19 the stability of the current of the external magnet during this measurement is shown. The stability ensures that for all data points the only variable is the position on the axis of the external magnet, and that the current is constant. The error bars overlap and form the broad band in the diagram. The mean value is $I_{ext} = (9.88 \pm 0.01)$A. The magnetic field is (8280 ± 10) G when the Hall probe is at the center position of the tube. The value of the magnetic flux density along the axis of the tube, that was measured with the Hall-probe, is shown in fig. 6.20. [3]

[3] In later measurements of the field map of the residual field, the current of the external magnet and thus the magnetic field is not the same as in this measurement. The value of the external magnetic field at the center ($z = 0$) that correspond to a certain current is calculated by applying the fit function f_{ext} to the current. The field map points are then determined by scaling the field map points from this measurement.

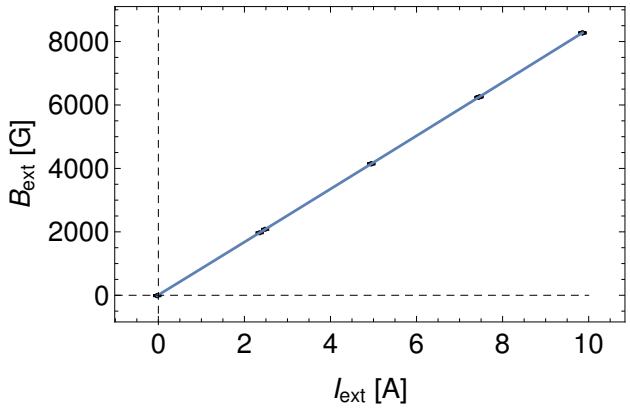

(a)

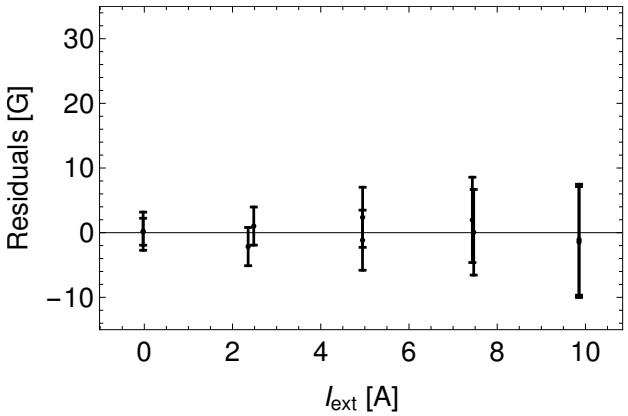

(b)

$f_{ext}(x) = ax + bx^2 + c$		
Parameter	Estimate	Uncertainty
a	833.03 G/A	1.17 G/A
b	0.58 G/A^2	0.14 G/A^2
c	9.42 G	1.65 G
χ^2/ndf	0.2	

(c)

Fig. 6.18: a) Magnetic flux density vs. the current of the external magnet. The result of the linear fit in fig. 6.17 implies that a small second order contribution to the linear fit function reduces the fit residuals. b) Residuals (difference between data points and fit function) of the second order polynomial. c) Table of fit results.

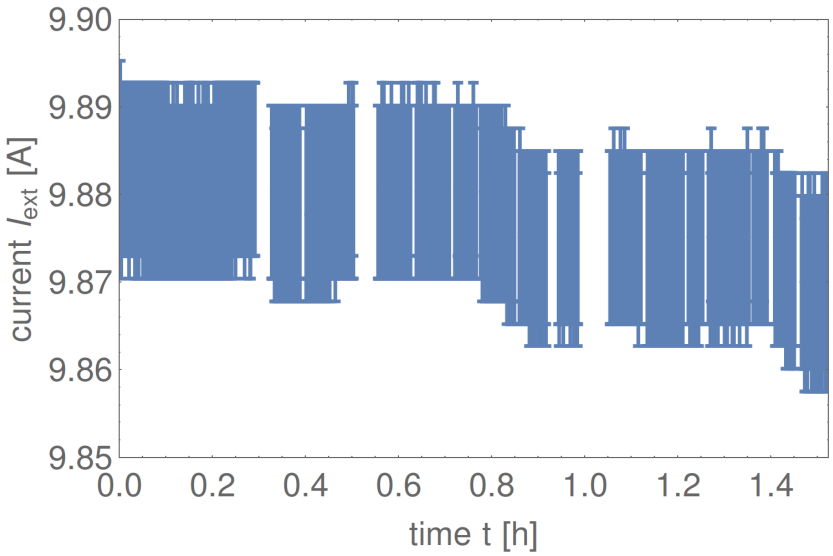

Fig. 6.19: Stability of the current supply of the external magnet during the measurement of the field map of the external magnet. The maximum variation is within the uncertainty of the device specification of 0.1% *of the reading of the device.*

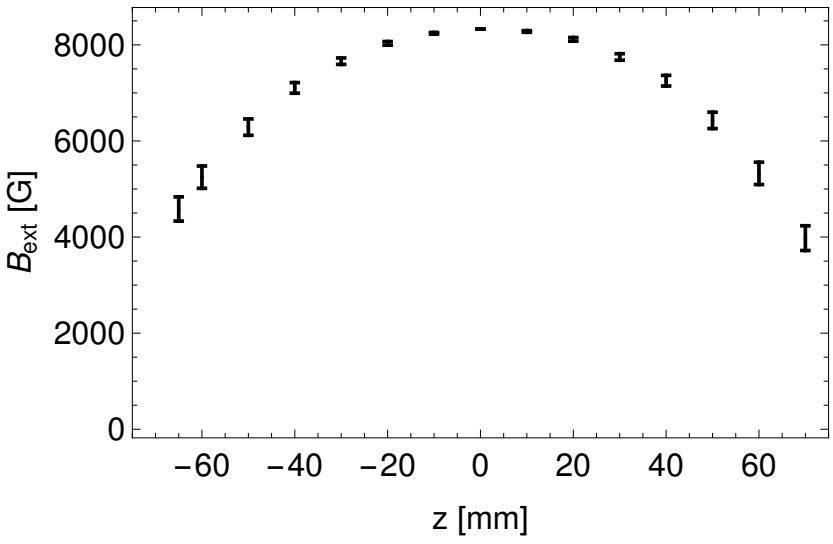

Fig. 6.20: The magnetic field along the axis at a constant current of the external magnet is measured.

6.3.3 Measurements at 1 T

Residual field of the shielding tube. In fig. 6.21 the data points of the residual magnetic field in the center of the shielding tube by increasing the external magnetic field to 1 T are shown. The mean value μ_{meas} is calculated as usual

$$\mu_{meas} = \frac{1}{N}\sum_{i=1}^{N} x_i = -1 \text{ G} \tag{6.6}$$

The mean value is defined as the offset and subtracted from all data. A Histogram of the data points (projection on the B_{res}-axis) (fig. 6.22) shows a fluctuation of

$$\sigma_{res} = \sqrt{\frac{1}{N(N-1)}\sum_{i=1}^{N}(x_i - \mu_{res})^2} = 0.016 \text{ G} \tag{6.7}$$

The x_i are the N recorded stable data points (see sec. 6.3.2). In the calculation of the μ_{meas} and σ_{res} also data from operation of the Zero-field magnet are included. The linear fits to the data points are shown in fig. 6.23. The external field B_{ext} and the residual field B_{meas} and its uncertainty as measured with the Zero-field magnet after subtraction of the offset -1 G are summarized in the table. From this result one can conclude that, besides the offset, no residual field is entering the shielding tube by increasing the external field up to 1 T. Since ($d = 3.5 \pm 0.2$) mm, $\mu_0 = 4\pi \cdot 10^{-7}$Vs/Am and $B_{\text{ext}} = (10140 \pm 14)$ G (this is the external field that was shielded) the average current density is $J_{ind} = (23000 \pm 2000)\frac{\text{A}}{\text{cm}^2}$. The uncertainty of the average current density σ_J is calculated via

$$\sigma_J^2 = \frac{\sigma_{ext}^2}{(\mu_0 d)^2} + \frac{B_{ext}^2}{(\mu_0 d^2)^2}\sigma_d^2 \tag{6.8}$$

The uncertainty in the wall thickness of the shielding tube, σ_d^2, is the main source of uncertainty when calculating the average current density. The shielding factor SF is defined as

$$SF = \frac{B_{ext}}{B_{res}} \tag{6.9}$$

and is extracted from the results for the residual field. Since the denominator for this case is compatible with zero within the uncertainty, the calculation of the shielding factor require to use a Monte-Carlo (MC) simulation, where two normally distributed random numbers are generated, the ratio calculated and the absolute value of the result aggregated. Another method is an analytical

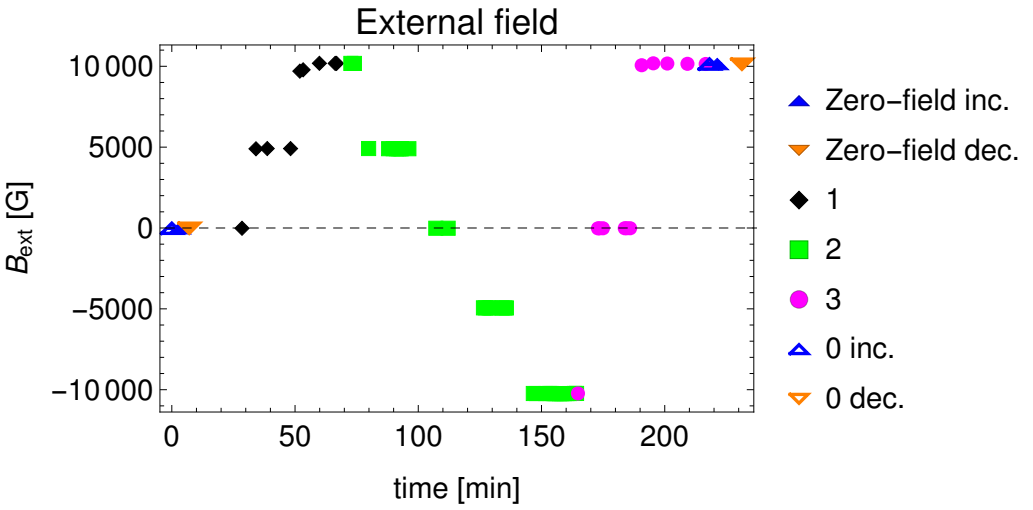

(a)

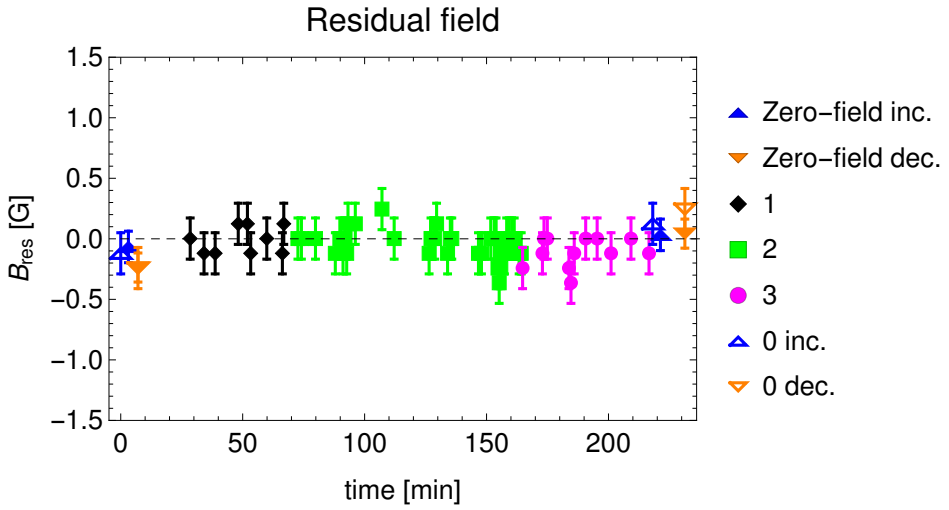

(b)

Fig. 6.21: External B_{ext} and residual magnetic field B_{res} vs. time in the center of the shielding tube by increasing the external magnetic field to 1 T (10^4 G). a) The symbols denote the value of the external field during the increasing procedure (data points 1. in black and 3. in magenta) and the decreasing (data points 2. in green) exactly at the time when the residual field was measured. The filled triangles are estimates of the residual field by using the Zero-field magnet. The open triangles are the values obtained just before the Zero-field magnet measurement started. The apex of the triangle indicates the increasing and decreasing procedures of the Zero-field magnet measurement. b) Residual field at the center of the tube. The offset -1 G is subtracted from the data.

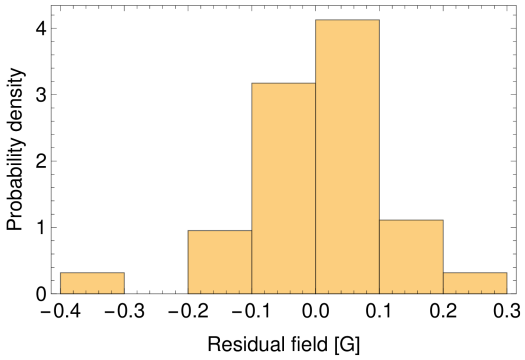

Fig. 6.22: Histogram of the residual field values obtained while increasing the external magnet to 1 T and decreasing to -1 T. The binning of the values is 0.1 *G. The total number of events in the histogram is 63. The offset is defined as the mean value of this data set* $\mu_{meas} = -1$ *G and this is subtracted from all data. Therefore the mean value after subtraction of the offset* μ_{res}*, as shown here, is* $\mu_{res} = 6 \cdot 10^{-18} \approx 0$*. As shown in the text, the fluctuation is* $\sigma_{res} = 0.016$ *G.*

μ_e	10140
σ_e	14
μ_r	0.000
σ_r	0.016
Max. SF in MC	2.52×10^{11}
MC simulated	10^6
Mode of SF dist.	454594
95 % C.L.	ca. $3.2 \cdot 10^5$

Tab. 6.11: Results from the Monte-Carlo simulation

calculation of a ratio distribution of two normal distributions. Both are described in the next sections.

By assuming two normal distributions $\mathcal{N}\{\mu_{e,r}, \sigma_{e,r}\}$ with mean $\mu_{ext,res}$ and variance $\sigma_{ext,res}$, 10^6 random numbers are generated for each of these distributions. For $x \in \mathcal{N}\{\mu_e, \sigma_e\}$ and $y \in \mathcal{N}\{\mu_r, \sigma_r\}$, the ratio $sf = |\frac{x}{y}|$ is calculated whenever y is not zero. The results are aggregated and a distribution $\mathcal{SF}$ is obtained. The resulting probability density function $\mathcal{SF}$ together with the shielding factor at a confidence level of 95% (0.05-quantile), that is considered as a lower limit (ca. $SF_{2\sigma} = 3.2 \cdot 10^5$), are shown in fig. 6.24. The results are summarized in tab. 6.11. The numerical stability of the MC calculation was tested. The results can be found in appendix F.

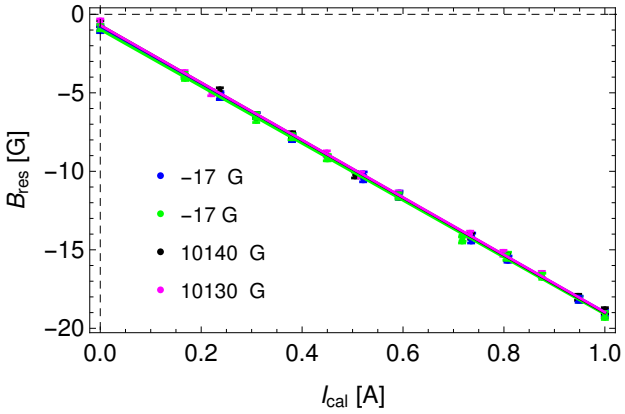

Mod.	B_{res} [G]	σ_{res} [G]	B_{ext} [G]	σ_{ext} [G]	Slope [G/A]	σ_{slope} [G/A]	χ^2/ndf
inc	0.2	0.13	-17	2	−18.18	0.2	0.1
dec	0.03	0.12	-17	2	−18.13	0.19	0.6
inc	0.3	0.13	10140	14	−18.31	0.2	0.5
dec	0.31	0.12	10130	14	−18.28	0.2	0.5

Fig. 6.23: Linear regressions at different external fields obtained with the Zero-field magnet. The current in the Zero-field magnet I_{cal} is increased and decreased and the magnetic field measured with the Hall-probe, while the external magnet is at a constant value (-17 G and 10140 G). In total four different linear fits are obtained (the offset is not subtracted from the data). The value of the magnetic field created by the external magnet while the data were taken can be found in the legend of the plot. The data are summarized in the table (with subtraction of the offset).

Parameter	μ [G]	σ [G]
B_{ext}	10140	14
B_{res}	0.000	0.016

Tab. 6.12: External and residual field used as location and scale parameter of the normal distributions taken for the calculation of the shielding factor.

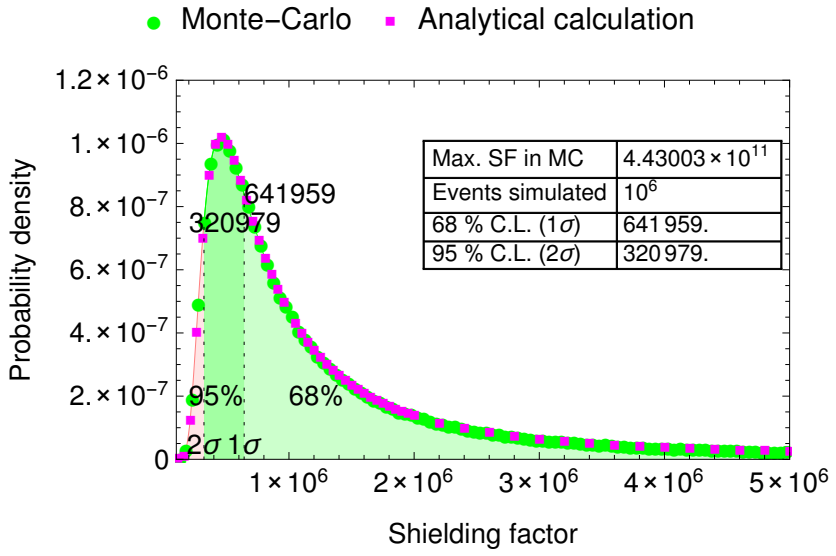

(a)

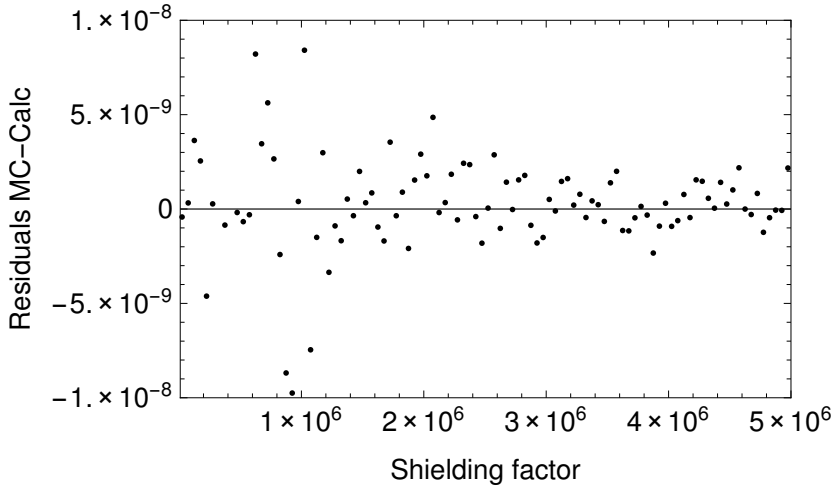

(b)

Fig. 6.24: a) Probability density function for the shielding factor as obtained via Monte-Carlo calculation compared to the analytical calculation. The maximum event in the MC, $2.52 \cdot 10^{11}$ *is not shown in this plot. The probability is decreasing for higher shielding factor events. and b) Residuals, difference between MC and the analytical calculation. The two methods lead to the same result at the order of* 10^{-8}.

By considering the joint probability of the random vector $Z = X/Y$ one can calculate the joint probability density function f analytically by assuming a normal distribution for g: $g_x(x) = \frac{1}{\sigma\sqrt{2\pi}} e^{-(x-\mu)^2/2\sigma^2}$ and the same for $h_y(y)$. The derivation, as it can be found for example in ref. [89], is shown. X,Y are random variables and $Z = X/Y$ a random vector. For the cumulative distribution function $F_Z(z)$ one gets

$$\begin{aligned} F_z(z) =& P(Z \leq z) \\ =& P(X/Y \leq z) \\ =& P(X \leq zy, y > 0) + P(X > zy, y < 0) \end{aligned} \tag{6.10}$$

$$F_z(z) = \int_0^\infty \mathrm{d}y \int_{-\infty}^{yz} \mathrm{d}x\, f_{X,Y}(x,y) + \int_{-\infty}^0 \mathrm{d}y \int_{yz}^\infty \mathrm{d}x\, f_{X,Y}(x,y) \tag{6.11}$$

After a variable transformation $x = yz \Rightarrow \mathrm{d}x = y\,\mathrm{d}z$ one gets

$$F_z(z) = \int_0^\infty \mathrm{d}y \int_{-\infty}^{yz} y\,\mathrm{d}z\, f_{YZ,Y}(yz,y) + \int_{-\infty}^0 \mathrm{d}y \int_{yz}^\infty -y\,\mathrm{d}z\, f_{YZ,Y}(yz,y)$$

From the cumulative distribution function one can calculate the probability density function

$$\frac{\mathrm{d}F_z(z)}{\mathrm{d}z} = \int_{-\infty}^\infty \mathrm{d}y\, |y| f_{YZ,Y}(yz,y) \tag{6.12}$$

If X and Y are independent $f_{X,Y}(x,y) = g_X(x)h_Y(y)$. $\mathcal{SF}$ is then

$$f(z) = \int_{-\infty}^\infty y g_{YZ}(yz) h_Y(y)\,\mathrm{d}y \tag{6.13}$$

$$\begin{array}{rcl} g & : & \text{Probability density function } \mathcal{N}\{\mu_e, \sigma_e\} \\ h & : & \text{Probability density function } \mathcal{N}\{\mu_r, \sigma_r\} \\ f(z) & : & \text{Probability density function } \mathcal{SF} \end{array}$$

We plot the resulting distribution function by using values for the location and scale parameters that can be found in tab. 6.12. and compare it to the Monte-Carlo calculation in fig. 6.24. The two different methods lead to the same result.

Stability and field map of the residual field. The stability of the residual field of the shielding tube was measured at a constant external magnetic field for 4 days. In the first 10 hours a rise in the residual field cannot be observed. (fig. 6.25). The mean value μ of the fluctuation of the residual

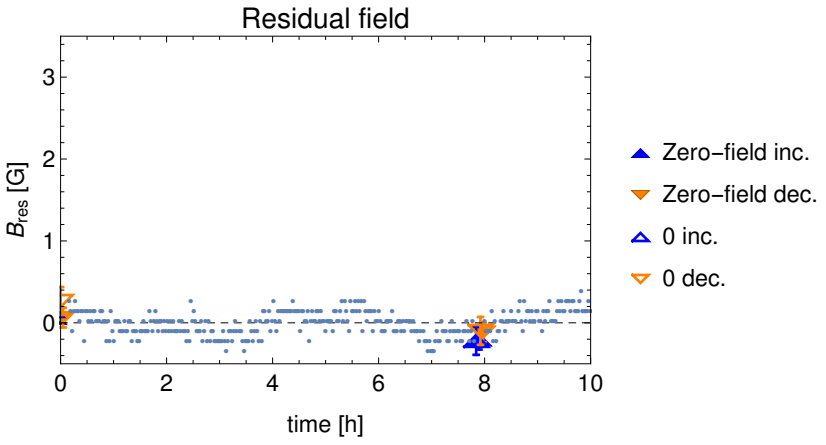

(a)

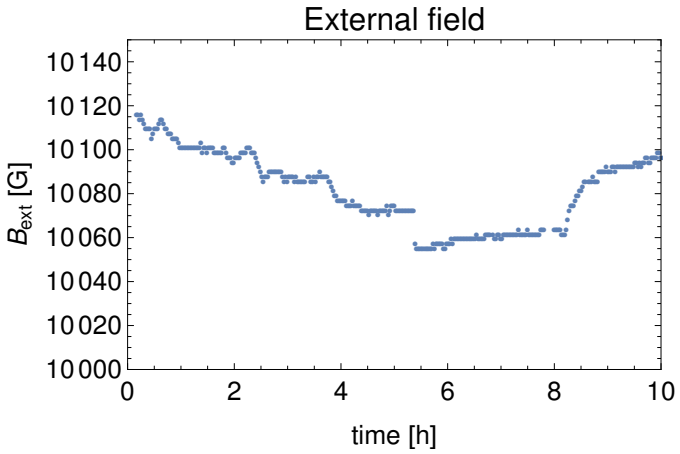

(b)

Fig. 6.25: a) Stability measurement of the shielding tube at an external magnetic field of ca. 1 T for 10 hours. b) Drift of the external field. Symbols as in fig. 6.21

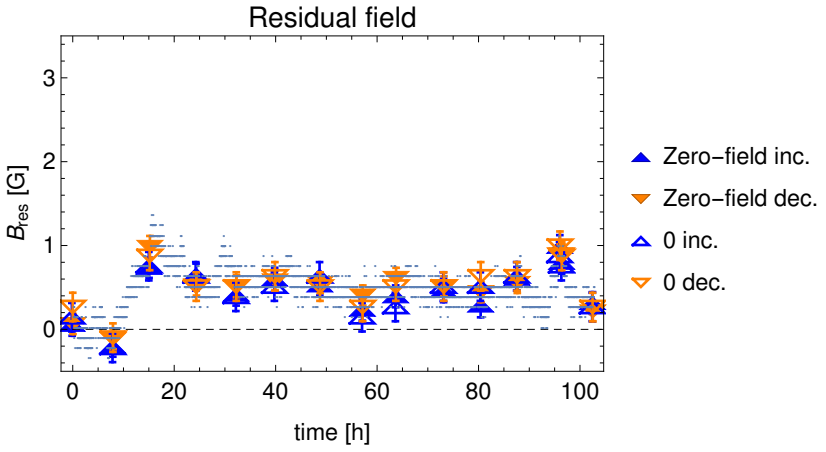

(a)

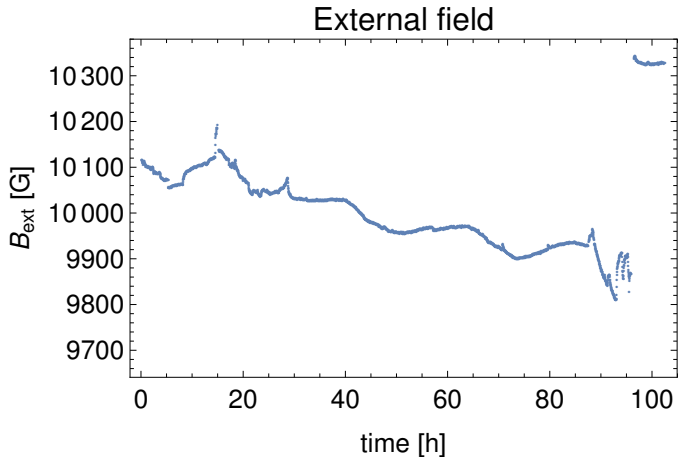

(b)

Fig. 6.26: a) Stability measurement of the shielding tube at an external magnetic field of ca. 1 T for 4 days. b) Drift of the external field. During the measurement, the magnetic field decreased slowly, due to the power supply of the external magnet that was in constant voltage mode. Close to the end of the measurement, after ca. 100 h, the current of the external magnet is increased, so the magnetic field is above 1 T again. Symbols as in fig. 6.21

	0 to 10 h		20 h to 100 h	
Parameter	μ [G]	σ [G]	μ [G]	σ [G]
B_{ext}	10081	14	10000	200
B_{res}	0.000	0.008	0.499	0.003

Tab. 6.13: Mean value μ of the residual field B_{res} and its uncertainty σ for the stability measurement at 1 T after subtraction of the offset (-0.751 ± 0.008) G.

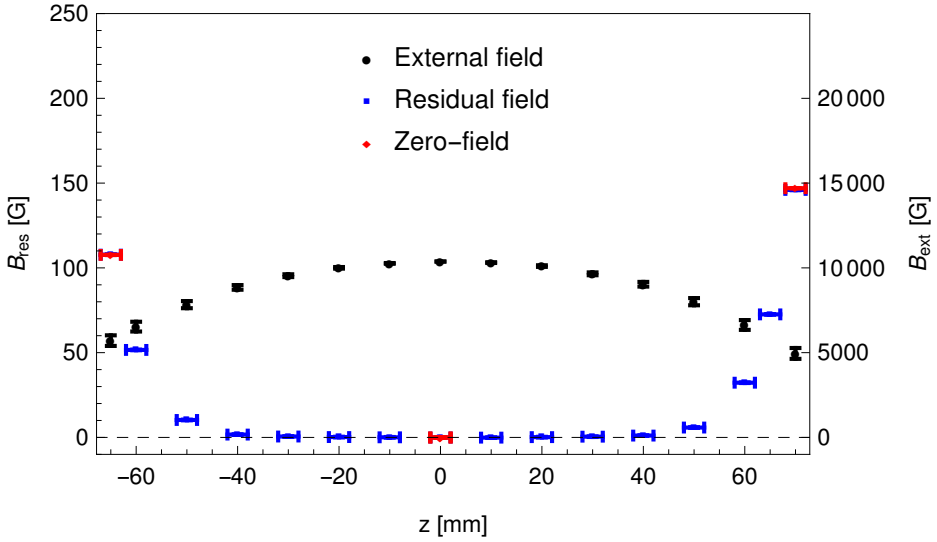

Fig. 6.27: External and residual field along the axis of the tube. The black points show the external field. The blue points are the residual field and the red ones estimated values with the Zero-field magnet.

field B_{res} and its uncertainty σ are summarized in tab. 6.13. One can see in fig. 6.26, after ca. 9 hours the residual field undergoes a quite fast jump within a few hours. After this jump the residual field stabilizes again.

The residual field along the axis of the shielding tube was measured at an external field of (10330 ± 14) G at the center of the tube. The shielded length, where the residual field is lower than 1 G, is 80 mm. Since the tube length is 150 mm, at more than half of the length of the shielding tube the residual field is less than 1 G. The plot is shown in fig. 6.27. The stability of the current supply of the external magnet is shown in fig. 6.28.

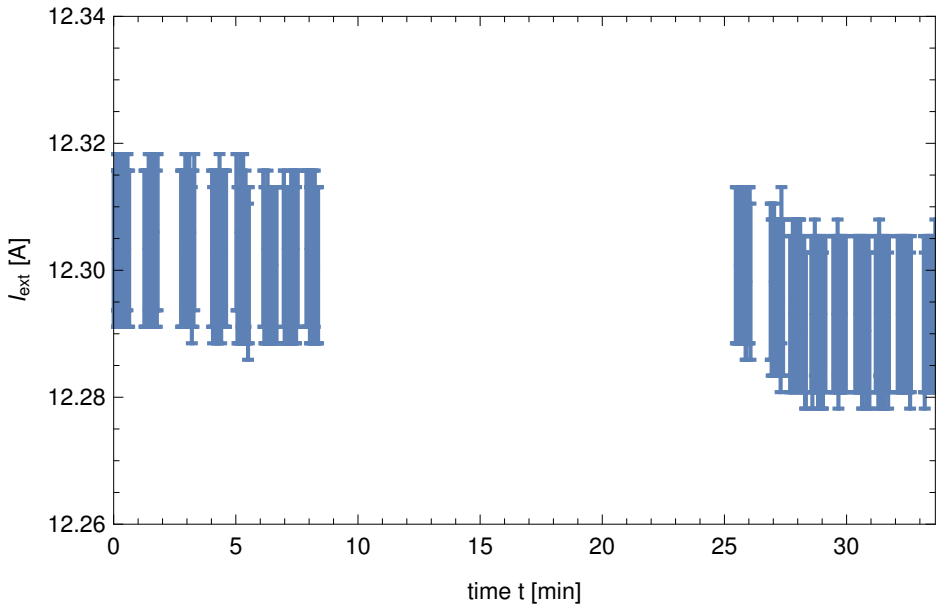

Fig. 6.28: Stability of the current supply of the external magnet in the measurement of the shielding tube field map at 1 T. The measurement was interrupted in the time interval between 8 min and 25 min.

6.3.4 Measurements at 1.4 T

Residual field at the center of the tube at 1.4 T. The same procedure, as described in section 6.3.3, is carried out, with the difference that the external field exceeds the point where it enters the shielding tube. The Hall-probe is fixed in the center of the tube axis, and the current of the external field rises to a value where the field begins to enter the shielding tube. The ramping of the external field is stopped at ca. 1.4 T. The plot of the residual field vs. the external field is shown in fig. 6.29. The verification of the residual field with the Zero-field magnet is shown in the plots fig. 6.30. The residual field is calculated as follows

$$B_{res} = B_{res}^{max} - B_{res}^{0}$$

where B_{res}^{max} and B_{res}^{0} are the values of the residual field at $B_{ext} = (14640 \pm 30)$ G and $B_{ext} = (17 \pm 2)$ G, respectively. The residual field B_{res}^{max} and B_{res}^{0} are determined from the average over the Zero-field magnet measurements, as listed in tab. 6.14. A shielding factor, $SF = \frac{B_{ext}}{B_{res}} = 12200$, and a current density (as calculated in sec. 6.3.3) $J_{ind} = (33000 \pm 3000) A/cm^2$ results and is summarized in tab. 6.15. The uncertainty of the shielding factor σ_{SF} is calculated via $\sigma_{SF}^2 = \frac{\sigma_{ext}^2}{\sigma_{res}^2} + \frac{B_{ext}^2}{B_{res}^4}\sigma_{res}^2$.

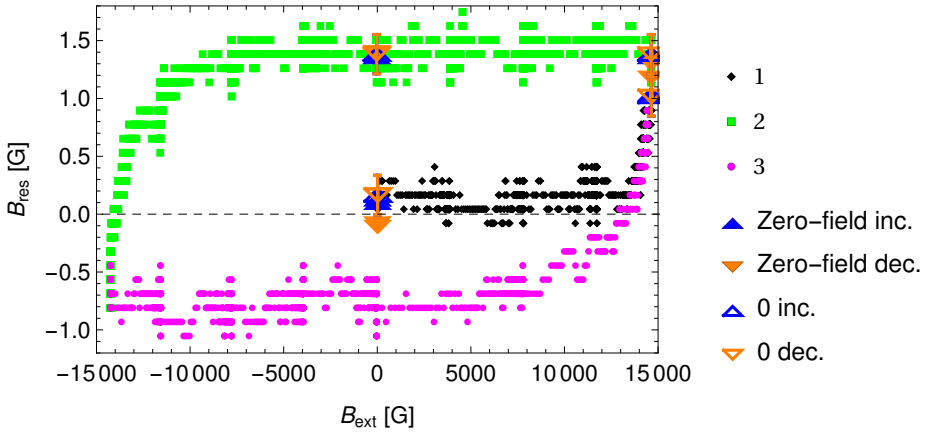

Fig. 6.29: Residual field vs. external field. Symbols as in fig. 6.21. The black line shows the first increasing of the external field. The curve shows a hysteresis. The hysteresis is caused by the irreversible behavior of the shielding tube discussed in sec. 6.2. The offset and the upper limit of the external field is verified with the Zero-field magnet. At the maximum external field of (14640 ± 30) *G the residual field increases to* (1.2 ± 0.06) *G.*

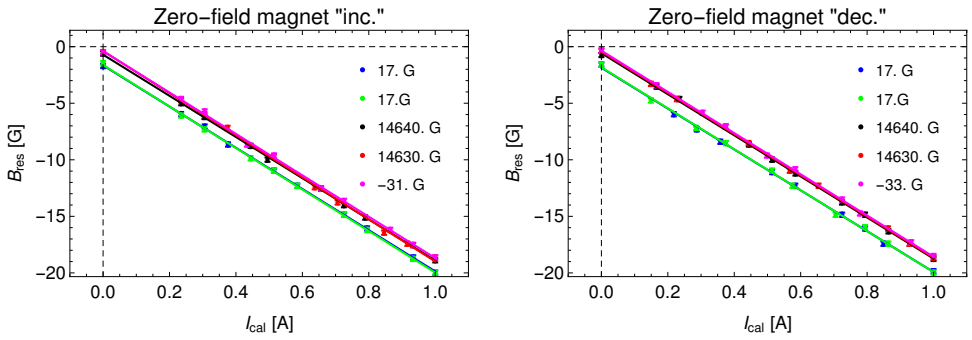

Fig. 6.30: Linear regressions at different external fields obtained with the Zero-field magnet. The different linear fits are obtained at two different states (low and high) of the external magnet before subtracting the offset. The value of the magnetic field created by the external magnet while the data were taken can be found in the legend of the plot. The fit results are listed in tab. 6.14

Time [min]	Mod.	B_{res} [G]	σ_{res} [G]	B_{ext} [G]	σ_{ext} [G]	Slope [G/A]	σ_{slope} [G/A]	χ^2/ndf
0	inc	−0.22	0.13	17	2	−18.21	0.2	0.2
6	dec	−0.43	0.12	17	2	−18.06	0.2	0.9
10	inc	−0.19	0.13	17	2	−18.35	0.2	0.2
14	dec	−0.4	0.12	17	2	−18.1	0.2	1.1
67	inc	0.72	0.13	14640	30	−18.2	0.2	0.4
72	dec	0.86	0.12	14640	30	−18.16	0.2	0.3
77	inc	1.04	0.13	14630	30	−18.6	0.2	1.3
83	dec	0.98	0.12	14630	30	−18.22	0.19	0.4
147	inc	1.04	0.13	-31	2	−18.3	0.2	0.8
157	dec	1.08	0.12	-33	2	−18.21	0.2	0.4

Tab. 6.14: External field B_{ext} and residual field B_{res} and its uncertainty as measured with the Zero-field magnet after subtraction of the offset (-1.44 ± 0.04) G. The measurements show the penetration of the external field into the shielding tube when exceeding 1 T. Because of a hysteresis-like behavior the residual field still remains in the shielding tube after decreasing the external field to zero. The data points and fit functions are shown in fig. 6.30.

Parameter	Value	Uncertainty
B_{ext} [G]	14640	30
B_{res} [G]	1.22	0.06
SF	12000	1000
Current density J_{ind} [A/cm^2]	33000	3000
Offset (subtracted from all data) [G]	-1.44	0.04

Tab. 6.15: External and residual field, shielding factor and estimated average current density at ca. 1.4 T.

Time [min]	Mod.	B_{res} [G]	σ_{res} [G]	B_{ext} [G]	σ_{ext} [G]	Slope [G/A]	σ_{slope} [G/A]	χ^2/ndf
0	inc	0.01	0.15	-6	2	−18.42	0.19	0.1
5	dec	−0.02	0.15	-6	2	−18.3	0.19	0.5
20	inc	0.41	0.16	14790	38	−18.19	0.2	1.1
25	dec	0.53	0.15	14790	38	−18.21	0.19	0.2
889	inc	2.68	0.16	14780	38	−18.2	0.22	1.2
894	dec	2.7	0.15	14780	38	−18.2	0.19	1.4

Tab. 6.16: External field B_{ext} and residual field B_{res} and its uncertainty as measured with the Zero-field magnet during the stability measurement at ca. 1.4 T after subtraction of the offset (1.135 ± 0.085) *G.*

Parameter	Value	Uncertainty
B_{res}	2.7 G	0.15 G
I_{ext}	17.516 A	0.004 A
B_{ext}	14765 G	30 G

Tab. 6.17: Residual field B_{res}, constant current supply I_{ext}, constant external field B_{ext} and its uncertainty for the stability measurement at ca. 1.4 T after 14 hours. The residual field in the shielding tube increases with time.

Stability and field map of the residual field. As for 1 T external field the stability of the residual field of the shielding tube at a constant external magnetic field of (14765 ± 30) G is measured for 14 hours (See the plot in fig. 6.31). In addition to the data points the Zero-field magnet for estimating the residual field was used. The values are in tab. 6.16. The Residual field B_{res}, constant external field B_{ext} and its uncertainty is summarized in tab. 6.17.

The residual field along the axis of the tube was measured at a constant external field of (14793 ± 30) G. The shielded length is 80 mm. The result is similar to that at 1 T. Since the tube length is 150 mm at more than half of the length of the shielding tube the residual field is less than 2 G. The plot is shown in fig. 6.32.

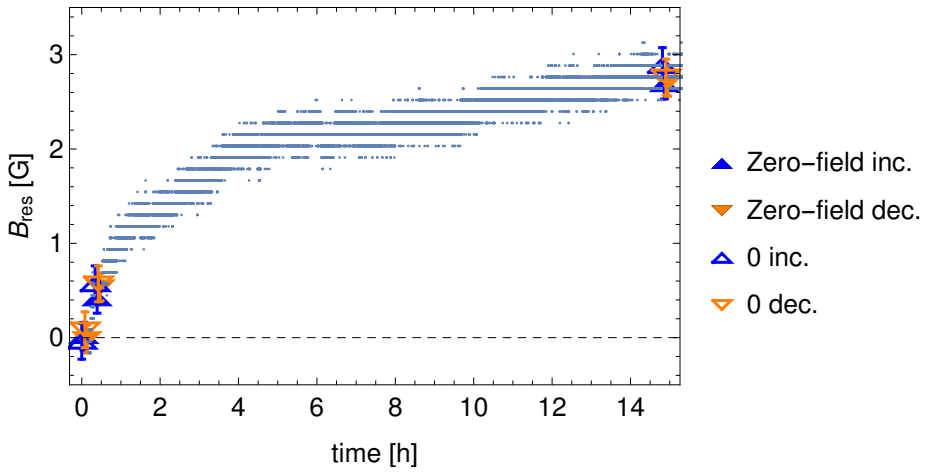

(a)

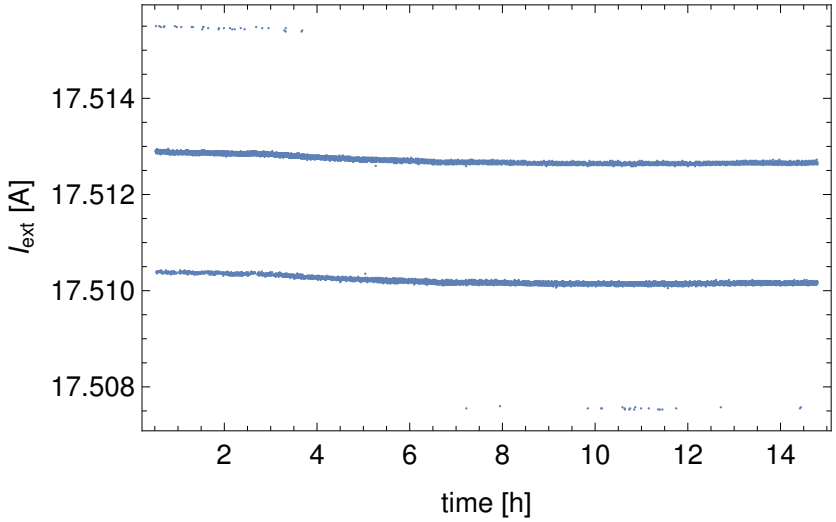

(b)

Fig. 6.31: a) Increasing residual field of the shielding tube at a constant external magnetic field of ca. 1.4 T for 14 hours. Symbols as in fig. 6.21. The offset (1.14 ± 0.08) *G is subtracted. b) Drift of the current supplying the external magnet creating a field of* (14765 ± 30) *G . The uncertainty in the magnetic field is a result from sec. 6.3.2. The uncertainty of the current is 0.05 %.*

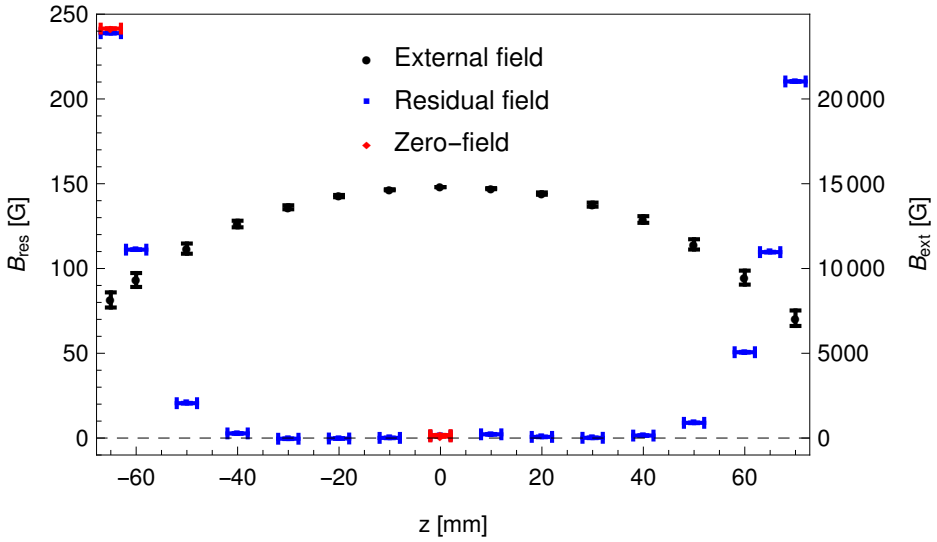

Fig. 6.32: External and residual field along the axis of the tube. The black points show the external field. The blue points are the residual field and the red ones estimated values with the Zero-field magnet.

6.4 Comparison of the simulation with the experimental result

To estimate the validity of the simulation, presented in chapter 5, the results of the calculated field map of the residual field along the axis of the shielding tube is compared with the values from the experiment. For the comparison one needs to apply numerically the same external field as in the experiment. Therefore one needs a function $f_{map}^{fit}(x = 0, z)$ where f_{map}^{fit} is the value of the magnetic field at position z on the axis ($x = 0$ means, the radial distance from the axis is zero). f_{map}^{fit} describes the measured field map best. The procedure to get this function is as follows. The field map $f_{map}(x, z)$ can be calculated via Biot-Savart (s.5.2) for the current $I^{ext} = 1$ A. For any other I^{ext} the function $f_{map}(x, z)$ is scaled linearly with I^{ext}, in fig.6.4 the function $f_{map}(x, z)$ is shown by using $I^{ext} = 12$ A for the calculation. By using the current $I^{ext} = 9.88$ A, $c \cdot f_{map}(x = 0, z)$ with fit parameter c can be fitted to the measured data. The fit result for c is shown in tab.6.18 and plotted with the measured data in fig.6.33 a). The residuals in fig.6.33 b) show a deviation from the calculated form [4]. The external current for input into the

[4]This can be due to winding errors during winding of the wire into layers of a solenoid. The length of the holding structure has to be adjusted to the wire diameter. The wire

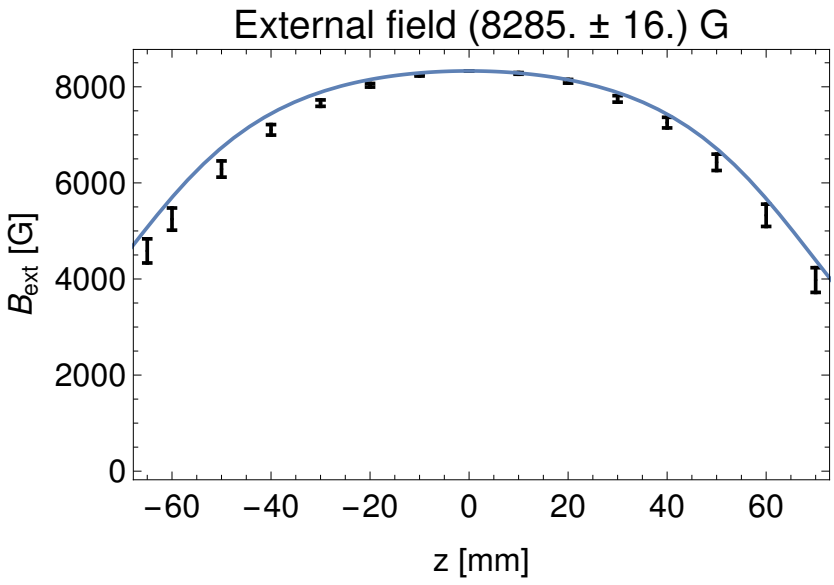

(a)

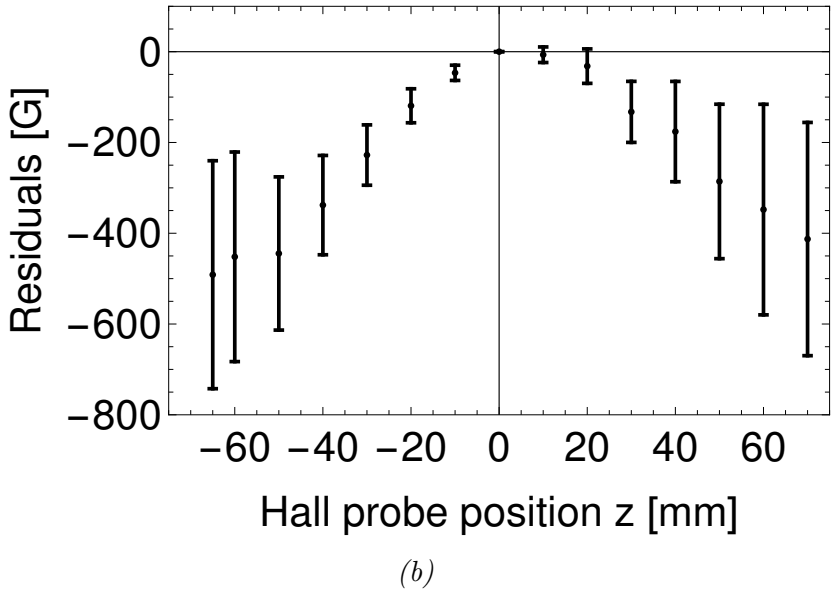

(b)

Fig. 6.33: a) The data points from the measurement are plotted together with the field map $f^{fit}_{map}(x = 0, z)$. b) Residuals (data-fit)

Parameter	Estimate	Uncertainty
c	0.993856	0.000035

Tab. 6.18: Fit result of the calculated magnetic field map to the measured one. The field map can be used as an input to the simulation. With the same field map used for the simulation of the residual field, the result can be compared to the measurement.

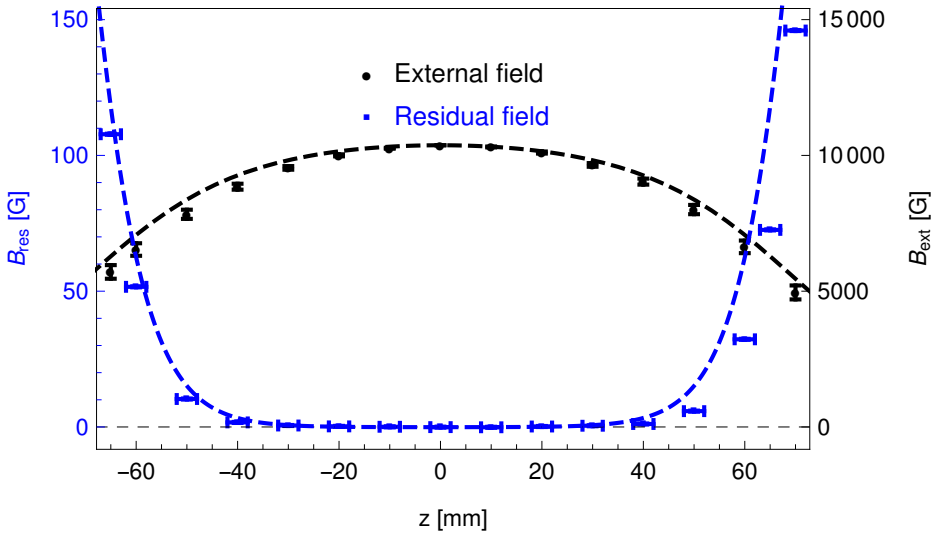

Fig. 6.34: Comparison of simulation and measurement. The black and blue dashed lines are the simulated external and residual field in G with corresponding scales on the right and left, respectively. The points with the error bars are the measured data as described in chap.6.

simulation is then determined by the mean external current (fig.6.19) while measuring the field map of the residual field of shielding tube corrected by the fit parameter c. The result of this comparison is shown in fig.6.34. The simulated residual field follows the measured one within the measurement errors on the left side (negative values of the axis) and in the middle part. The deviation of the measured data points and the simulated curve on the right side has to be studied. The measured data points are slightly shifted on the z-axis with respect to the $z = 0$ position. This can be due to a systematic

diameter alters in the range of some 10 to 100 μm because of the uncertainty of the wire coating during fabrication of the wire and and gluing during the winding procedure. Therefore, the last winding at the end of a layer is not exactly a whole loop. This leads to an imperfection in the profile of the windings and causes the magnetic field to be stronger towards the center, where the windings are well-arranged.

error not taken into account in the analysis. In particular, the position of the sliding rod and the Hall-probe on it. The measurement of points at different z positions require the manually movement of the rod. This would introduce a shift of the residual field map to one side, adding an offset in z direction to the measured data points.

6.5 Summary of the results

The performance of the BSCCO shielding tube concerning the issue of minimizing the longitudinal magnetic flux density, created by an external magnet, was tested. A testing apparatus was built consisting of the following elements: The external magnet is realized by a superconducting coil. It is mounted on the top of the shielding tube. It applies a magnetic field parallel to the wall of the tube. Inside the shielding tube a Hall probe is measuring the residual magnetic flux density. A dewar, that contains the whole testing apparatus, is filled with liquid helium, sustaining the apparatus at a constant temperature of 4.2 K.

The residual field was measured, a shielding factor for 1 T and 1.4 T external field was extracted and the induced average current density in the shielding tube estimated. The residual field along the axis of the shielding tube, where it is lower than 1 G, was determined. A long term stability measurement was performed. The results are summarized in tab. 6.19.

The measurement has shown that with a 150 mm long shielding tube with an inner diameter of 43 mm and a wall thickness of 3.5 mm a magnetic flux density of (10140 ± 14) G can be shielded with a vanishing residual field and an uncertainty of 0.016 G. The shielding factor is at least $3.2 \cdot 10^5$ with a 95 % confidence level. The 4 days long stability measurement at 1 T shows a stable operation of the shielding tube. The residual field does not increase with an uncertainty of 0.008 G until 10 h and stabilizes at $B_{res} = (0.499 \pm 0.003)$ G for the rest of the measured time. At 1.4 T the residual field B_{res} increases to $B_{res} = 2.7$ G after 14 h. The residual field was also measured along the axis of the tube and it shows that the residual field is $B_{res} < 1$ G at the length of 80 mm. Above 1 T the field starts to penetrate into the inner part of the shielding tube. At 1.4 T the residual field in the center of the tube is $B_{res} = 1.2$ G.

External field	1 T	1.4 T
Shielding factor	> 320000 (95 % C.L.)	12000 ± 1000
Average induced current density J_{ind} $[\frac{\mathrm{A}}{\mathrm{cm}^2}]$	23000 ± 2000	33000 ± 3000
Shielded length [mm] (tube length 150 mm)	80 ± 2	80 ± 2
Residual field [G] after 9 h at 1 T and 14 h at 1.4 T	0.0000 ± 0.0024	2.70 ± 0.15
Residual field [G] in the range of 20 to 80 h	0.499 ± 0.003	

Tab. 6.19: Results for measurements with the BSCCO shielding tube at an external field of 1 T and 1.4 T in longitudinal direction (applied parallel to the wall of the tube) at 4.2 K. The tube length is 150 mm and its wall thickness 3.5 mm.

Chapter 7

Conclusion and future development

A transverse polarized target is a highly demanded tool to investigate the nucleon structure in a way that would not be accessible otherwise. In first place, a transverse polarized target in the PANDA detector requires a shielding tube that can shield the 2 T longitudinal field created by the PANDA solenoid with a shielding factor as high as possible to be able to maintain a high degree of transverse polarization. Also a low material budget is required. Therefore a BSCCO high-temperature superconducting hollow cylinder was tested experimentally whether it can shield an intense magnetic flux.

Simulations of the shielding tube where carried out by assuming that the superconductor is an ideal conductor.

It was shown experimentally that a magnetic flux density of (10140 ± 22) G can be shielded. The stability measurement at 1 T external field shows a stable operation of the shielding tube. The residual field was also measured along the axis of the tube and showed the homogeneity of the shielding. Above 1 T the field starts to penetrate into the inner part of the shielding tube and at 1.4 T the residual field is $B_{res} = 1.2$ G.

A comparison of the results of the calculated field map of the shielding tube with the measured data from the experiment showed a good agreement of the calculated values to the data. The calculation can be used to adjust and optimize the geometry of the shielding tube. The calculated field map can be used as an input for particle tracking simulations.

The shielding tube is suitable for shielding 1 T with a good homogeneity and stability, and with a high shielding factor. The shielding tube is sufficient for an operation of a polarized target at 1 T at the temperature 4.2 K if the $\bar{\text{P}}$ANDA solenoid operating point is 1 T. Although, shielding of 2 T would be more desirable. At 1.4 T the shielding performance is reduced. The

applicability depends on which is the maximum residual field that can be accepted, and the required stability in time.

Shielding of more than 1 T with BSCCO would require a thicker tube or an additional BSCCO tube placed inside the first tube. A combination of different superconducting materials could also be an option. Another possibility to enhance the shielding performance, by higher current density, is to lower the temperature, where more experimental studies are needed.

Bibliography

[1] PANDA experiment https : //panda.gsi.de/

[2] http : //www.fair − center.com/

[3] K.A. Olive et al. (Particle Data Group), Chin. Phys. (2014).

[4] P. Achenbach, S. Bleser, J. Pochodzalla, A. Sanchez Lorente, M. Steinen,*Hyper nuclear Physics at PANDA*, Hyperfine Interactions 209, pp. 99-104 (2012).

[5] A. Sanchez Lorente on behalf of the PANDA collaboration,*High precision γ-spectroscopy of $\Lambda\Lambda$-Hypernuclei at the $\bar{P}ANDA$ experiment*, Journal of Physics: Conference Series 426, 012030 (2013).

[6] A. V. Radyushkin, Phys. Part. Nucl. 44 (2013) 469.

[7] R. Maier for the HESR Consortium, *The High-Energy Storage Ring (HESR)*, Proceedings of 2011 Particle Accelerator Conference, New York, NY, USA (2011).

[8] Lehmann, Inti, *Physics Programme of PANDA at FAIR*, Particles and nuclei. Proceedings, 18th International Conference, PANIC08, Eilat, Israel, November 9-14, 2008, 408-410, (2009) arXiv:0909.4237.

[9] PANDA Collaboration,*PANDA - Strong interaction studies with antiprotons*,FAIR-ESAC/Pbar/Technical Progress Report.

[10] PANDA Collaboration, *Technical Design Report for the PANDA Solenoid and Dipole Spectrometer Magnets*, arXiv:0907.0169 [physics.ins-det], 2009.

[11] PANDA Collaboration,*Development of cluster-jet targets: From COSY-11 to FAIR*,AIP Conference Proceedings 950, 85 (2007), arXiv:1404.5988 [physics.ins-det], (2014).

[12] PANDA Collaboration, *Technical Design Report for the PANDA Internal Targets*,http : //www.fair − center.eu/fileadmin/fair/publications$_{e}$xp/PANDA$_{T}$argets$_{T}$DR.pdf, (2012).

[13] A. Freund, A. V. Radyushkin, A. Schafer and C. Weiss, Phys. Rev. Lett. 90 (2003)092001.

[14] B. Pire and L. Szymanowski, Phys. Rev. D 71 (2005) 111501.

[15] K. N. Barish et al., http : //www.bnl.gov/npp/docs/pac0610/Goto$_{r}$hic − drell − yan.pdf (2010).

[16] R. Angeles-Martinez et al., *Transverse momentum dependent (TMD) parton distribution functions: status and prospects*, ACTA PHYSICA POLONICA B 46, (2015) 2501, arXiv:1507.05267 [hep-ph].

[17] P. F. Dahl, p. 324 ff., *Flash of the Cathode Rays A History of J J Thomson's Electron*, Institute Of Physics Publishing Bristol and Philadelphia, 1997.

[18] A. Melissinos, *Experiments in modern physics: Ruther- ford scattering*, Academic Press, (1966) Chap. 6, pp. 226-252.

[19] N. F. Mott, Proc. Roy. Soc. (London) A 124 (1929) 425.

[20] M. E. Rose, *The Charge Distribution in Nuclei and the Scattering of High Energy E1ectrons*, Phys. Rev. 73 (1948) 279.

[21] R. Hofstadter, *Electron scattering and nuclear structure*, Rev. Mod. Phys., 28 (1956) 214.

[22] L. L. Foldy, Phys. Rev. 87 (1952) 688.

[23] M. N. Rosenbluth, Phys. Rev. 79 (1950) 615-619.

[24] F. J. Ernst, R. G. Sachs and K. C. Wali, Phys. Rev. 119 (1960) 1105.

[25] Mohr, Peter J.; Newell, David B.; Taylor, Barry N. (21 Jul 2015). *CODATA Recommended Values of the Fundamental Physical Constants: 2014*, arXiv:1507.07956v1.

[26] A. Akhiezer, and M. Rekalo, Sov. Phys. Dokl. 13 (1968) 572, Dokl. Akad. Nauk Ser. Fiz. 180 (1968) 1081.

[27] A. Akhiezer, and M. Rekalo, Sov. Phys. Dokl. 4 (1974) 277, Fiz. Elem. Chast. Atom. Yadra 4 (1973) 662.

[28] C. F. Perdrisat, V. Punjabi and M. Vanderhaeghen, Prog. Part. Nucl. Phys. 59 (2007) 694 [hep-ph/0612014].

[29] G. Bardin et al. Nucl. Phys. B, 411, 3-32, 1994.

[30] J. P. Lees et al. Phys. Rev. D, 88(7):072009, 2013.

[31] BESIII collaboration, http://bes3.ihep.ac.cn/index.htm

[32] BELLE collaboration, http://belle.kek.jp/

[33] Alaa Dbeyssi, *Study of the internal structure of the proton with the PANDA experiment at FAIR*, Institut de physique nucleare, IPNO-T-13-04 (2013).

[34] G. Bardin et al., Nucl. Phys. B 411, 3 (1994).

[35] BaBar Collaboration (J.P. Lees et al.), Phys. Rev. D88, 072009 (2013) arXiv:1308.1795.

[36] BESIII Collaboration (M. Ablikim et al.), Phys. Rev. D 91, 112004 (2015).

[37] R. Baldini et al., Eur. Phys. J. C 46, 421 (2006) arXiv:hep-ph/0507085.

[38] PANDA Collaboration (Singh, B. et al.), *Feasibility studies of time-like proton electromagnetic form factors at PANDA at FAIR*, Eur.Phys.J. A52 (2016).

[39] E. Tomasi-Gustafsson, M.P. Rekalo, Phys. Lett. B 504, 291 (2001).

[40] Iris Zimmermann, PhD Thesis, Universität Mainz (2017).

[41] A. Zichichi, S.M. Berman, N. Cabibbo and R. Gatto, Nuovo Cimento XXIV, 170 (1962).

[42] Egle Tomasi-Gustafsson, F. Lacroix, C. Duterte and G. I. Gakh, *Nucleon electromagnetic form factors and polarization observables in space-like and time-like regions*, arXiv:nucl-th/0503001.

[43] Huber P. and Meyer K. P. *Proc. Int. Symp. on Polarization Phenomena of Nucleons (Basel, 1960)*, Birkhäuser Verlag (1961), Helv. Phys. Acta Supplementum.

[44] St. Goertz et. al., *Polarized H, D and 3He Targets for Particle Physics Experiments*, Progress in Particle and Nuclear Physics 49 (2002) 403-489.

[45] E. Steffens, W. Haeberli, *Polarized gas targets*, Rep. Prog. Phys. 66 (2003).

[46] Erb, Motchane, and Ubersfeld, Compt. rend. 246, 2121 and 3051 (1958).

[47] A. Abragam and W. G. Proctor, Compt. rend. 246, 2253 (1958).

[48] A. Abragam, et al., Phys. Lett. 2 (1962) 310.

[49] O. Chamberlain, et al., Phys. Lett. 7 (1963) 293.

[50] A. ABRAGAM and M. GOLDMAN, Rep. Prog. Phys., Vol 41, 1978. Printed in Great Britain.

[51] A. Airapetian et al, Eur. Phys. J. C 74 (2014) 3110.

[52] A. Airapetian et al, submitted to EPJC (2017).

[53] R. Gilman et al., Phys. Rev. Lett. 65 (1990) 1733.

[54] F. Rathmann et al., Phys. Rev. Lett. 71 (1993) 1379..

[55] Ferro-Luzzi et al., Phys. Rev. Lett. B (2630) 77 1996.

[56] M.A. Miller et al., Phys. Rev. Lett. 74 (1995) 502.

[57] H. Gao et al., Phys. Rev. C 50 (1994) 546.

[58] C.E. Jones et al., Phys. Rev. C 47 (1993) 110.

[59] C.E. Woodward et al., Phys. Rev. Lett. 65 (1990) 698.

[60] Jin, Kai, JLab Polarized He-3 Target Group Collaboration, APS Meeting Abstracts (2015).

[61] N.R. Newbury et al., Phys. Rev. Lett. 67 (1991) 3219.

[62] N.R. Newbury et al., Phys. Rev. Lett. 69 (1992) 391.

[63] J. Becker et al., Eur. Phys. J. A 6 (1999) 329.

[64] D. Rohe et al., Phys. Rev. Lett. 83 (1999) 4257.

[65] R. De Vita, 9th Conference on the Structure of Baryons, Newport News, March 2002.

[66] B. Larson et al., Phys. Rev. Lett. 67 (1991) 3356.

[67] B. Larson et al., Phys. Rev. A 44 (1991) 3108.

[68] J.R. Johnson et al., Nucl. Instr. and Meth. A 356 (1995) 148.

[69] A. Meier, Ph.D. thesis, University of Bochum, Germany (2001).

[70] J. Ahrens et al., Phys. Rev. Lett. 84 (2000) 5950.

[71] J. Ahrens et al., Phys. Rev. Lett. 87 (2001) 022003.

[72] J. P. Didelez, Nucl. Phys. New Europe 4 (1994) 10.

[73] S. Hoblit et al., (LEGS-Spin Collaboration), Phys.Rev.Lett.102:172002,(2009).

[74] T. IWATA, Electromagnetic Interactions in Nuclear and Hadron Physics, pp. 578-587, (2002).

[75] SD. Drell and A.C. Hearn, Phys. Rev. Lett. 16 (1966) 908.

[76] S.B. Gerasimov, Sov. J. Nucl. Phys. 2 (1966) 430.

[77] W. Buckel, R. Kleiner, *Supraleitung*, Wiley-VCH Verlag(2013).

[78] H. Kamerlingh Onnes, Commun. Phys. Lab. Univ. Leiden. Suppl. 29 (Nov. 1911).

[79] Meissner, W.; Ochsenfeld, R.,*Ein neuer Effekt bei Eintritt der SupraleitfÃ¤higkeit*,Die Naturwissenschaften, Volume 21, Issue 44, pp.787-788, (1933).

[80] Rjabinin, J. N.; Shubnikow, L. W. (1935). *Magnetic Properties and Critical Currents of Supra-conducting Alloys*. Nature. 135 (3415), pp. 581-582, (1935).

[81] Yoichi Ando, G. S. Boebinger, A. Passner, L. F. Schneemeyer, T. Kimura, M. Okuya, S. Watauchi, J. Shimoyama, K. Kishio, K. Tamasaku, N. Ichikawa, and S. Uchida, *Resistive upper critical fields and irreversibility lines of optimally doped high-Tc cuprates*, Phys. Rev. B 60, 12475, Published 1 November 1999.

[82] Charles P. Bean, *Magnetization of high field superconductors*, Rev. mod. phys., January 1964.

[83] S. Eidelman et al., *Review of Particle Physics*, Physics Letters B Volume 592, Issues 1-4, 15 July 2004 Elsevier B.V..

[84] Bock J, Elschner S. and Herrmann P., 1995 IEEE Trans. Appl. Supercond. 5 1409.

[85] D. Dimos, P. Chaudari and J. Mannhart, Phys. Rev. B 41, 4038 (1990).

[86] J. D. Jackson, *Classical Electrodynamics*, sect. 5.17, third edition (1999).

[87] E. B. Rosa, *Bulletin of the Bureau of Standards*, Vol. 4., No. 3., p. 372.

[88] J-F Fagnard, S Elschner, J Bock, M Dirickx, Vanderheyden and P Vanderbemden, *Shielding efficiency and E(J) characteristics measured on large melt cast Bi-2212 hollow cylinders in axial magnetic fields*, Supercond. Sci. Technol. 23 (2010) 095012 (8pp).

[89] J. H. Curtiss, Ann. Math. Statist., Volume 12, Number 4 (1941), 409-421.

Appendix A

Finite element method calculation

Using a commercial program (CST Studio Suite ® 2017) a finite element method calculation was performed with the same geometrical parameters and external magnetic field as in the calculation in chapter 5. The shielding tube is modeled as a perfect electric conductor, in analogy to the assumptions made in this chapter. The comparison of both methods show an overlap of the result (fig. A.1). The residuals (difference between both simulation results) are shown in fig. A.2.

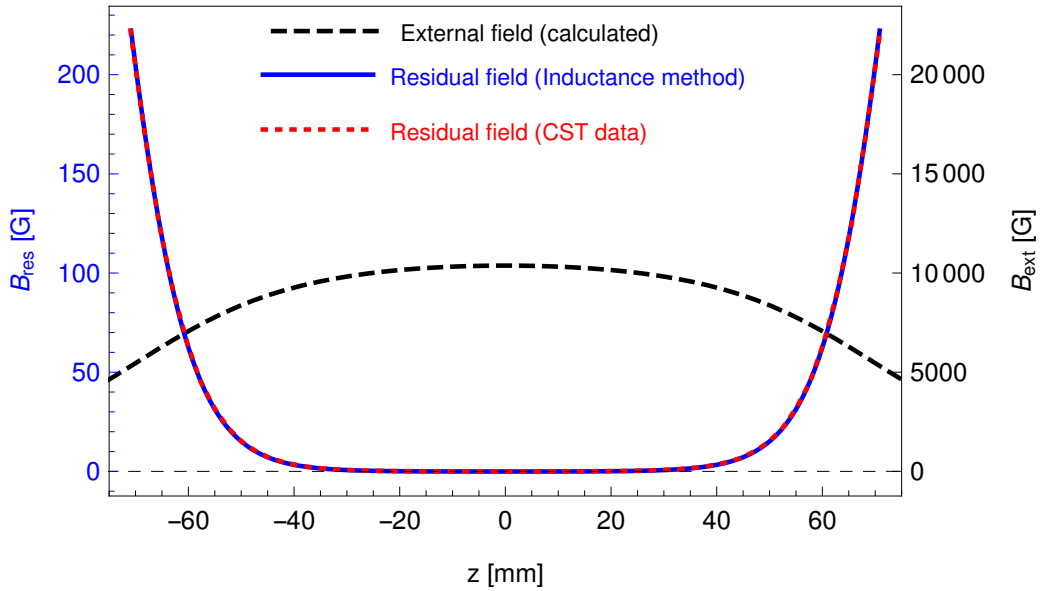

Fig. A.1: Simulation of residual field with CST Studio Suite ® 2017 (red dashed line) compared to the result of the numerical simulation in sec. 5 (blue line). The black dashed line is the external field as calculated via Biot-Savart. The scale on the right (left) corresponds to the external (residual) field.

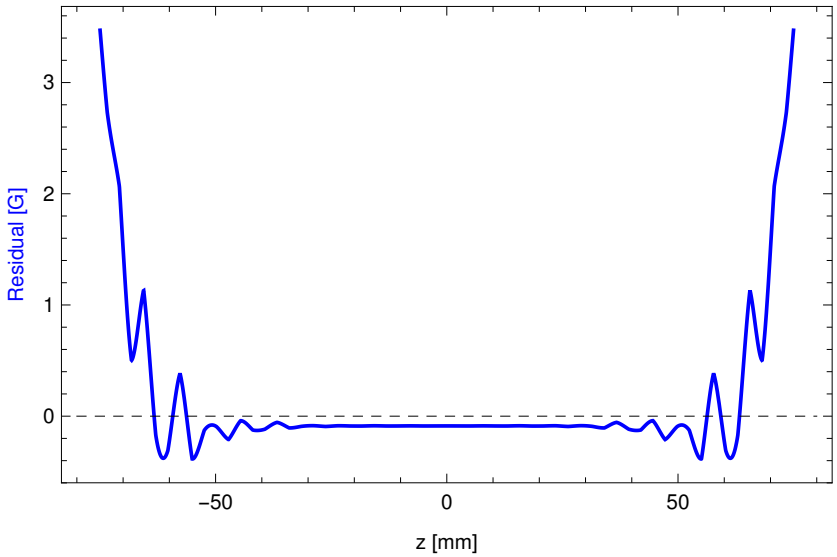

Fig. A.2: Difference (residuals) of the two calculation methods shown in the plot fig. A.1.

Appendix B

Calculation of the residual field

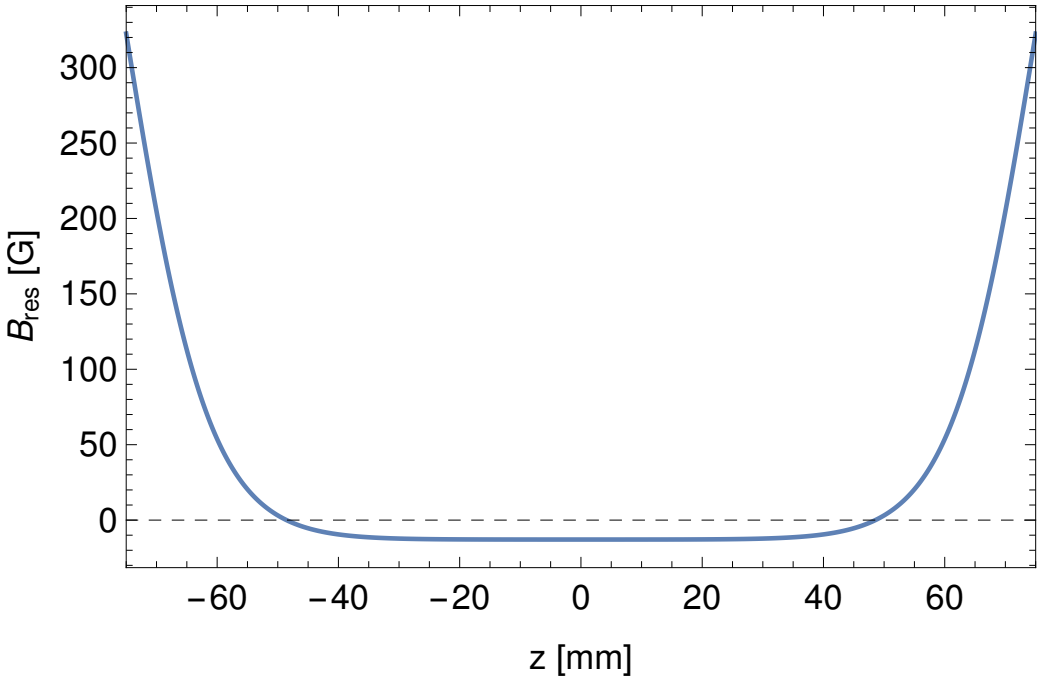

Fig. B.1: Simulation of the residual field with approximation of the geometry of all rings with a point-like cross section. This leads to an over-induced magnetic field in the shielding tube and a negative residual field.

Appendix C

Corrections to the linearity of the Hall probe

Magnetic flux density B	ΔB	Magnetic flux density B	ΔB
-20000	91.524		
-19000	79.277	50	-0.408
-18000	67.693	300	-2.198
-17000	56.774	1000	-7.408
-16000	46.521	2000	-15.054
-15000	36.934	3000	-21.524
-14000	28.014	4000	-26.23
-13000	19.763	5000	-29.108
-12000	12.18	6000	-29.654
-11000	5.266	7000	-27.646
-10000	-0.985	8000	-25.653
-9000	-6.584	9000	-22.801
-8000	-11.518	10000	-18.911
-7000	-16.646	11000	-14.191
-6000	-20.439	12000	-8.589
-5000	-20.863	13000	-2.088
-4000	-19.524	14000	5.308
-3000	-16.943	15000	13.596
-2000	-12.54	16000	22.772
-1000	-6.714	17000	32.835
-300	-2.134	18000	43.779
-50	-0.43	19000	55.602
0	0	20000	68.301

Tab. C.1: Linearity error of the Hall probe Lake Shore HGCA 3020. After correction with this values the error for operation with $I_C = 100$ mA is less then 0.01 mA.

Appendix D

Measurement program

No.	Sec.	Date	min. field [G]	max. field [G]	Type
1. a)	6.3.2	Aug 24	-12 ± 2	8290 ± 16	Calibration
1. f)	6.3.2	Aug 24	-12 ± 2	8290 ± 16	Field map
2. a)	6.3.3	Sep 3	-10250 ± 20	10180 ± 20	Ramp
2. s)	6.3.3	Sep 3 - 7	9811 ± 21	10343 ± 22	Stability
2. f)	6.3.3	Sep 2	-	10332 ± 22	Field map
3. a)	6.3.4	Aug 31	-14260 ± 40	14640 ± 40	Ramp
3. f)	6.3.4	Sep 8	-	14794 ± 38	Field map

Tab. D.1: Measurement program 2015 at Institut für Kernphysik Mainz. Calibration: Measuring the magnetic field versus the current of the external magnet. Ramp: Measuring the residual magnetic field in the center of the shielding tube by increasing and decreasing the external magnetic field. Field map: Measuring the residual field along the axis of the tube at constant external field. Stability: Measuring the residual field in the center at a constant external magnetic field. The temperature of the external magnet and the shielding tube was $T = 4.2$ K. Measurements before 31st Aug are measurements without the shielding tube. Magnetic fields higher than 10000 G means a residual field in the shielding tube, also for follow up experiments.

No.	Date	Ext. mag. [A]	Zero-field mag. [A]	Hallprobe pos. [mm]	Measurement
78	Mon Aug 24 18:23:04	0..10	0	0	ext.
80	Mon Aug 24 20:43:21	10..0	0	0	ext.
86	Mon Aug 24 23:15:50	0..10	0	0	ext.
87	Mon Aug 24 23:40:09	10	0	0..70	fieldmap
88	Tue Aug 25 00:42:08	10	0	0..-65	fieldmap
89	Tue Aug 25 01:13:56	0..24	0	0	quench
95	Tue Aug 25 16:21:05	0..30	0	0	quench
8	Mon Aug 31 17:52:52	0..17.3	0	0	loop
14	Mon Aug 31 19:01:32	17.3..0	0	0	loop
18	Mon Aug 31 20:27:37	0..-17.3	0	0	loop
19	Mon Aug 31 21:29:06	-17.3..0	0	0	loop
21	Mon Aug 31 22:27:31	0..17.3	0	0	loop
no entry		17.3..0	0	0	loop
28	Tue Sep 1 12:05:51	0..17..0..-17..0	0	0	ext.
32	Tue Sep 1 13:45:15	0..3.7	0	0	ext.
34	Tue Sep 1 14:27:39	3.7	0	0..70	fieldmap
38	Tue Sep 1 15:22:13	3.7	0	0..-65	fieldmap
43	Tue Sep 1 18:32:50	0..17.5	0	0	loop
44	Tue Sep 1 19:34:20	17.5..0..-17.2	0	0	loop
47	Tue Sep 1 22:06:47	-17.5..0..17.2	0	0	loop
49	Tue Sep 1 23:48:13	17.5..0..-17.2	0	0	loop
50	Wed Sep 2 00:12:38	-17..0	0	0	loop
59	Wed Sep 2 12:45:05	9.25	0	0..70	fieldmap
64	Wed Sep 2 13:27:13	9.25	0	0..-65	fieldmap
67	Wed Sep 2 13:53:32	12.3	0	0	ext.
71	Wed Sep 2 15:44:45	12.3	0	-65..0	fieldmap

Tab. D.2: See caption of tab.D.4

No.	Date	Ext. mag. [A]	Zero-field mag. [A]	Hallprobe pos. [mm]	Measurement
74	Wed Sep 2 16:10:12	12.3	0	0..70	fieldmap
79	Wed Sep 2 17:32:04	0	0	0..70	fieldmap
88	Wed Sep 2 18:10:45	0	0	0..-65	fieldmap
92	Wed Sep 2 18:44:00	3.7	0	-65..0	fieldmap
96	Wed Sep 2 19:08:32	3.7	0	0..70	fieldmap
101	Thu Sep 3 12:11:28	0..12..0..12..0..12	0	0	loop
106	Thu Sep 3 15:42:48	12	0	0	relax.
113	Thu Sep 3 23:32:40	12	0	0	relax.
119	Fri Sep 4 06:48:36	12	0	0	relax.
127	Fri Sep 4 15:58:39	12	0	0	relax.
137	Fri Sep 4 23:51:58	12	0	0	relax.
144	Sat Sep 5 07:29:08	12	0	0	relax.
152	Sat Sep 5 16:20:33	12	0	0	relax.
161	Sun Sep 6 00:44:39	12	0	0	relax.
172	Sun Sep 6 07:23:38	12	0	0	relax.
186	Sun Sep 6 16:48:06	12	0	0	relax.
195	Mon Sep 7 00:03:08	12	0	0	relax.
202	Mon Sep 7 07:12:36	12	0	0	relax.
210	Mon Sep 7 15:41:43	12	0	0	relax.
213	Mon Sep 7 16:03:05	12	0	0	relax.
221	Mon Sep 7 22:09:21	0	0	0	ext.
224	Mon Sep 7 22:29:34	0	0	0	relax.
233	Tue Sep 8 16:52:28	0..12	0	0	loop
237	Tue Sep 8 17:08:39	12..0	0	0	loop
240	Tue Sep 8 17:30:56	0..-12	0	0	loop
244	Tue Sep 8 17:47:04	-12..0	0	0	loop
247	Tue Sep 8 18:12:31	0..17.5	0	0	ext.

Tab. D.3: See caption of tab.D.4

No.	Date	Ext. mag. [A]	Zero-field mag. [A]	Hallprobe pos. [mm]	Measurement
250,251	Tue Sep 8 18:35:36	17.5	0	0..70..-65	fieldmap
254	Tue Sep 8 19:36:17	17.5..0	0	0	loop
259	Tue Sep 8 21:11:44	0..-17.5	0	0	loop
262	Tue Sep 8 21:39:47	-17.5..0	0	0	loop
265	Tue Sep 8 22:10:46	0..17.5	0	0	loop
272	Wed Sep 9 13:33:09	0	0	0	relax.
275	Wed Sep 9 17:56:16	0..15.9	0	0	ext.
280	Wed Sep 9 18:26:18	15.9	0	0..70	fieldmap
286	Wed Sep 9 19:14:19	15.9	0	0..-65	fieldmap
293	Wed Sep 9 19:43:05	15.9..0	0	0	loop
296	Wed Sep 9 20:02:26	0..-15.9	0	0	loop
299	Wed Sep 9 20:24:20	-15.9..0	0	0	loop
302	Wed Sep 9 20:43:08	0..15.9	0	0	loop
308	Wed Sep 9 21:41:13	0	0	0	relax.
312	Thu Sep 10 07:35:34	0..17.5	0	0	ext.
315	Thu Sep 10 07:56:26	17.5	0	0	relax.
322	Thu Sep 10 22:23:18	17.5	0	0	relax.
335	Mon Sep 14 15:09:27	13.37	0	0	ext.
340	Mon Sep 14 15:20:51	13.37	0	0..70	fieldmap
346	Mon Sep 14 15:49:23	13.37	0	0..-65	fieldmap
349	Mon Sep 14 16:07:41	14.58	0	-65	ext.
352	Mon Sep 14 16:20:10	14.58	0	-65..0	fieldmap
355	Mon Sep 14 16:35:48	14.58	0	0..70	fieldmap
362	Mon Sep 14 17:56:05	0	0	0	relax.
369	Wed Sep 16 17:36:37	0..14.56	0	0	loop
372	Wed Sep 16 17:53:45	14.56..0	0	0	loop
375	Wed Sep 16 18:09:01	0..-14.56	0	0	loop
378	Wed Sep 16 18:24:41	-14.56..0	0	0	loop
381	Wed Sep 16 18:40:38	0..14.56	0	0	loop

Tab. D.4: All measurements in a chronological order. The columns from left to right: No.: The serial number as in the log book. Date: the date of the measurement. Ext. mag. [A]: current of the external magnet. Zero-field mag. [A]: current of the Zero-field magnet. Hallprobe position: Position of the Hall probe along the axes of the shielding tube. Measurement: "loop": Ramping the current of the external magnet. "relax": Stability measurement at constant current of the external magnet. "ext": Constant current of the external magnet. "fieldmap": Probing the magnetic field along the axes of the tube at constant current of the external magnet. "quench": Ramping the current of the external magnet until quenching it.

Appendix E

Extracting points of stable current

During the measurement the stability of the current supply of the external magnet is essential for an exact magnetic field measurement. The current vs. time is recorded and a stable value is extracted from a region where the current is fluctuating around a constant value. The regions are plotted in fig. E.1 and fig. E.2.

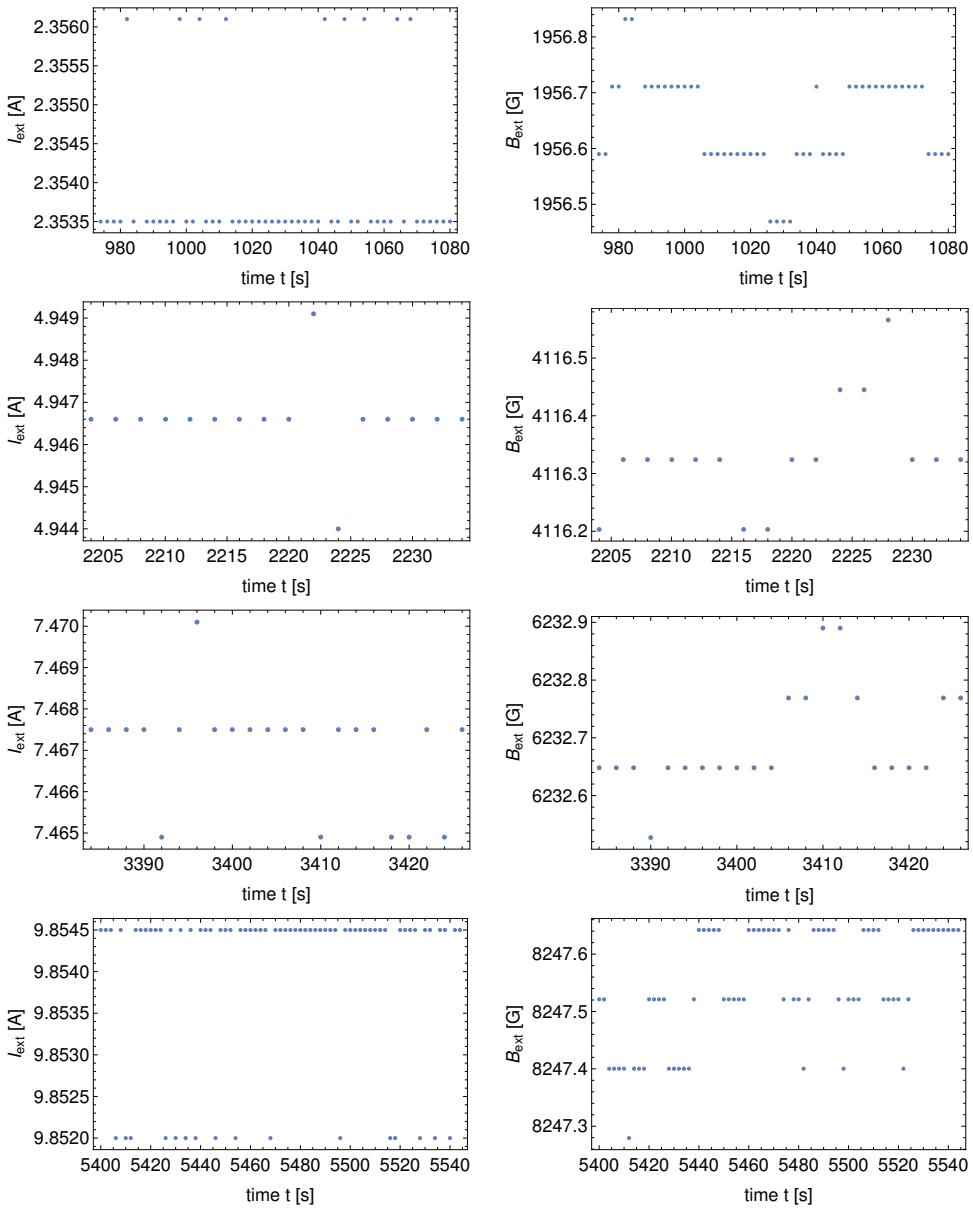

Fig. E.1: Detailed plots of the stable regions of the current and the magnetic field that were taken into account by determination of the stable value. The uncertainty is calculated and verified as given by the manufacturer. Except at the lowest point of the current, where the estimated uncertainty is 2.5 mA.

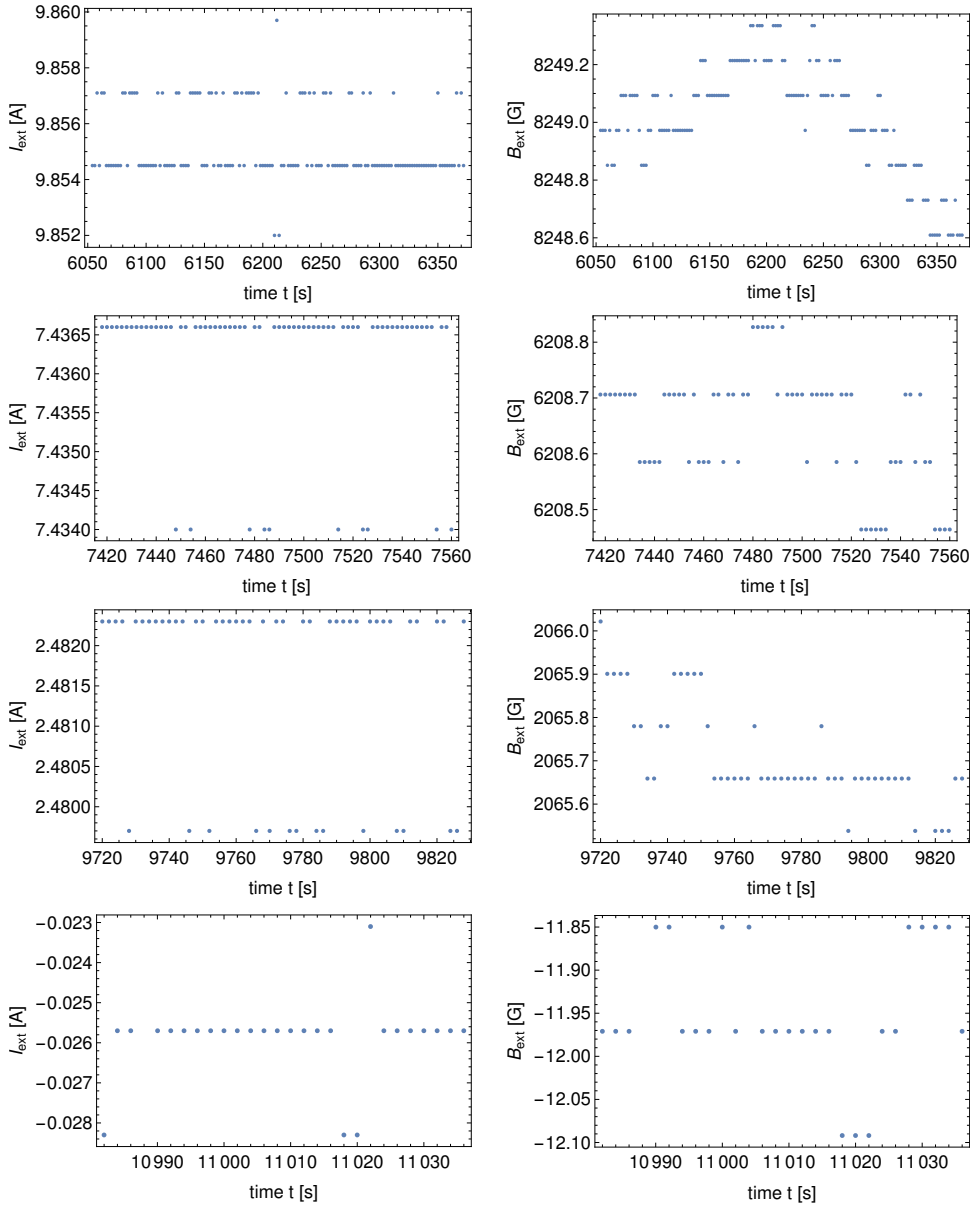

Fig. E.2: Detailed plots of the stable regions of the current and the magnetic field that were taken into account by determination of the stable value.

Appendix F

The numerical stability of the MC calculation

The numerical stability of the MC calculation was tested for two concerns. The first one is the variation of the number of generated random numbers. A convergence of the result is expected by decreasing statistical uncertainties due to increased number of generated random numbers. The Monte-Carlo data were compared with a reference function, that was calculated analytically (sec. 6.3.3). The differences of the Monte-Carlo simulated data and the analytical calculated data (residuals) for 10^4 and 10^5 generated numbers are shown in the plots fig. F.1 and fig. F.2, respectively. The residuals for 10^6 generated numbers is shown in fig. 6.24. The second concern is the proximity of a singularity resulting from the division by zero. The denominator is a random number from a normal distribution symmetric around zero. The division by zero in the simulation was avoided by cutting away those numbers equal to 0. The simulation was also tested for a cut off of those numbers, whose absolute value is greater than a predefined cut off value. The plots in fig. F.3, fig. F.4 and fig. F.5 show the results, when the cut off is 10^{-5}, 10^{-6} or 10^{-7}. The differences of the Monte-Carlo simulated data to the analytical calculated data (residuals) are shown. As expected, the total variation of the residuals does not change, while the cut off goes closer to zero.

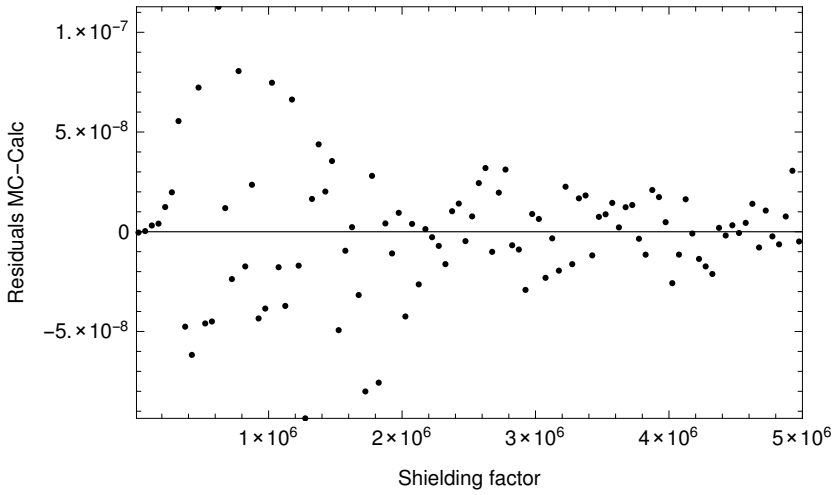

Fig. F.1: Differences of the Monte-Carlo simulation to the analytical calculation (residuals) of the shielding factor with 10^4 *simulated events.*

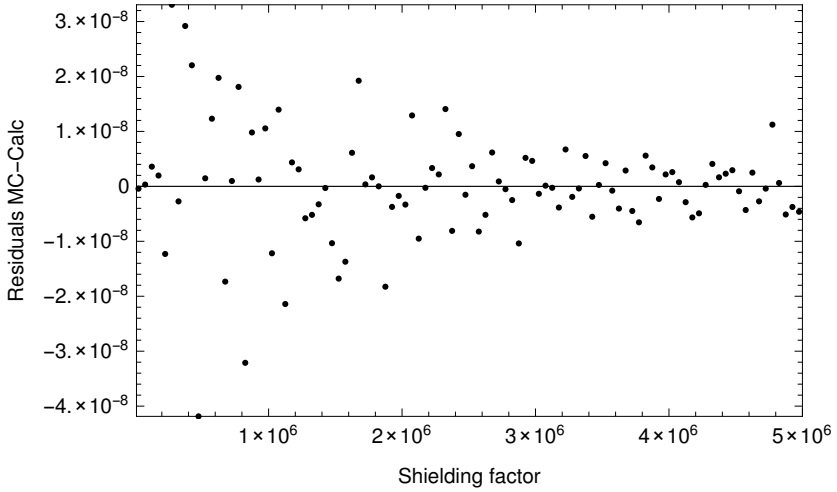

Fig. F.2: Differences of the Monte-Carlo simulation to the analytical calculation (residuals) of the shielding factor with 10^5 *simulated events.*

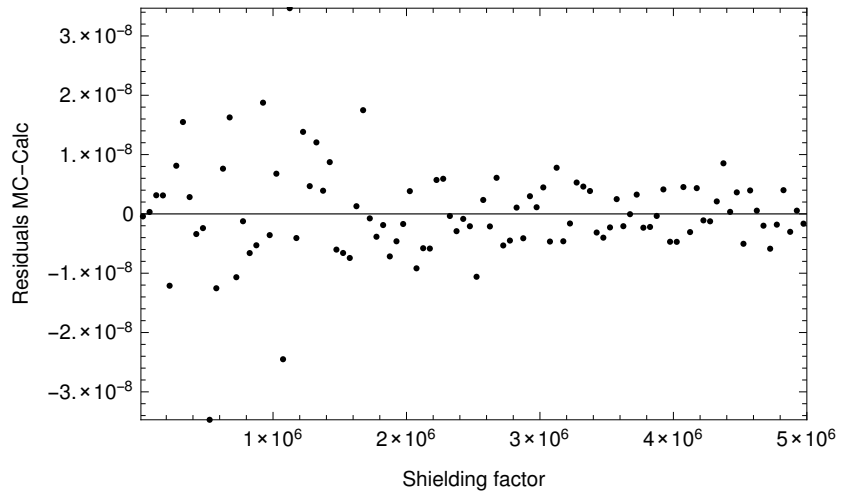

Fig. F.3: Differences of the Monte-Carlo simulation to the analytical calculation (residuals) when the cut off value is 10^{-5}.

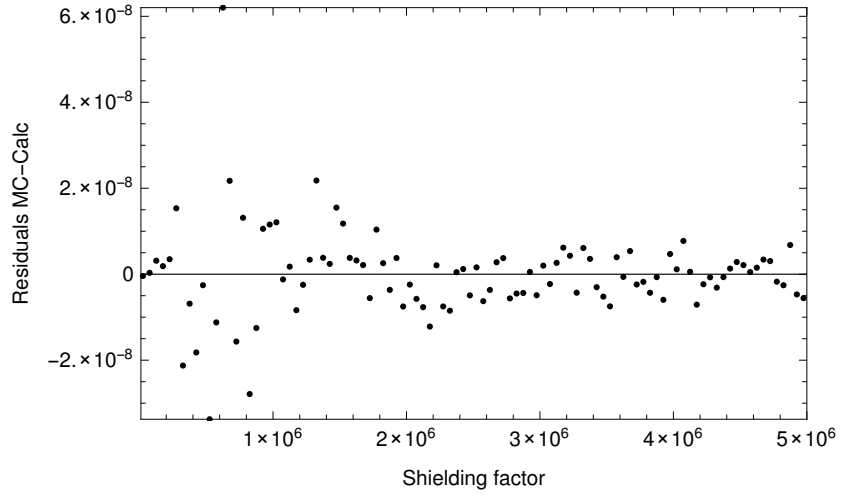

Fig. F.4: Differences of the Monte-Carlo simulation to the analytical calculation (residuals) when the cut off value is 10^{-6}.

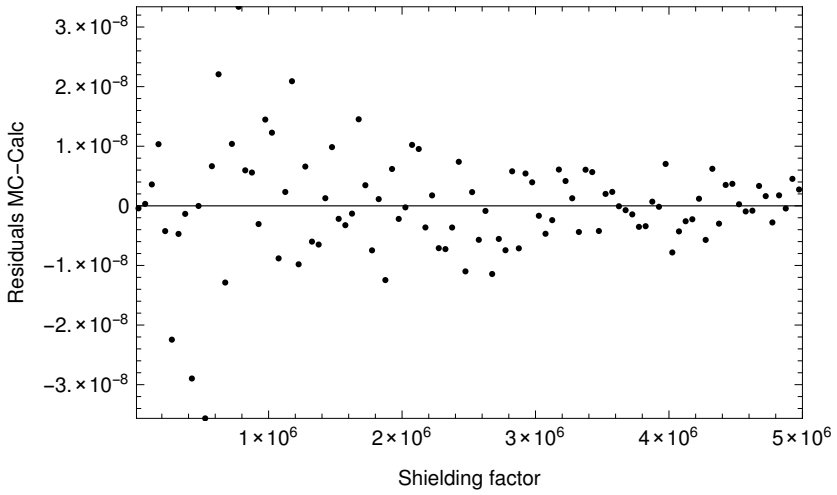

Fig. F.5: Differences of the Monte-Carlo simulation to the analytical calculation (residuals) when the cut off value is 10^{-7}.

Appendix G

Acronyms

GSI GSI Helmholtz Centre for Heavy Ion Research, Darmstadt

HIM Helmholtz-Institut Mainz

$\bar{\text{P}}$ANDA antiProton ANnihilation in DArmstadt

FAIR Facility for Antiproton and Ion Research

HESR High Energy Storage Ring

YBCO Yttrium-1 Barium-2 Copper-3 Oxid

BSCCO Bismuth-2 Strontium-2 Calcium-1 Copper-2 Oxid

CST CST Studio Suite® 2015